7-14-2016

Regional Solid Earth and Ionospheric Responses to Subduction Earthquakes in South America

Demian D. Gomez

Recommended Citation

Gomez, Demian D., "Regional Solid Earth and Ionospheric Responses to Subduction Earthquakes in South America" (2016). *Electronic Theses and Dissertations*. 1439.
https://digitalcommons.memphis.edu/etd/1439

REGIONAL SOLID EARTH AND IONOSPHERIC RESPONSES TO SUBDUCTION EARTHQUAKES IN SOUTH AMERICA

by

Demián David Gómez

A Dissertation

Submitted in Partial Fulfillment of the

Requirements for the Degree of

Doctor of Philosophy

Major: Earth Sciences

The University of Memphis

August 2016

Dedication

A mis padres, Alicia y Oscar, por darme la vida y todo lo que soy. A mi compañera inseparable de aventuras, Leslie, que me enseñó el mundo.

Para vos, que aún estás en camino.

Acknowledgements

First, I would like to thank my committee, Eunseo Choi, Chuck Langston, Mitch Withers, Randy Cox, and especially Bob Smalley, for accompanying me on this journey. After four years of hard work, Bob is not only my advisor but also my good friend, and I thank him for all his support and interesting scientific and political discussions. I should also mention that I owe my survival of my comprehensive exams to Chuck, who had very supportive words during a very stressful moment. Completing my Ph.D. at CERI gave me the tools to do excellent scientific research. It also allowed me to fulfill one of my life dreams: to do fieldwork in Antarctica.

Second, I would like to thank my friends from the National Geographic Institute (IGN) of Argentina, Diego Piñón, Agustín Raffo, Hernán Guagni, Gonzalo Ghibaudo, Tomás Cannon, and Ezequiel Antokoletz. Very special thanks to Sergio Cimbaro, President of IGN, who was first my college professor at the University of Buenos Aires, was then my supervisor at IGN, and is now a supportive friend and colleague. He gave me great support to start my scientific career.

Third, I want to thank my lifelong friends, Emilio Russ, Ignacio Sorondo, Javier Sorondo, and Patricio Myers. During these past four years they have supported my fieldwork activities in Argentina by running errands, talking to people, and hosting me at their homes. This has taken our friendship to a whole new level.

Finally, many thanks to my father, Oscar Gómez. The Central Andes GPS Project and I are greatly indebted to him for all the work done in preparation for our field campaigns, including the purchase of materials for building GPS stations, the organization of travel logistics, and much more, which he did selflessly in support of the project and of me.

“¡Gracias, Viejo!” – CARLOS GARDEL

Preface

This dissertation is composed of four published papers and one submitted manuscript. Chapter One, “A closed-form solution for earthquake location in a homogeneous half-space based on the Bancroft GPS location algorithm,” was published in the Bulletin of the Seismological Society of America. Chapter Two, “Co-seismic deformation of the 2010 Maule, Chile earthquake: Validating a least squares collocation interpolation,” was published in the Journal of the Argentine Association of Geodesy and Geophysics, GeoActa. Chapter Three, “Reference frame access under the effects of great earthquakes: a least squares collocation approach for non-secular post-seismic evolution,” was published in the Journal of Geodesy. Chapter Four, “Virtual array beamforming of GPS TEC observations of co-seismic ionospheric disturbances near the Geomagnetic South Pole triggered by teleseismic megathrusts,” was published in the Journal of Geophysical Research, Space Physics. Chapter Five, “The lithospheric stress guide and far-field co-seismic deformation,” was submitted to the Journal of Geophysical Research, Solid Earth. When reviewing the published versions, we found a minor notation mistake in Chapter One and a missing sign in Chapter Four. Corrections have been made and will be submitted to the corresponding journals as errata pages.

Before coming to The University of Memphis, I had always worked in multidisciplinary professional engineering environments and I am continuing that style of activity by bringing methodologies and techniques from other fields to Earth Sciences. This dissertation, therefore, contains a compendium that exceeds the ionospheric and solid earth response to subduction earthquakes in South America. All the chapters, however, use GPS as their principal tool.

Abstract

Gómez, Demián David, Ph.D. The University of Memphis. August, 2016. Regional Solid Earth and Ionospheric Responses to Subduction Earthquakes in South America. Robert Smalley, Jr. Ph.D. in Geophysics

First, we developed an earthquake location technique using a non-iterative GPS location algorithm known as the Bancroft algorithm. We also proposed the use of an improved quality factor for earthquake hypocenter solutions. This factor is derived from GPS and known as geometric dilution of precision (GDOP). We applied the Bancroft algorithm to ~10 years of earthquake data in the Charlevoix Seismic zone, Canada and found that this location algorithm improves the solutions of hypocenters located in regions with high GDOP.

Second, we applied and tested an interpolation technique, called least squares collocation (LSC), to the co-seismic deformation (obtained using GPS) produced by the 2010 Mw 8.8 Maule earthquake. We found that this interpolation technique cannot be used to predict the co-seismic jumps due to the low number of available GPS sites.

Third, we used the same method as before to produce a trajectory prediction model (TPM) to estimate the trajectories of passive geodetic benchmarks. This methodology proved to be very useful for engineering and surveying communities dealing with co- and post-seismic deformation in large geodetic networks after great earthquakes. The TPM for Argentina is currently being implemented by the National Geographic Institute of that country.

Fourth, we studied the ionospheric response in Antarctica to acoustic waves induced by Rayleigh waves produced by two major seismic events, the 2010 Mw 8.8 Maule earthquake and the 2011 Mw 9.0 Tohoku-Oki earthquake. We found that the geometry of the geomagnetic field at the South Geomagnetic Pole and the low elevation of GPS satellites in Antarctica favor the observation of acoustic wave-plasma coupling in the ionosphere.

Fifth and finally, we studied the lithospheric stress guide and far-field co-seismic deformation after a megathrust earthquake. We found that the energy transmitted to the far-field depends on the asthenospheric strength. We also studied the surface deformation as a function of slip source depth, finding that sources within the stress guide are amplified in the far-field as compared to those occurring in the crust. We suggested that the information collected by far-field GPS stations can help reveal lithospheric and asthenospheric structures.

Table of Contents

Chapter Page

List of Figures ix

Introduction 1

1. A closed-form solution for earthquake location in a homogeneous half-space based on the Bancroft GPS location algorithm 3
    - Introduction 3
    - GPS model for absolute positioning 6
    - The Bancroft Algorithm 10
    - Application in Seismology and Tests using Synthetic Data 17
    - Relocation of Events using Real Arrival Time Data 20
    - Quantifying solution quality 21
    - Discussion 26
    - Data and Resources 30
    - Acknowledgements 30
    - References 32

2. Co-seismic deformation of the 2010 Maule, Chile earthquake: Validating a least squares collocation interpolation 34
    - Introduction 34
    - The least squares collocation method 37
    - Synthetic data for forward validation 41
    - Elastic deformation semi-variogram 45
    - Results 48
    - Discussion and conclusions 51
    - Acknowledgements 53
    - Data sources 54
    - References 55

3. Reference frame access under the effects of great earthquakes: a least squares collocation approach for non-secular post-seismic evolution 57
    - Introduction 57
    - Underlying secular inter-seismic velocities of the CAP, RAMSAC and IGS networks 61
    - Least squares collocation of post-seismic deformation 68
    - Accessing POSGAR07 using post-seismic coordinates: co-seismic displacements 73
    - Conclusion 77
    - Acknowledgements 79
    - Data sources 79
    - References 80

4. Virtual array beamforming of GPS TEC observations of co-seismic ionospheric disturbances near the Geomagnetic South Pole triggered by teleseismic megathrusts 83
    Introduction 83
    A model for GPS TEC observations 86
    Recovery of the neutral acoustic wave 93
    Virtual array processing 95
    Observation of teleseismic Rayleigh waves in Antarctica 103
    Virtual Beamforming the Maule earthquake TEC signals in Antarctica 104
    Virtual Beamforming the Tohoku-Oki earthquake TEC signals in Antarctica 108
    Conclusion 111
    Acknowledgements 112
    Data Sources 113
    References 114

5. The lithospheric stress guide and far-field co-seismic deformation 117
    Introduction 117
    Finite element model: validation against a semi-analytic solution 120
    Problem description and setup 124
    The lithospheric stress guide 126
    Interpretation of displacement and strain 133
    The effect of the asthenospheric stiffness 138
    Influence of the stress guide on surface displacement 141
    Discussion and conclusions 143
    References 145

Conclusions 147

Bibliography 150

List of Figures

CHAPTER 1

1. Relationship between the sources. 7

2. Comparison of Bancroft algorithm and HYPOINVERSE location residuals. 18

3. Histogram of the root mean square (rms) difference between the HYPOINVERSE and Bancroft solutions using Charlevoix seismic-zone real data. 20

4. Example GDOP for the Charlevoix Seismic Network. 24

5. Histograms of the GDOP classified by rms value. 27

CHAPTER 2

1. Comparison between observed and FEM co-seismic deformation. 44

2. Station list, ordered by increasing distance from the rupture zone. 45

3. Semi-variogram of the deformation field. 46

4. Differences between LSC and synthetic co-seismic deformation. 49

CHAPTER 3

1. Histograms and time series. 64

2. Difference between Vel-Ar-Lin and VEMOS2009. 67

3. Semi-variogram plots of the north and east components of the post-seismic transient. 70

4. Least squares collocation model of the logarithmic transients. 72

5. Histogram of the difference between the modeled and observed trajectories and their fits to normal distributions. 73

6. Full Vel-Ar model test. 76

CHAPTER 4

1. Synthetic TEC response to an acoustic wave using the G&H transfer function. 92

2. Comparison of deformation as a function of time. 99

3. Results for virtual array beamform of synthetic acoustic waves. 101

4. Ionospheric TEC observation diagram. 102

5. Results for virtual array beamform of CIDs produced by the Maule earthquake. 105

6. Traditional time-distance diagram of TEC. 107

7. Results for virtual array beamform of CIDs produced by Tohoku-Oki. 109

8. Amplitude comparison of the TEC response of Maule and Tohoku-Oki earthquakes. 110

CHAPTER 5

1. Finite element model schematic view. 119

2. Comparison of surface displacements. 122

3. Surface displacement profiles. 123

4. Displacement field cross sections. 127

5. Stress cross sections. 130

6. Strain cross sections. 132

7. Depth profiles at ~400 km from the trench. 134

8. Depth profiles at ~800 km from the fault. 137

9. Displacement difference, strain energy and strain as a function of asthenospheric stiffness at ~400 km from the trench. 139

10. Displacement difference, strain energy and strain as a function of asthenospheric stiffness at ~800 km from the trench. 140

Introduction

At first glance, this dissertation may appear to mix unrelated methods and techniques applied to seismology, geodesy, and geophysics. To be more specific, Chapter One describes the application of an earthquake location technique, Chapter Two shows how to test a least squares collocation of co-seismic jumps observed in GPS time series, Chapter Three develops a new technique to predict passive geodetic benchmark displacements after a great earthquake, Chapter Four develops a new technique to apply beamforming to total electron content (TEC) time series, and Chapter Five studies in detail the lithospheric stress guide of a megathrust earthquake. All these techniques and methods are not unrelated; from earthquake location to the theory of stress guiding, all publications in this dissertation use GPS in one way or another.

In the past 20 years, GPS has become a powerful tool for the geophysics scientific community. GPS can be used to measure many geophysical variables, including crustal displacements and the response of the ionosphere to acoustic-gravity waves propagating in the atmosphere. When GPS was engineered (more than 35 years ago) most of these applications were not part of the original design, which was meant for positioning and timing. The extensive use of GPS has created a variety of techniques and tools to process and analyze GPS data.

Some of the techniques used for GPS data processing can also be applied to fields other than geodesy. We show this in Chapter One, where we apply the Bancroft algorithm for GPS location to the earthquake location problem, proving that under certain circumstances, Bancroft estimates a better earthquake location solution than traditional methods. We show this with an example application in the Charlevoix Seismic zone by relocating more than 1,200 events reducing the rms of ~55% of them.

GPS data used for research activities can also be used to produce models for the engineering community. As a secondary goal, therefore, we develop a model of the benchmark displacements (both co- and post-seismic) in South America produced by the 2010 Maule earthquake. These kinematic models of GPS displacements help to reveal post-seismic spatial patterns, which contributes to our understanding of the South America-Nazca plate boundary. Chapters Two and Three show and develop new techniques to generate kinematic models using GPS displacements produced by a large earthquake.

The last two chapters of this dissertation show the scientific results of our work. Chapter Four shows how GPS TEC time series can be used to beamform acoustic wave signals triggered by distant earthquake sources that produce Rayleigh waves in Antarctica. We find that the South Geomagnetic Pole has special characteristics that allow these acoustic wave signals (produced by the coupling between the solid earth and the atmosphere) to appear in the ionosphere as TEC disturbances. Our modified beamforming technique estimates the direction and slowness of these disturbances, finding signals produced by sources located ~7,500 km and 12,500 km away from our study area. These are the farthest co-seismic TEC disturbances ever detected using GPS.

The final chapter of this dissertation shows the solid earth component of our research. We investigate in detail the effects of the stiffness of the lithosphere and asthenosphere on the lithospheric stress guide. This work is part of our ongoing efforts to understand the role of the stress guide in far-field deformation produced in South America by megathrust earthquakes.

CHAPTER 1

A closed-form solution for earthquake location in a homogeneous half-space based on the Bancroft GPS location algorithm

Published in the Bulletin of the Seismological Society of America

Introduction

The standard introduction to earthquake and GPS location sets the problem up in a homogeneous half-space, in which ray paths are straight lines. Although the earthquake location problem usually requires a more complex velocity model, and bending ray paths, this does not affect the basic development. In addition, there are cases in which the homogeneous half-space velocity model is the best practical model to locate earthquakes. In the case of GPS, unlike seismology, ray-path bending is a second-order effect and a constant velocity model is appropriate. Bancroft (1985) found a closed-form rather than iterative solution for the GPS location problem with a uniform velocity model. We will show that both the GPS and earthquake location problems in a uniform velocity model are analogous, and the Bancroft algorithm can be used to locate hypocenters. In theory, this method has a few shortcomings such as larger sensitivity to data outliers, because it minimizes the sum of the fourth power of the errors rather than the square (as in least squares). However, we will use real data that the method is capable of finding solutions with smaller root mean square (rms) errors than such traditional earthquake location methods as HYPOINVERSE (Klein, 1978). We will begin examining the development of the earthquake location problem.

Given a uniform half-space and *P* arrival times from an earthquake at a number of seismic stations (*N*) with known locations (X_n, Y_n, Z_n), the hypocenter and origin time

(X, Y, Z, t) of the earthquake can be found from the following analysis. The travel time T_n to the *n*th seismic station is

$$T_n = \frac{d_n}{v} = \frac{\sqrt{(X - X_n)^2 + (Y - Y_n)^2 + (Z - Z_n)^2}}{v} . \tag{1}$$

in which d_n is the distance between the *n*th station and the earthquake, and v is the *P* or *S* velocity for the half-space. The left hand side of equation (1) is travel time, but the seismic observables are arrival times. As the origin time of an event is unknown, we need some way to estimate it. Subtracting the earliest arrival time from each observation yields N - 1 nonzero arrival-time differences that are travel times offset by a constant value equal to the travel time from the hypocenter to the closest seismic station. We can therefore rewrite equation (1) in terms of relative arrival times by subtracting the travel time t to the nearest station:

$$\overline{T_n} = \frac{\sqrt{(X - X_n)^2 + (Y - Y_n)^2 + (Z - Z_n)^2}}{v} - t . \tag{2}$$

With *P* arrival times from four or more stations, the hypocenter and origin time can be found by simultaneously solving the set of equations. Although this analysis also works with *S* waves, earthquakes are not generally located using only *S* waves. If both *P* and *S* waves are available, d_n can be estimated directly from the T_S-T_P arrival times, and data from only three stations are needed (two arrival times per station, one for *P* and another for *S*, i.e. six observations).

Equation (2) is nonlinear and cannot be solved analytically as it is written. Such problems are typically solved by using a truncated Taylor series to linearize the problem and least squares to find the solution that minimizes the observation errors. A complete discussion on the history of least squares and some applications to geodesy can be found in Nievergelt (2000). Following Geiger (1910, 1912) for an initial estimate for the earthquake location of (X_0, Y_0, Z_0, t_0), we can write the travel time to the *n*th station as

$$\overline{T_n} \approx \left.\frac{\partial T_n}{\partial X}\right|_{(X_0,Y_0,Z_0,t_0)} \delta X_0 + \left.\frac{\partial T_n}{\partial Y}\right|_{(X_0,Y_0,Z_0,t_0)} \delta Y_0 + \left.\frac{\partial T_n}{\partial Z}\right|_{(X_0,Y_0,Z_0,t_0)} \delta Z_0 + \left.\frac{\partial T_n}{\partial t}\right|_{(X_0,Y_0,Z_0,t_0)} \delta t_0 \qquad (3)$$

A common value for the initial estimate is the location of the station having the first arrival with fixed depth and time offsets. Equation (3) gives the exact solution of the four unknowns using the following four equations:

$$\begin{aligned} &X = X_0 + \delta X_0, \quad Y = Y_0 + \delta Y_0, \\ &Z = Z_0 + \delta Z_0, \text{ and } t = t_0 + \delta t_0. \end{aligned} \qquad (4)$$

Each seismic station has one equation (observation) of the type shown in equation (3). If four observations are available, the unknown parameters may be found using standard matrix inversion methods. In the case of an over-determined system (more than four measurements), least squares can be used to minimize the errors for the set of equations for the corrections in (3) to generate a new trial solution (X_0, Y_0, Z_0, t_0) to be used in the next estimate of this iterative procedure, until convergence (or failure) is obtained. Because the relation between the time corrections and the coordinates of the hypocenter is non-linear, dropping the higher degrees of the Taylor series in equation (3) requires assuming that the correction terms in (4) are small enough to correctly approximate equation (2). If the correction terms are large, a single iteration might not be sufficient for convergence and additional iterations may be necessary. This introduces a limitation to the method, since the initial estimate (X_0, Y_0, Z_0, t_0) has to be close enough to the real solution to keep the error terms small. If this condition is not satisfied, the iteration may either converge very slowly or not converge at all (Lee and Stewart, 1981; Thurber, 1985).

We now examine the Global Positioning System (GPS) absolute positioning case and its solution and show it is analogous to the earthquake location problem. This comparison will validate the use of a series of tools developed in GPS analysis for seismology.

GPS model for absolute positioning

GPS consists of a constellation of 24-32 satellites, orbiting the Earth at an altitude of 20,200 km that provide navigation and time transfer signals. In the navigation application, GPS equipment provides the location of its antenna with an error that varies from meters to a few millimeters depending on the positioning technique used.

The most common use of GPS is to obtain the absolute position of a single receiver on or near the surface of the Earth. This is done by multiplying the travel time of the GPS radio signal, from a satellite whose position is known, by the speed of light to produce a pseudorange (Figure 1) that is used to calculate locations with precisions of 5 m or better. The receiver estimates the travel times using the arrival times of coded, time-synchronized signals transmitted by the GPS satellites. In earthquake location terms, this is similar to using S-P times and V_P and V_S to determine the distance from a station to the source (Figure 1). When applied to earthquake location, the pseudoranges (*S*-*P* distances) are used to solve for the XYZ coordinates of a hypocenter.

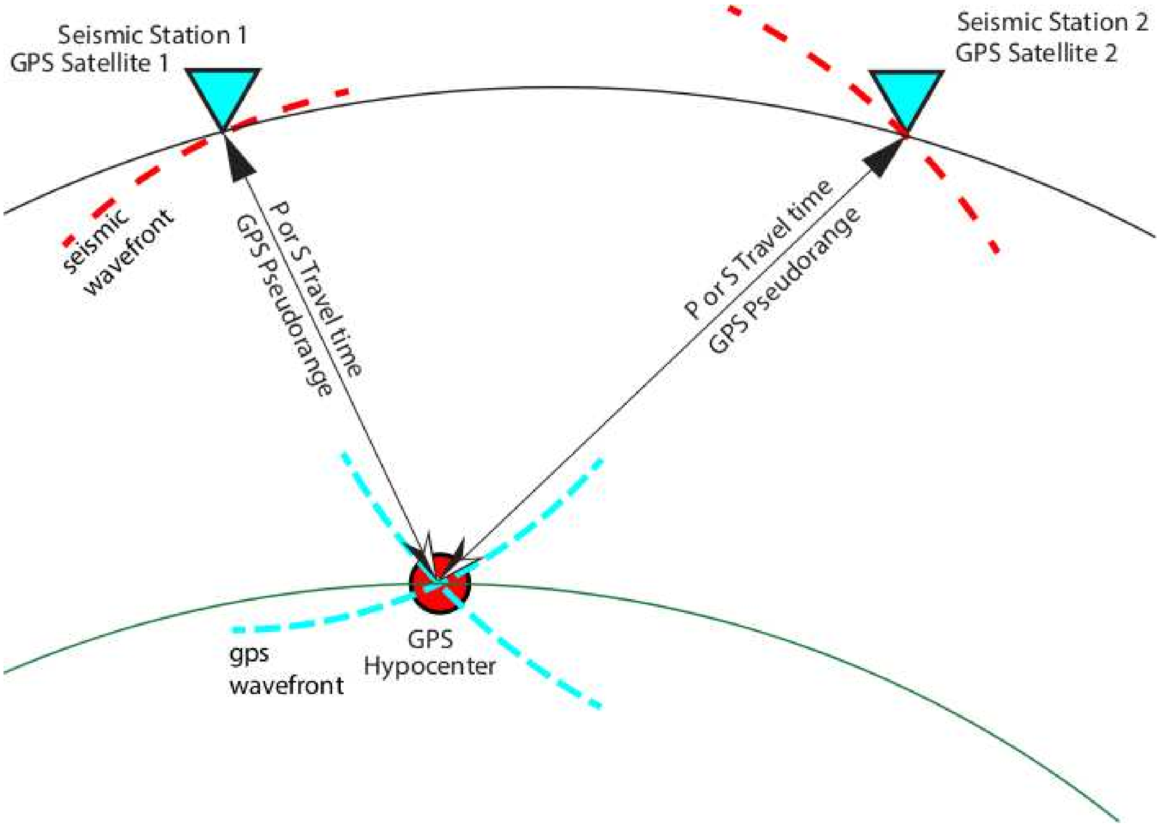

Figure 1. Relationship between the sources (earthquakes or Global Positioning System [GPS] satellites) and receivers (seismic stations or GPS receivers). The circle indicates an unknown position (GPS receiver or hypocenter), the triangles indicate known position (GPS satellites or seismic stations), the solid labeled lines show ray paths and the dashed lines show the GPS or seismic wave fronts. The color version of this figure is available only in the electronic edition.

Because of the large value of the speed of light, very accurate time measurements are required to correctly determine the pseudoranges. One solution to achieve sufficient precision is to use atomic clocks. This is the solution used in the GPS satellites; however, because the size and cost of such devices are prohibitive for most GPS receivers, consumer-quality quartz clocks are typically used. Such clocks are not precise enough to perform pseudorange measurements (as a reference, a 1 ms timing error for a signal traveling at the speed of light becomes a 300 km pseudorange error), but this problem can be overcome by using a fourth pseudorange measurement to estimate a correction for the receiver clock. This solution allows the receiver to determine time almost as accurately as the satellite clocks.

By taking into account the clock correction term, the equation for the pseudorange can be written as

$$\rho_i = t_i c = \sqrt{(X_r - X_i)^2 + (Y_r - Y_i)^2 + (Z_r - Z_i)^2} - \delta t c \tag{5}$$

(Leick, 1994), in which *c* is the appropriate speed of light, t_i is the travel time determined by the receiver, (X_i, Y_i, Z_i) are the coordinates of the *i*th satellite, (X_r, Y_r, Z_r) are the unknown coordinates of the GPS receiver, and δt is the receiver clock error. With four or more of these equations, we can solve for the location of the receiver and the receiver clock error.

Because the signals transmitted by the satellites are precisely synchronized and their departure times can be calculated by the receiver, the δt term in equation (5) represents the correction to apply to the receiver’s clock in order to synchronize it to the GPS satellite time frame. A full discussion on GPS pseudorange measurements can be found in Leick (1994). To compare this error term with its seismological counterpart, we can think of the time of an event with respect to the synchronized time frame of a seismic station network. When an event occurs, the *t* term in the right hand side of equation (2) is estimated to place the event in the network time frame. This is equivalent to placing the receiver in the GPS satellite time frame.

Dividing equation (5) by the speed of light, we obtain

$$t_i = \frac{\sqrt{(X_r - X_i)^2 + (Y_r - Y_i)^2 + (Z_r - Z_i)^2}}{c} - \delta t \,, \tag{6}$$

in which t_i is the measured travel time. This expression is identical to equation (2) that we found for the earthquake location problem. This shows that for a uniform half-space the earthquake location and GPS positioning problems are equivalent. This is the key observation supporting the application of the Bancroft algorithm to earthquake location. The principal difference is in the location of receivers and sources (Figure 1). In GPS, the known locations are the sources (GPS satellites), and the unknown is the GPS receiver location. In contrast, in earthquake location, the receivers (the seismic stations) have the known locations, and the hypocenter has an unknown location. Because of the principle of reciprocity, interchanging sources and receivers between the two problems yields the same results.

In GPS, two signals (L1 and L2) with different frequencies are employed. They provide first-order correction for a time delay produced by a dispersive change of the speed of light in the ionosphere. A similar, but nondispersive change in the speed of light occurs in the troposphere, with a time delay estimated using a theoretical model. The length difference between the geometrical and the optical ray paths due to refraction in the ionosphere and troposphere is very small, thus the bending of the ray paths can be neglected when computing GPS solutions. Only the corrections for the ionospheric and tropospheric delays are required to properly compute the pseudoranges, allowing us to consider the ray paths as straight, at least to first order. In seismology, straight rays are associated with a constant velocity, which will allow us to apply the

GPS closed-form solutions to earthquake location. More complex velocity models having non-constant velocities, where one cannot neglect bending of the seismic ray path, are outside the scope of this article.

The Bancroft Algorithm

The application of the closed-form solution of Bancroft to earthquake location is limited to homogeneous half-spaces, a nonrealistic earth velocity structure model in many cases. This work is not intended to present a new, general method to replace current earthquake location techniques. The homogeneous half-space model, however, is sometimes the most appropriate. The Geological Survey of Canada, for example, uses a uniform half-space velocity model to locate events in the Charlevoix seismic zone (CSZ). In the following sections, we will use data from Charlevoix to test the performance of the Bancroft algorithm against a standard earthquake location program (HYPOINVERSE, Klein, 1978).

We will now present development of a solution to equation (2), and its equivalents (5) and (6), developed by Bancroft (1985) and discuss the algorithm's contributions to the earthquake location problem. Equation (5) is nonlinear due to the square root term. By simply isolating the square root on the right hand side, and squaring both sides of the equation we obtain:

$$(\rho_i + \delta tc)^2 = (X_r - X_i)^2 + (Y_r - Y_i)^2 + (Z_r - Z_i)^2 \,. \qquad (7)$$

Expanding and rearranging this expression yields:

$$-[X_r{}^2 + Y_r{}^2 + Z_r{}^2 - (\delta tc)^2] = (X_i{}^2 + Y_i^2 + Z_i{}^2 - \rho_i{}^2) - 2(X_i X_r + Y_i Y_r + Z_i Z_r - \rho_i \delta tc) \,. \qquad (8)$$

Solving equation (8) for (X_r, Y_r, Z_r) and δt is no easier than solving equation (2). To recast equation (8) into an equation with a closed-form solution, Bancroft introduces the Minkowski functional (Minkowski, 1907/1908), also known as the Lorentz inner product, from relativity theory. Although the justification for the use of this inner product was not discussed in Bancroft (1985), the application of the Minkowski functional implies that the geometry of a system of pseudorange equations is hyperbolic (Chaffee and Abel, 1994). Other authors such as Pujol and Smalley (1990) have taken advantage of this geometry to solve for the coordinates of earthquake hypocenters. Regardless of the hyperbolic geometry, Sirola (2010) showed that the Bancroft algorithm can also be derived without the use of the Minkowski functional. In this paper, however, we will follow Bancroft's notation and derivation.

The Minkowski functional for four-space is defined as

$$\langle \mathbf{a}, \mathbf{b} \rangle = \mathbf{a}^T \mathbf{M} \mathbf{b} \tag{9}$$

in which **M** is the 4 x 4 matrix:

$$\mathbf{M} = \begin{bmatrix} 1 & 0 & 0 & 0 \\ 0 & 1 & 0 & 0 \\ 0 & 0 & 1 & 0 \\ 0 & 0 & 0 & -1 \end{bmatrix}. \tag{10}$$

The Minkowski functional is also the standard dot product between two relativistic four-space position vectors with elements $\begin{bmatrix} X \\ Y \\ Z \\ \sqrt{-1}\ t \end{bmatrix}$. Defining the vectors

$$\overline{\mathbf{X}}_i = \begin{bmatrix} X_i \\ Y_i \\ Z_i \end{bmatrix} \text{ and } \overline{\mathbf{X}}_r = \begin{bmatrix} X_r \\ Y_r \\ Z_r \end{bmatrix} \tag{11}$$

the terms of equation (8) can be rewritten using the Minkowski functional:

$$\begin{aligned} X_i^{\,2} + Y_i^2 + Z_i^{\,2} - \rho_i^{\,2} &= \left\langle \begin{bmatrix} \overline{\mathbf{X}}_i \\ \rho_i \end{bmatrix}, \begin{bmatrix} \overline{\mathbf{X}}_i \\ \rho_i \end{bmatrix} \right\rangle \\ X_r^{\,2} + Y_r^{\,2} + Z_r^{\,2} - (\delta tc)^2 &= \left\langle \begin{bmatrix} \overline{\mathbf{X}}_r \\ \delta tc \end{bmatrix}, \begin{bmatrix} \overline{\mathbf{X}}_r \\ \delta tc \end{bmatrix} \right\rangle \\ X_i X_r + Y_i Y_r + Z_i Z_r - \rho_i \delta tc &= \left\langle \begin{bmatrix} \overline{\mathbf{X}}_i \\ \rho_i \end{bmatrix}, \begin{bmatrix} \overline{\mathbf{X}}_r \\ \delta tc \end{bmatrix} \right\rangle . \end{aligned} \tag{12}$$

And equation (8) becomes

$$\frac{1}{2}\left\langle \begin{bmatrix} \overline{\mathbf{X}}_i \\ \rho_i \end{bmatrix}, \begin{bmatrix} \overline{\mathbf{X}}_i \\ \rho_i \end{bmatrix} \right\rangle + \frac{1}{2}\left\langle \begin{bmatrix} \overline{\mathbf{X}}_r \\ \delta tc \end{bmatrix}, \begin{bmatrix} \overline{\mathbf{X}}_r \\ \delta tc \end{bmatrix} \right\rangle - \left\langle \begin{bmatrix} \overline{\mathbf{X}}_i \\ \rho_i \end{bmatrix}, \begin{bmatrix} \overline{\mathbf{X}}_r \\ \delta tc \end{bmatrix} \right\rangle = 0. \tag{13}$$

To further simplify equation (13), Bancroft introduces the following two terms:

$$E = \frac{1}{2}\left\langle \begin{bmatrix} \overline{\mathbf{X}}_r \\ \delta tc \end{bmatrix}, \begin{bmatrix} \overline{\mathbf{X}}_r \\ \delta tc \end{bmatrix} \right\rangle \text{ and } a_i = \frac{1}{2}\left\langle \begin{bmatrix} \overline{\mathbf{X}}_i \\ \rho_i \end{bmatrix}, \begin{bmatrix} \overline{\mathbf{X}}_i \\ \rho_i \end{bmatrix} \right\rangle . \tag{14}$$

For each observation (to a satellite or seismic station), a term a_i can be calculated. These terms can be arranged into a column vector:

$$a = \begin{bmatrix} \frac{1}{2}\left\langle \begin{bmatrix} \overline{\mathbf{X}}_1 \\ \rho_1 \end{bmatrix}, \begin{bmatrix} \overline{\mathbf{X}}_1 \\ \rho_1 \end{bmatrix} \right\rangle \\ \frac{1}{2}\left\langle \begin{bmatrix} \overline{\mathbf{X}}_2 \\ \rho_2 \end{bmatrix}, \begin{bmatrix} \overline{\mathbf{X}}_2 \\ \rho_2 \end{bmatrix} \right\rangle \\ \vdots \\ \frac{1}{2}\left\langle \begin{bmatrix} \overline{\mathbf{X}}_i \\ \rho_i \end{bmatrix}, \begin{bmatrix} \overline{\mathbf{X}}_i \\ \rho_i \end{bmatrix} \right\rangle \end{bmatrix} . \tag{15}$$

Because the last equation of equation set (12) has both known and unknown terms and there are *i* observation equations, the Minkowski functional form for the matrix equation to be solved can be rewritten in a non-compact fashion that isolates the unknown terms:

$$\left\langle \begin{bmatrix} \overline{\mathbf{X}}_i \\ \rho_i \end{bmatrix}, \begin{bmatrix} \overline{\mathbf{X}}_r \\ \delta tc \end{bmatrix} \right\rangle = \mathbf{BM} \begin{bmatrix} \overline{\mathbf{X}}_r \\ \delta tc \end{bmatrix} , \tag{16}$$

where **B** is a *i* x 4 matrix containing all the known terms from equation (8)

$$\mathbf{B} = \begin{bmatrix} X_1 & Y_1 & Z_1 & \rho_1 \\ X_2 & Y_2 & Z_2 & \rho_2 \\ \vdots & \vdots & \vdots & \vdots \\ X_i & Y_i & Z_i & \rho_i \end{bmatrix}. \tag{17}$$

Substituting equations (16) and (14) into equation (13) and defining $\mathbf{e} = [1\ 1\ 1\ \cdots\ 1]^T$, we obtain

$$\mathbf{a} - \mathbf{BM}\begin{bmatrix} \overline{\mathbf{X}}_r \\ \delta tc \end{bmatrix} + E\mathbf{e} = 0. \tag{18}$$

Solving equation (18) for the vector containing the unknowns $\begin{bmatrix} \overline{\mathbf{X}}_r \\ \delta tc \end{bmatrix}$ yields the so-called GPS navigation equation,

$$\begin{bmatrix} \overline{\mathbf{X}}_r \\ \delta tc \end{bmatrix} = (\mathbf{BM})^{-1}(E\mathbf{e} + \mathbf{a}). \tag{19}$$

Because the *E* term defined in equation (14) also includes the unknowns $\begin{bmatrix} \overline{\mathbf{X}}_r \\ \delta tc \end{bmatrix}$, equation (19) is nonlinear and cannot be solved as given. Applying the Minkowski functional again to both sides of equation (19) yields

$$\left\langle \begin{bmatrix} \overline{\mathbf{X}}_r \\ \delta tc \end{bmatrix}, \begin{bmatrix} \overline{\mathbf{X}}_r \\ \delta tc \end{bmatrix} \right\rangle = \left\langle (\mathbf{BM})^{-1}(E\mathbf{e}+\mathbf{a}), (\mathbf{BM})^{-1}(E\mathbf{e}+\mathbf{a}) \right\rangle. \tag{20}$$

This can be rewritten as

$$2E = [(BM)^{-1}(Ee+a)]^T M (BM)^{-1}(Ee+a). \tag{21}$$

Rearranging equation (21) and using $\mathbf{M}^{-1} = \mathbf{M}$ and $\langle \mathbf{Ma}, \mathbf{Mb} \rangle = \langle \mathbf{a}, \mathbf{b} \rangle$, we obtain a quadratic equation in *E:*

$$\left\langle \mathbf{B}^{-1}\mathbf{e}, \mathbf{B}^{-1}\mathbf{e} \right\rangle E^2 + 2\left(\left\langle \mathbf{B}^{-1}\mathbf{e}, \mathbf{B}^{-1}\mathbf{a} \right\rangle - 1 \right) E + \left\langle \mathbf{B}^{-1}\mathbf{a}, \mathbf{B}^{-1}\mathbf{a} \right\rangle = 0. \tag{22}$$

In this expression, all the components of the quadratic coefficients **B**, **e** and **a** are known, thus the value of *E* can be found. This solution will yield two possible values for *E*, from which the physically correct answer is chosen, that is, a positive pseudorange value. If both values for *E* are positive, the correct answer is the one that yields a solution that has a coordinate below the seismic network. If a solution for the problem cannot be found, both values for *E* might be negative or imaginary. Once *E* is obtained, equation (19) can be used to solve for $\begin{bmatrix} \overline{X}_r \\ \delta tc \end{bmatrix}$. Abel and Chaffee (1991) and Chaffee and Abel (1994) more fully discuss details about the uniqueness and existence of the solution.

For the case of a system with more than four observations, the matrix **B** will have more than four rows and thus it will not be invertible. This is addressed in the standard method by applying the Moore-Penrose pseudoinverse to **B**:

$$\mathbf{B}^{+} = (\mathbf{B}^{T}\mathbf{B})^{-1}\mathbf{B}^{T} . \tag{23}$$

Using the Moore-Penrose pseudoinverse for $\mathbf{B}^{-1}$ in (19) one obtains the regular least squares form with an extra term $\mathbf{M}^{-1}$:

$$\begin{bmatrix} \overline{\mathbf{X}}_{r} \\ \delta tc \end{bmatrix} = (\mathbf{B}^{T}\mathbf{B})^{-1}\mathbf{B}^{T}\mathbf{M}^{-1}(E\mathbf{e} + \mathbf{a}). \tag{24}$$

Taking a closer look to the term $(Ee + a)$, however, the reader will notice that the observations in the vector **a** are squared due to the Minkowski functional. This squaring of observations will have a few consequences that will be discussed later.

The development of the Bancroft method was primarily motivated by the need to solve equation (5) using minimum computer and power resources. This algorithm has been widely used in GPS receivers since it does not require any *a priori* information about the initial location, reducing the receivers' cold start up time. The Bancroft algorithm is only one of many other closed-form solutions developed for GPS positioning that could also be implemented for earthquake location. For other examples, see Sirola (2004).

Application in Seismology and Tests using Synthetic Data

We have reviewed the GPS inverse problem and the earthquake location problem and observed that they are identical when using a uniform half-space velocity model. We will now test the Bancroft algorithm and compare the results to a standard earthquake location program, HYPOINVERSE (Klein, 1978), using both synthetic and real data for the Charlevoix seismic network. We will relocate ~1200 events from the Charlevoix catalog that occurred during December 1989 – August 1999 time period. Finally, we will introduce a method of quantifying the quality of the solution, known as dilution of precision (DOP) that is based on the hypocenter-network geometry, and show that DOP is more informative than azimuthal gap.

Using the CSZ seismicity catalog (see Data and Resources Section), we obtained synthetic data by calculating travel times to the Charlevoix seismic network stations in a uniform velocity half-space for 1330 events during the selected time period. Random Gaussian noise, with a standard deviation of 0.02 s, was added to the synthetic data to simulate typical picking time errors (Powell *et al.*, 2010). At this time, we are not assuming long tails caused by erroneous picks or phase association misidentifications, because the goal of the synthetic analysis is to establish the capability of each method (Bancroft and HYPOINVERSE) to obtain the original hypocenter.

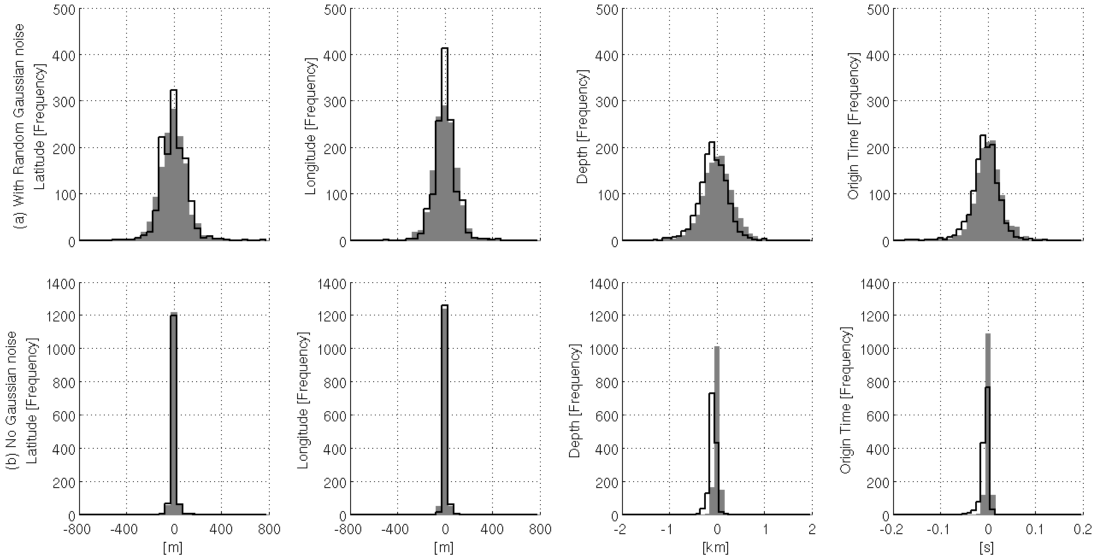

Figure 2. Comparison of Bancroft algorithm and HYPOINVERSE location residuals using synthetic data (a). Dark gray indicates Bancroft, and the black lines indicate HYPOINVERSE. Histograms are shown for latitude, longitude, depth, and origin time residuals calculated from the true and estimated solutions using HYPOINVERSE and the Bancroft algorithms. The x axis shows residual values and y axis shows frequency. (b) Histograms of the same variables but without adding Gaussian noise to synthetics.

Histograms of the difference between the true and estimated solutions are shown in Figure 2a. Both methods successfully located 100% of the hypocenters. For latitude and longitude, Bancroft and HYPOINVERSE solutions appear to be equally accurate with Bancroft showing a slightly more dispersed distribution. To quantify these results, we fit normal distributions to the histograms in Figure 2a. The results of these fits are shown in Table 1 (“Gaussian Noise” [GN] columns). For depth and origin time estimations, Bancroft seems to be slightly more accurate but more dispersed than HYPOINVERSE, confirming that HYPOINVERSE solutions are slightly biased.

Table 1. Normal fit distributions to histograms. Normal fit distributions to histograms using data with added Gaussian noise (GN) and without Gaussian noise (NN). Bancroft fits show that its solutions are slightly more accurate but more dispersed than those from HYPOINVERSE.

Solution		**Lat. (m)**		**Lon. (m)**		**Depth (m)**		**O. Time (s)**	
		GN	NN	GN	NN	GN	NN	GN	NN
Bancroft	Mean	3.8	-0.35	-5.8	0.14	15	0.04	0.001	3e-5
	St. Dev	111.0	16.00	94.0	14.00	315	47.0	0.029	0.004
HYPOINVERSE	Mean	-4.3	-0.68	8.9	5.50	-61	-76.0	0.004	-0.005
	St. Dev	97.0	20.00	86.0	17.00	279	63.0	0.028	0.008

To better understand the behavior observed in Figure 2a, we performed a second synthetic test without adding Gaussian noise to the arrival times. Figure 2b shows that after removing the Gaussian noise, the HYPOINVERSE depth and origin time estimations show asymmetric histograms while the Bancroft solution is always centered at zero. The “No Gaussian Noise” (NN) column in Table 1 shows the results of the normal distribution fits. The persistent bias observed in depth and origin time is probably a result of small differences between our forward calculation and HYPOINVERSE’s seismic stations coordinate transformations used to solve the inverse problem. We arrive to this conclusion after always observing the same bias running HYPOINVERSE with different trial depths and iteration criteria. We also conclude that these biases are too small to modify the result of the tests using the real Charlevoix seismic zone arrival time data, presented in the next section.

We should mention that HYPOINVERSE’s input format for arrival time data is FORTRAN F5.2 which only allows precision to a hundredth of a second, and this round off contributes to some of the dispersion observed in HYPOINVERSE result with noiseless data. To compare against the Bancroft algorithm, we used the same input precision. Using full double precision arrival times (in MATLAB; see Data and Resources), the Bancroft algorithm finds a solution that differs from the true solution by ~10^{-3} m in latitude and longitude, ~10^{-3} m in depth and ~10^{-6} s in origin time in the region examined.

Relocation of Events using Real Arrival Time Data

We proceeded to relocate the 1330 events in the CSZ using both methods, from which 1232 were relocated (92%). The remaining 98 events were not relocated, either due to quality of the data or because of missing arrival times. We only relocated events with more than four observations that were marked as good on the arrival time quality column. This avoids exact solutions of unknown quality when the number of observations and parameters are equal.

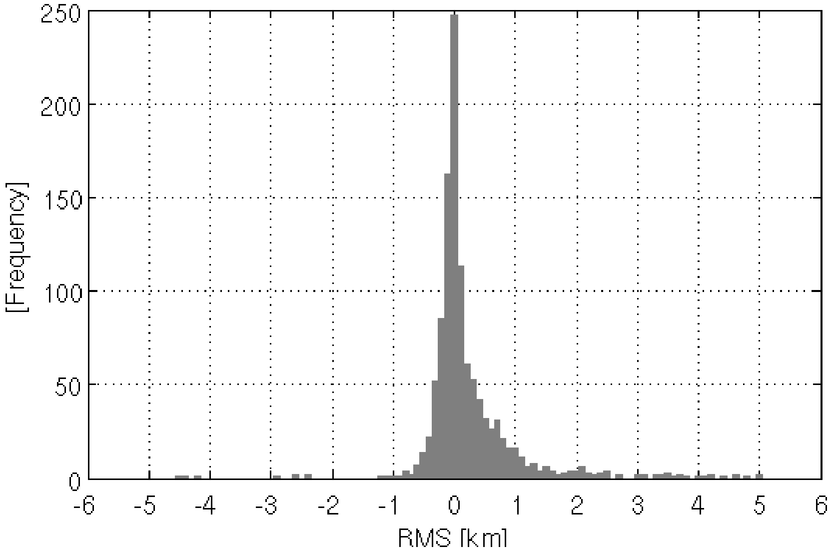

Figure 3. Histogram of the root mean square (rms) difference between the HYPOINVERSE and Bancroft solutions using Charlevoix seismic-zone real data. An $rms_D > 0$ represents a solution where Bancroft produced a better rms than HYPOINVERSE and $rms_D < 0$ represents a solution where HYPOINVERSE produced a better rms than Bancroft.

The rms residual difference for each earthquake, $rms_D = rms_H - rms_B$, (in which the subscripts D, H and B indicate difference, HYPOINVERSE and Bancroft) was calculated to quantify the comparison of the results from both methods (Figure 3). An $rms_D > 0$ represents a solution where Bancroft had a smaller rms than HYPOINVERSE, and vice versa. Figure 3 shows a clear tendency towards positive values, showing that Bancroft's solution has smaller residuals than HYPOINVERSE. Out of 1232 events, 548 solutions had $rms_D < 0$ while 684 had $rms_D > 0$. The asymmetry of the histogram shows that in the cases where HYPOINVERSE wins ($rms_D < 0$), the difference between the two solutions is generally small, as shown by the steep decline of the histogram. In the cases where Bancroft wins ($rms_D > 0$) the difference between the two solutions is generally larger, as shown by the wider histogram tail.

Quantifying solution quality

The most common GPS solution quality estimator is a DOP formulation. There are three DOP estimators (time, position and geometric), and they are computed using the diagonal elements of the covariance matrix associated with the design matrix. DOP represents the effect of the satellite-GPS receiver geometry on the accuracy of the solution (Leick, 1994) and is independent of measurement errors. Because the equation for earthquake location and GPS is the same, the DOP concept can provide a useful solution quality metric in the earthquake location problem. The precision with which a seismic network will be capable of locating an event is, therefore, also largely determined by the event-station geometry.

The DOP factor may be conceptually interpreted using the following ratio

$$DOP = \frac{\Delta(Output\ Location)}{\Delta(Measured\ Data)} . \qquad (25)$$

Ideally, small changes in the measured data should produce small variations in the result, which will yield small DOP values. When small changes in the input result in large changes in the result, this indicates that the solution is very sensitive to errors in the observations.

Using the classic least squares method and equation (2), each seismic station will provide an observation. The solution of the event hypocenter and origin time (X, Y, Z, t) can be found from the linearized version of equation (2). Assuming an over-determined system of equations, the matrix notation for a least squares solution has the form:

$$\overline{\mathbf{X}} = (\mathbf{A}^T \mathbf{A})^{-1} \mathbf{A}^T \mathbf{L} \tag{26}$$

in which **L** contains the observations (measured pseudoranges between event and seismic stations), $\overline{\mathbf{X}}$ contains the unknown parameters in vector form and **A** is known as the design matrix:

$$\mathbf{A} = \begin{bmatrix} \frac{(X - X_1)}{R_1} & \frac{(Y - Y_1)}{R_1} & \frac{(Z - Z_1)}{R_1} & -v \\ \frac{(X - X_2)}{R_2} & \frac{(Y - Y_2)}{R_2} & \frac{(Z - Z_2)}{R_2} & -v \\ \vdots & \vdots & \vdots & \vdots \\ \frac{(X - X_n)}{R_n} & \frac{(Y - Y_n)}{R_n} & \frac{(Z - Z_n)}{R_n} & -v \end{bmatrix} \tag{27}$$

and $R_n = \sqrt{(X - X_n)^2 + (Y - Y_n)^2 + (Z - Z_n)^2}$.

The term $(\mathbf{A}^T \mathbf{A})^{-1}$ is usually called the inverse of the normal matrix, or simply the covariance matrix **Q**. From this matrix, several DOPs can be calculated as

$$\begin{aligned}
&GDOP = \sqrt{Q_{11} + Q_{22} + Q_{33} + Q_{44}} \\
&TDOP = \sqrt{Q_{44}} \\
&VDOP = \sqrt{Q_{33}} \\
&HDOP = \sqrt{Q_{11} + Q_{22}}, \text{and} \\
&PDOP = \sqrt{Q_{11} + Q_{22} + Q_{33}}.
\end{aligned} \tag{28}$$

The geometric dilution of precision (GDOP) estimates the total effect on the solution of the combined network-event geometry and origin time determination. The Time Dilution of Precision (TDOP), Vertical Dilution of Precision (VDOP), Horizontal Dilution of Precision (HDOP) and Position Dilution of Precision (PDOP) reflect the precision of the network with respect to determination of the origin time, depth, epicenter, and hypocenter of an event, respectively.

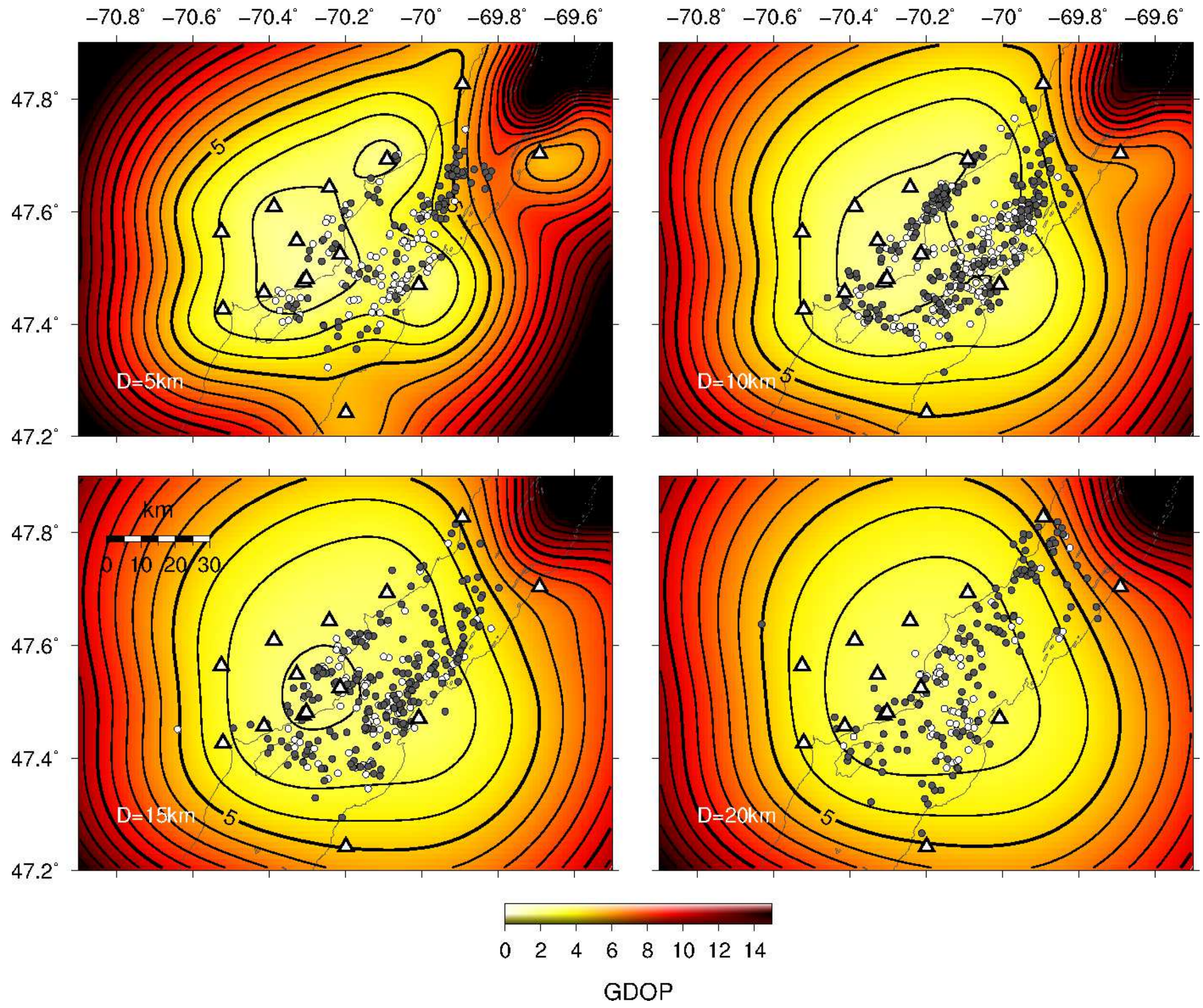

Figure 4. Example GDOP for the Charlevoix Seismic Network at depths of 5, 10, 15 and 20 km. Seismic stations are shown by triangles and catalog epicenters shown by circles, where dark circles are hypocenters with $RMS_D > 0$ and light circles are those with $RMS_D < 0$. Depth ranges on each depth slice are: 0-7.5 km; 7.5-12.5 km; 12.5-17.5 km; 17.5 km and deeper. The gray thin lines show Saint Lawrence River shore.

Because the covariance matrix does not depend on the observed data, the net effect of the geometry of the network on the solution can be estimated by calculating the covariance matrix as a function of hypocenter location. PDOP can be compared to the traditional method of using the azimuthal gap. The gap method estimates the quality of the epicenter by examining the gaps between azimuthally adjacent stations. PDOP and GDOP are more powerful as PDOP provides quality estimation for the hypocenter, and GDOP provides quality estimation for the hypocenter and origin time, based on the earthquake-station geometry. This procedure can be applied to the covariance matrix associated with the least squares design matrix of standard earthquake location programs, such as the various versions of the Hypo family, Double Difference, and 3D inversion.

Figure 4 shows a map of the Charlevoix seismic network with the resulting GDOP surface as a function of position for source depths of 5, 10, 15 and 20 km, and the Bancroft relocated catalog events. In GPS, a GDOP lower than five is considered acceptable or good, while anything greater is considered poor quality. This is an arbitrary limit that has been proved to provide a useful threshold for GPS solution quality estimation (Leick, 1994). We will later show that this limit can also be used in seismology to describe the boundary between good and poor quality locations. As expected, events occurring within clusters of seismic stations will be well located. Note that isolated stations near the edge of the network locally reduce GDOP, showing the reasonable result that a nearby station improves the quality of the location even though the azimuthal gap may be quite large.

It should also be noted that one can weight the inverse of the normal matrix, $(\mathbf{A}^T\mathbf{A})^{-1}$, in the usual way by using $(\mathbf{A}^T\mathbf{P}\mathbf{A})^{-1}$ where **P** is a matrix containing the weights. In this way we can take into account *a priori* information such as a station being located in a region where the data is noisier (e.g. station located in unconsolidated sediments, cultural noise, etc.) or any other information that can affect the confidence in the data.

We will now analyze the GDOP of the CSZ relocations by classifying them by rms_D. Figure 5 shows the histograms of the GDOP for the events that had $rms_D > 0$ and $rms_D < 0$. As expected, a large number of events occurred in the region of GDOP < ~4, which is a reasonable value within the seismic network limits, as seen on Figure 4. It should be noted, however, the

GDOP map in Figure 4 was constructed assuming that all the seismic stations provide arrival time data, which for some events is not true, resulting in a higher GDOP value for that particular hypocenter. In the region where GDOP < ~4, there are fewer events where Bancroft had a smaller rms than HYPOINVERSE. For the locations where GDOP > ~4, however, we observe the opposite, that is, there are more cases in which Bancroft had a smaller rms than HYPOINVERSE. This result confirms the finding of Bancroft (1985), that the described algorithm improves the accuracy in situations with large GDOP and validates the use of GDOP = 5 as a threshold between good and poor quality locations. In the particular case examined here, the threshold could be tightened to GDOP 4.

Discussion

In this article, we presented a comparison between the GPS and earthquake location inverse problems for a uniform half-space velocity model and found that they are analogous and expressed by the same equation. We then showed how to apply a noniterative algorithm developed to determine position using GPS data to the earthquake location problem in seismology. Advantages of the closed-form algorithm include no need for an initial estimate, improved efficiency as there is no need to iterate, and a numerically stable solution that improves accuracy in situations with large GDOP (Bancroft, 1985), as shown by Figure 5.

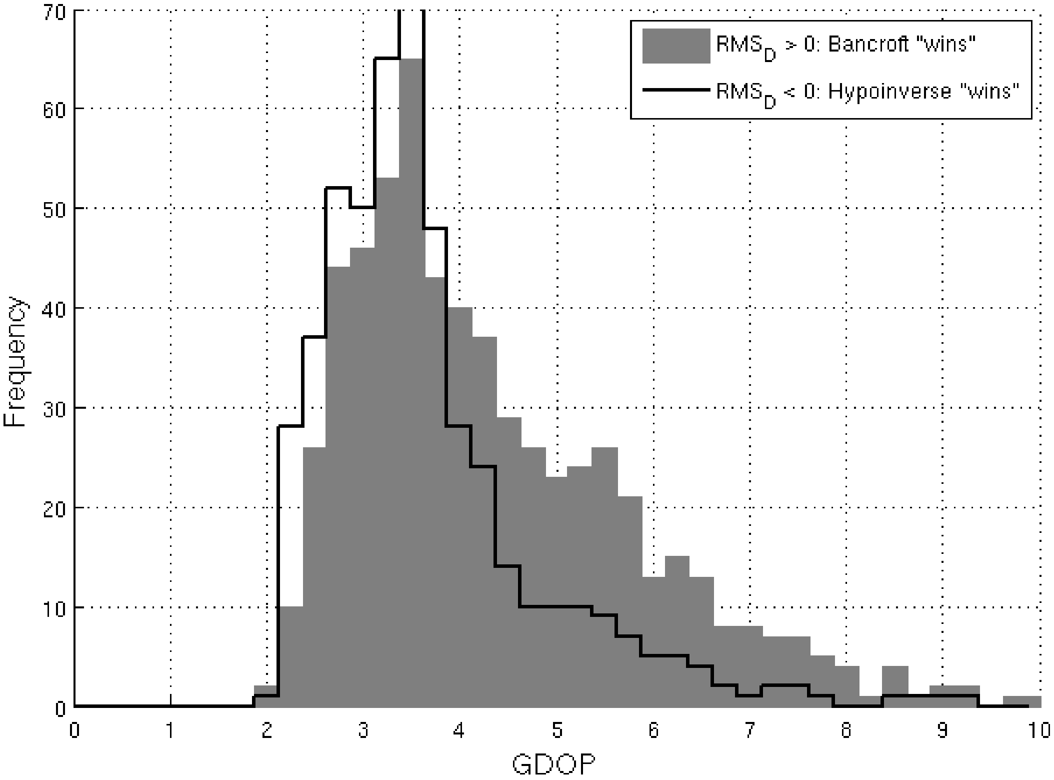

Figure 5. Histograms of the GDOP classified by rms value. For hypocenters with GDOP < ~4, Bancroft had fewer cases with smaller rms than HYPOINVERSE. For hypocenters with GDOP > ~4, Bancroft had more cases with smaller rms than HYPOINVERSE.

Despite this improvement in precision, some questions have arisen regarding the statistics and norm optimization criteria of the results obtained by the Bancroft algorithm when used in over-determined cases (Chaffee and Abel, 1994). A complete discussion of noniterative algorithms for solving the GPS location problems can be found in Sirola (2010). Although some drawbacks about these methods are discussed by Sirola (2010), such as numerical instability in certain cases of negative pseudorange measurements, these drawbacks do not present problems when applying the Bancroft algorithm for earthquake location.

There are two points from Sirola (2010), however, that deserve special attention. In over-determined systems, the Bancroft algorithm minimizes the sum of the fourth power of the errors, not the sum of the square of the errors (as in least squares). This is easily observed in equation (24) where one finds that the observations are squared. As a result, the solution is more influenced by outliers in the data than in least squares. Sirola calls these types of solutions "least-quartic". However, in cases where errors are of similar magnitude, this effect should not be critical for data without large outliers. Cases of events with stations providing large outlier data can be easily filtered by running the algorithm twice. A first run is used to calculate a first hypocenter from which outliers can be detected from the residuals; and a second run is used to obtain the final solution. A similar argument regarding the influence of the norm optimization criteria exists between the use of the L1 norm and the L2 norm (least squares) (Aster *et al.*, 2005). As it was shown by the test using real data, 55% of the solutions showed a reduction in rms residuals. In the cases where HYPOINVERSE wins ($rms_D < 0$), the difference between the two solutions is generally small. In the cases where Bancroft wins ($rms_D > 0$) the difference between the two solutions is generally larger.

Furthermore, the consequences of the application of this so-called least quartic solution can be observed in both synthetic and real data tests. During the synthetic tests (using random Gaussian noise), the normal distribution fits performed on the histograms revealed a larger dispersion on the Bancroft algorithm results. Because the Bancroft algorithm finds the exact solution but using a different norm optimization, the solutions have a tendency to be more dispersed than those using least squares. For the real data test, Bancroft had fewer results with lower rms than HYPOINVERSE in areas with low GDOP, most likely because HYPOINVERSE did not have convergence problems in these regions, making the norm optimization difference more evident (although the rms difference rarely exceeded ~1 km). In regions with large GDOP (in which standard-linearized location algorithms have higher chances of failing) the Bancroft algorithm provided more solutions with lower rms than did HYPOINVERSE because, although the norm optimization used in Bancroft provides a larger rms when compared with least squares, the linearized algorithm was unable to converge to a solution with lower rms. We should point out that there are many parameters to stabilize HYPOINVERSE that were not investigated and could potentially provide a lower rms. However, the application of Bancroft without any *a priori* information of the problem provided a better solution than that of HYPOINVERSE for 55% of the events.

The second point raised by Sirola (2010) is also related to the fact that the observations in equation (24) are squared as a consequence of applying the Minkowski functional. Dealing with the covariance of these squared measurements is more complicated. Moreover, applying traditional L1 or L2 norm statistics to least-quartic methods will not provide useful information about the solution quality. For seismologic applications, this point should not represent a problem, since it is fairly common to work with observations for which neither the error distribution nor the confidence level are known. Furthermore, quality estimators such as GDOP taken together with the residuals can provide information about the solution quality. Despite these drawbacks, the results of our tests show that Bancroft's synthetic solutions are comparable to those of HYPOINVERSE, with a higher dispersion due to the norm optimization difference. We have also shown that Bancroft improved 55% of the real locations. Additionally, we showed how to implement a set of simple and straightforward solution quality estimates (TDOP, HDOP, VDOP, PDOP, and GDOP) based on the source and seismic network geometry.

A homogeneous half-space is oftentimes too simple a model for determining earthquake locations. In certain cases, however, such as the CSZ, a uniform half-space is the most reasonable model. The Bancroft algorithm relies on a constant velocity medium (ray paths are straight lines), to make use of the Minkowski functional. At a minimum, the Bancroft algorithm can be used to obtain good initial earthquake locations (rather than using the location of the station with the first arrival) for use with more realistic non-homogeneous velocity models and corresponding iterative methods. The approach of using a closed-form solution as a starting position for a conventional iterative least squares method was also suggested by Sirola (2004). Although we have not tested this option, HYPOINVERSE requires setting a trial depth and origin time before running the location routine. If using Bancroft as a first rough approximation of the location, there would be no need to set these trial parameter values. The Bancroft method should also be directly applicable to relative location methods based on using a master event with a known location. In these methods, events near the master event are located with respect to the master event by using relative arrival times, assuming a constant velocity in the vicinity of the reference event. These are topics for future work.

Data and Resources

We would like to thank Maurice Lamontagne from the Geological Survey of Canada for providing the Charlevoix seismic-zone earthquake catalog data and metadata. Figure 4 was made using the Generic Mapping Tools version 5.1.1 (Wessel and Smith, 1998). MATLAB is available from www.mathworks.com/products/matlab.

Acknowledgements

D. Gómez is supported by the National Science Foundation (NSF) Office of Polar Programs grant, Collaborative Research: IPY: POLENET-Antarctica: Investigating Links between Geodynamics and Ice Sheets (NSF-ANT-062339 and supplement -0948103), and by the Center for Earthquake Research and Information, University of Memphis. We would like to thank Bill Barnhart, an anonymous reviewer, and Associate Editor Roland Bürgmann for critical reviews that improved the manuscript, and we thank Christine Powell for her contributions to this work.

References

Abel, J. S., and J. W. Chaffee (1991). Existence and uniqueness of GPS solutions, *IEEE Trans. Aero. Electron. Syst.* **27**, no. 6, 952–956, doi: 10.1109/7.104271.

Aster, R., B. Borchers, and C. Thurber (2005). *Parameter Estimation and Inverse Problems*, Academic Press/Elsevier, Burlington, Vermont.

Bancroft, S. (1985). An algebraic solution of the GPS equations, *IEEE Trans. Aero. Electron. Syst*. **AES-21**, 56–59.

Chaffee, J., and J. Abel (1994). On the exact solutions of pseudorange equations, *IEEE Trans. Aero. Electron*. Syst. **30**, no. 4, 1021–1030, doi: 10.1109/7.328767.

Geiger, L. (1910). Herbsetimmung bei Erdbeben aus den Ankunfzeiten, *K. Gessell. Wiss. Goett*. **4**, 331–349 (in German).

Geiger, L. (1912). Probability method for the determination of earthquake epicenters from the arrival time only, *Bull. St. Louis Univ*. **8**, 60–71.

Klein, F. W. (1978). Hypocenter location program HYPOINVERSE, *U.S. Geol. Surv. Open-File Rept*. 78-694, 113 pp

Lee, W. H. K., and S. W. Stewart (1981). Principles and applications of microearthquake networks, *Adv. Geophys. Suppl*. 2, 293 pp.

Leick, A. (2004). *GPS Satellite Surveying*, 3rd edition, John Wiley & Sons, New Jersey.

Minkowski, H. (1907/1908). Die Grundgleichungen für die elektromagnetischen Vorgänge in bewegten Körpern, *Nachrichten von der Gesellschaft der Wissenschaften zu Göttingen, Mathematisch-Physikalische Klasse*, 53–111 (In German)

Nievergelt, Y. (2000). A tutorial history of least squares with applications to astronomy and geodesy, *J. Comput. Appl. Math*. **121**, no. 1/2, 37–72, ISSN 0377-0427, doi: 10.1016/S0377-0427(00)00343-5.

Powell, C. A., M. M. Withers, H. R. DeShon, and M. M. Dunn (2010). Intrusions and anomalous V_P/V_S ratios associated with the New Madrid seismic zone, *J. Geophys. Res*. **115**, no. B08311, doi: 10.1029/2009JB007107.

Pujol, J., and R. Smalley Jr. (1990). A preliminary earthquake location method based on a hyperbolic approximation to travel times, *Bull. Seismol. Soc. Am*. **80**, 1629–1642.

Sirola, N. (2004). A versatile algorithm for local positioning in closed form, *Proceedings of the 8th European Conference GNSS 2004,* Rotterdam, The Netherlands, 16–19 May 2004.

Sirola, N. (2010). Closed-form algorithms in mobile positioning: Myths and misconceptions, *7th Workshop Positioning Navigation and Communication (WPNC)*, Dresden, Germany, 11–12 March 2010, 38–44, doi: 10.1109/WPNC.2010.5653789.

Thurber, C. (1985). Nonlinear earthquake location: Theory and examples, *Bull. Seismol. Soc. Am.* **75**, 779-790.

Wessel, P., and W. H. F. Smith (1998). New, improved version of generic mapping tools released, *Eos Trans. AGU* **79**, no. 47, 579–579, doi: 10.1029/98EO00426.

CHAPTER 2

Co-seismic deformation of the 2010 Maule, Chile earthquake: Validating a least squares collocation interpolation

Published in Journal of the Argentine Association of Geodesy and Geophysics

Introduction

Mathematical representations of observational data are comprised of deterministic and stochastic models. A deterministic model is defined by a functional relation between the observed data and the model parameters describing the physical characteristics of the phenomenon under study. In inverse theory, this model is usually presented in the form of a matrix multiplication as $\mathbf{Ax}=\mathbf{L}$, where $\mathbf{A}$ represents the functional relation (also known as the design matrix), $\mathbf{x}$ is a vector of model parameters and $\mathbf{L}$ is the observation vector (Sevilla, 1987).

The stochastic model is the mathematical representation of the random behavior of the phenomenon, which can be described in terms of a probability density distribution. The statistical expectation of the variables is given by means of the covariance matrices, which describes the random behavior of the data and model parameters (Moritz, 1972). During least squares adjustment, the stochastic model is often used to weight the data by multiplying the inverse of the covariance matrix, $\sum^{-1}$, with the *a priori* unitary variance ($\mathbf{W}=\sigma_0{}^2\mathbf{\Sigma}^{-1}$ where $\sigma_0=1$) to obtain the so-called weighting matrix. If we have independent direct observations, the covariance matrix will only have elements on the diagonal that correspond to the expected variance of the observations, thus representing their probability distribution. This implies that we at least know the mean (assumed to be zero) and variance of the probability distribution that governs the random behavior of the observations.

When the physical laws that govern the phenomena under study are unknown or their expressions are too complicated to be derived, we can consider the observations to be random variables of a particular probability density distribution with their mean located at the observation value. In this case, we can fit the deterministic part of the observed variable with a convenient function (such as a polynomial) that has no physical meaning (Vieira et al., 2009). To apply geostatistical tools such as least squares collocation (LSC), it is required that the misfit between the data and the function describing the deterministic part of the problem produces residuals with a probability distribution that has a mean statistically equal to zero.

By analyzing the statistical behavior of a variable under study, i.e. describing its stochastic model, the LSC method can be used to obtain spatial or temporal predictions (interpolations) of the variable of interest. This stochastic model description can be done analytically to find the exact expression of the so-called covariance function. In most cases, however, this analytical form may be very complicated and hard to derive. Nevertheless, Moritz (1978) showed that although the statistical interpretation of the covariance function provides a solution with a minimum root mean square (rms) interpolation error, any expression can be used to describe the covariance of the data, as long as the resulting covariance matrices are symmetric and positive definite. This is generally done by fitting a suitable expression to the empirical covariance data, which will provide a simple and optimal way to obtain a result that is within a certain tolerance of the minimum rms solution (Moritz, 1978).

This procedure has been successfully applied in geodesy for gravity and other variables such as the velocity field of the Caribbean and South American plates in the *Sistema de Referencia Geocéntrico para las Américas* (SIRGAS) 2000 reference frame (Drewes and Heidbach, 2012). Recently, the application of LSC to predict the elastic deformation of the 2010

Maule earthquake was proposed by Drewes and Sánchez (2013) during the SIRGAS meeting in Panamá City. By analyzing the empirical covariance data of the available GPS sites during the time of the earthquake, they have constructed a one degree grid in latitude and longitude of predicted co-seismic deformation to interpolate the displacements that relate the pre-seismic reference frame with the post-seismic one. By fitting the ongoing post-seismic deformation (using the same technique), they have proposed a practical way to "connect" these two reference frames.

As it was previously discussed, the LSC method has proved to be a reliable technique to interpolate gravity observations, since the gravity equipotential is oftentimes a continuous and smooth surface. However, Darbeheshti and Featherstone (2009) showed that in some cases, where the gravity field shows sharper changes across faults and other geologic features, non-stationary LSC must be used in order to better interpolate the equipotential surface. Because the deformation of an earthquake can also show abrupt changes in the near-field (specially across fault lines), which might not be correctly sampled due to the lack of observations, a deeper analysis of the problem must be conducted in order to understand the capabilities and limitations of this interpolation method.

To better test the proposed application of LSC to elastic deformation produced by the Maule earthquake, we have simulated the co-seismic deformation by means of a finite element model (FEM) using a finite element code for dynamic and quasistatic simulations of crustal deformation called Pylith (Aagaard et al., 2013). This simulation provides a convenient way to solve a forward LSC problem, by knowing *a priori* the magnitude of the deformation. These tests have revealed that the application of the LSC method to deformation data cannot correctly interpolate the deformation in the near-field, using the available GPS dataset. Nevertheless, the far-field interpolation results are in good agreement with the synthetic deformation values from the FEM. These results suggest that it might be necessary to consider other LSC approaches such as non-stationary covariance functions, although this will not mitigate the effect of the lack of observations in some regions where the FEM shows a complex elastic response.

The least squares collocation method

Using both deterministic and stochastic components, the observation of a physical quantity may be expressed as:

$$\mathbf{z} = \mathbf{A}\mathbf{x} + \mathbf{s} + \mathbf{n}, \tag{1}$$

where $\mathbf{z}$ is the observed variable, $\mathbf{A}$ is the design matrix, $\mathbf{x}$ is the model parameters vector, $\mathbf{Ax}$ represents the deterministic component, $\mathbf{s}$ is the stochastic component signal vector, and $\mathbf{n}$ is the measurement noise.

Assuming that the noise measurement in (1) is uncorrelated between independent observations, the stochastic signal $\mathbf{s}$ and noise $\mathbf{n}$ may be obtained by evaluating the following expression

$$\mathbf{s} + \mathbf{n} = \mathbf{z} - \mathbf{A}\mathbf{x}. \tag{2}$$

The left hand side of equation (2) contains the residuals that are not represented by the deterministic model. If the deterministic model has no physical meaning, i.e. the design matrix $\mathbf{A}$ is an arbitrary fitting function that produces residuals with a mean that is statistically equal to zero, obtaining the residuals $\mathbf{s} + \mathbf{n}$ can be interpreted as a detrending of the observations. The necessity of detrending the data to apply LSC will be discussed later in this section. Quantity $\mathbf{s}$ (also known as the stochastic signal) can be modeled using a stochastic model defined by the covariance matrix **C** with elements

$$C_{ij} = E(s_i, s_j) \tag{3}$$

where $E(s_i, s_j)$ is the mathematical expectation operator, C_{ij} is the ij element of the covariance matrix $\mathbf{C}$ and s_i, s_j are the ij elements of the stochastic signal $\mathbf{s}$. Since the noise term $\mathbf{n}$ is uncorrelated for independent measurements, the measurements noise matrix can be written as

$$\mathbf{C_{rr}} = \begin{bmatrix} \frac{1}{\sigma^2} & 0 & 0 \\ 0 & \ddots & 0 \\ 0 & 0 & \frac{1}{\sigma^2} \end{bmatrix}. \tag{4}$$

where σ^2 is the variance of the observations. We are using a uniform variance because we are assuming the measurements are obtained from a single observational method (e.g. GPS). The covariance matrix will then be the sum of (3) and (4) which yields:

$$\mathbf{C_{ss}} = \mathbf{C} + \mathbf{C_{rr}} \tag{5}$$

As previously discussed, the covariance of the measurement errors is equal to zero but the covariance of the stochastic signal is non-zero, allowing us to separate them and model the stochastic signal.

Obtaining an exact mathematical expectation expression for *C* in (5) is oftentimes a difficult task. To avoid these complications, a function can be fit to the covariance data to obtain the so-called covariance function (Moritz, 1978). This function must satisfy the conditions that the resulting covariance matrices are symmetric and positive definite. To obtain the covariance data, observation residuals from equation (2) have to be grouped into "bins" according to their pair distance. Then, the covariance for each distance d_j will be the average of the covariance of the *j*'s bin, which contains N_j pairs and can be calculated as:

$$Cov(d_j) = \frac{1}{N_j} \sum_{k,i}^{N_j} \Delta(x_k, y_k)\,\Delta(x_i, y_i) \tag{6}$$

where Δ is the residual from equation (2). A function that describes the general characteristics of the covariance data as a function of distance must be used to fit the empirical covariance data points obtained from (6). The most common types of functions used to fit covariance data are the Cauchy (Moritz, 1980):

$$C(d) = \frac{C_0}{1 + \left(\frac{d}{r_1}\right)^2} \tag{7}$$

and Gaussian expressions (Kearsley, 1977):

$$C(d) = C_0\left(1-\frac{d^2}{r_2^2}\right)\exp\left(-\frac{d^2}{r_1^2}\right) \tag{8}$$

for stationary cases, where C_0 is the *a priori* variance, d is the distance and r_1, r_2 are the correlation lengths. Equivalent non-stationary expressions for (7) and (8) are presented in Darbeheshti and Featherstone (2009).

Detrending the data using equation (2) is a necessary step before finding the covariance function. In two dimensional data sets (scalar fields) with trends, the expectation value of the field changes as a function of position. The so-called intrinsic hypothesis states that the expectation value of the scalar should not be a function of position (Ligas and Kulczycki 2010; Vieira et al., 2009), thus the detrending of the data is a necessary step to satisfy the intrinsic hypothesis. To verify that the data set satisfies this hypothesis, one can plot the semi-variogram of the variable under study. When the semi-variogram has a clearly defined and stable plateau or sill at the value of the a priori variance, the intrinsic hypothesis is satisfied and therefore, geostatistical analysis such as kriging or LSC can be applied to the data (Vieira et al., 2009).

Once the covariance function has been estimated, the values at unmeasured points can be "predicted" using LSC:

$$\mathbf{s}_p = \mathbf{C_{zs}}\mathbf{C_{ss}}^{-1}\mathbf{z} \tag{9}$$

where **z** is the observation vector, $\mathbf{C_{ss}}$ has been already defined and $\mathbf{C_{zs}}$ is covariance matrix of the predicted points. The $\mathbf{C_{zs}}$ matrix is calculated using the same covariance function as for $\mathbf{C_{ss}}$, since the distances between observation and prediction points are known.

After finding the stochastic signal $\mathbf{s}_p$, the complete observation estimate can be calculated by adding the detrending function or deterministic model back. So, the complete predicted data can be found using the following expression:

$$\mathbf{z}_p = \mathbf{A}\mathbf{x} + \mathbf{s}_p \tag{10}$$

If the data has no trend, then the result from equation (9) provides the desired prediction.

The LSC has been successfully applied to a number of problems, such as topographic interpolation, gravity measurements and geodetic reference frame velocities. Its application to other fields, such as elastic deformation, can be done only after validating that the intrinsic hypothesis is satisfied.

For the elastic deformation case, this validation might be a difficult task to perform, as the available data to perform semi-variogram plots can be very limited. Moreover, since the deformation signal can have a very complicated spatial structure in unsampled regions, the direct use of LSC might provide “visually” good results that do not match the actual deformation field. To test and validate the procedure, we have obtained synthetic data to test the LSC application to elastic deformation.

Synthetic data for forward validation

In order to obtain synthetic data to test the application of LSC to elastic deformation data, we have used the finite element model (FEM) code Pylith. The finite element method is a numerical technique for finding approximate solutions for governing differential equations. Pylith is a numerical approach to solve dynamic and quasistatic elasticity problems.

The construction of a FEM starts by defining a mesh of nodes to which the finite element method will be applied. The complexity of the model geometry and boundary conditions vary from problem to problem. Since the purpose of our FEM is to obtain an approximate co-seismic deformation field to use in our synthetic LSC test, we only include in the model first order characteristics that have the greatest impact on co-seismic deformation.

As the region under consideration extends from Chile to eastern Argentina, a flat earth or half-space model is inappropriate to model the deformation field and therefore, we have used a layered spherical FEM mesh. Layer thickness and elastic properties are taken from the Preliminary Earth Model (PREM) (Dziewonski and Anderson, 1981). One of several advantages of using a spherical FEM mesh is that there is no necessity to define free slip boundary conditions, as deformation in a sphere is self constrained, since the nodes that form the FEM mesh form a closed surface.

After the FEM mesh geometry is defined, a fault model must be used to simulate the slip produced by the earthquake. Several finite fault models are available based on inversion of InSAR data, GPS or both (Tong et al., 2010; Pollitz et al., 2011; Lorito et al., 2011; Moreno et al., 2012). Because of the particular characteristics of our FEM model, we have inverted our own finite fault model using GPS data only. The input data to produce the finite fault slip was a combination of the co-seismic displacement solutions obtained from the Central Andes GPS Project (Pollitz et al., 2011) and the Instituto Geográfico Nacional (IGN). This inversion yields the approximate slip distribution on a predefined fault surface. As our fault surface, we have adopted the USGS South American subduction zone slab model (Hayes et al., 2012). We will not discuss the finite fault inversion process and modeling techniques since they are out of the scope of this paper.

Using the FEM mesh and the finite fault models, we run Pylith to produce two datasets: 1) the co-seismic displacements at the same locations where the continuous GPS (CGPS) stations are located and 2) co-seismic displacements on a 0.5º grid in latitude and longitude where the LSC will be used to interpolate the earthquake's deformation.

Before continuing to the LSC tests, we will show the similarity of the synthetic data to the real co-seismic deformation. This comparison will validate the use of this synthetic dataset to apply LSC as if this was the observed deformation field. Figure 1 shows the comparison between the observed and the FEM co-seismic deformation field. Misfits between the model and the GPS observations can be observed, in both the near and far-field. However, these differences never exceed 25 cm, as shown by Figure 2. Taking into account previous simulation residuals (Tong et al., 2010; Pollitz et al., 2011; Lorito et al., 2011; Moreno et al., 2012), the directions of the displacements are in very good agreement with the directions reported by the GPS observations (except for a few points), showing that the model represents the crustal elastic response of the 2010 Maule earthquake well. The misfits are probably due to a combination of the roughness of the mesh and the simplicity of the finite fault model. Since the objective of this paper is to test the LSC of elastic deformation, we conclude that the obtained synthetic dataset is adequate to run our tests.

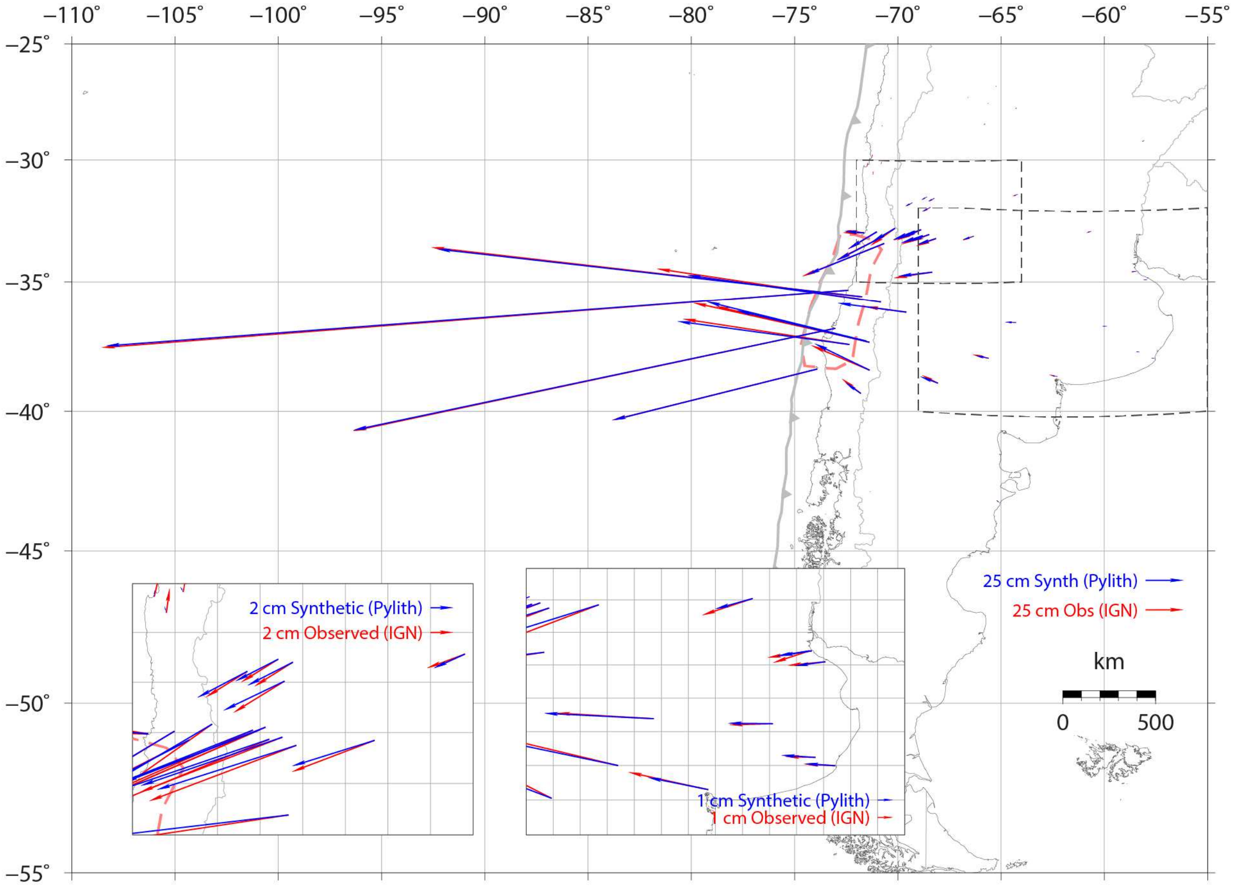

Figure 1. Comparison between observed and FEM co-seismic deformation using GPS solutions provided by the Central Andes Project (Pollitz et al., 2011) and Instituto Geográfico Nacional, Argentina. Blue arrows: modeled displacements; red arrows: observed displacements; red dashed polygon: rupture zone defined by aftershocks.

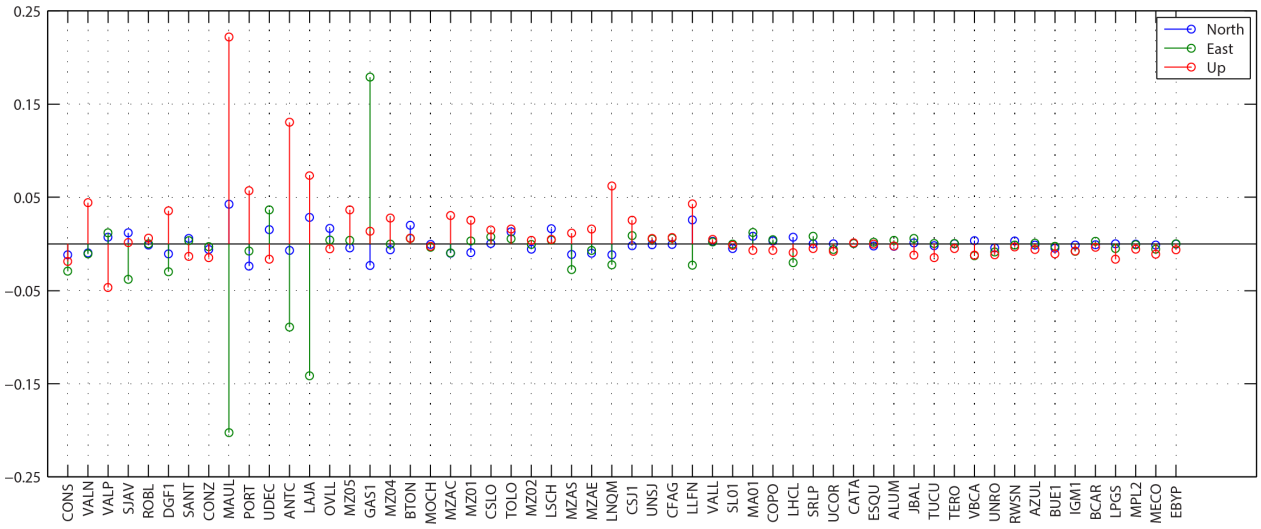

Figure 2. Station list, ordered by increasing distance from the rupture zone, with differences between model and GPS observations for north, east and up components. Only six stations exceed the 5 cm limit, all of them in the near-field. These differences are most likely due to model geometry and slip inversion simplifications.

Elastic deformation semi-variogram

We have produced semi-variogram plots of the elastic deformation as in Vieira et al., (2009) to investigate if the data satisfy the intrinsic hypothesis, which can be verified by the presence of a plateau or sill in the semi-variogram plot. Unlike the empirical covariance function, which describes the similarity of the data as a function of distance, the semi-variogram provides a measure of the dissimilarity between pairs of observations at a certain distance range (Ligas and Kulczycki, 2010).

The first assumption required to apply the LSC method (with a stationary covariance function) is that the earthquake's deformation data describes a stationary process. This means that the selected covariance function that describes the stochastic behavior of the data is the same for the entire domain. Although the observed elastic deformation data does not satisfy this assumption, since the deformation field does not have a mean equal to zero (as seen on Figure 1), we can assume an approximate stationary covariance function after detrending the data.

We followed the procedure of Vieira et al., (2009) to obtain the lowest degree detrending polynomial that produces a sill in the semi-variogram plot. Vieira et al., (2009), however, does not discuss the maximum degree for the detrending polynomial, which has to take into account the number of available data points. If the degree of the polynomial is too high and the data points are few, we can obtain spurious oscillations and edge effects due to a badly constrained inversion of the polynomial parameters. From this analysis, we have found that the maximum polynomial degree allowed by the FEM grid is six while the maximum degree for the synthetic GPS solution (that of the FEM at the CGPS sites) is only two. The consequences of detrending the data with these two different polynomials will be discussed later.

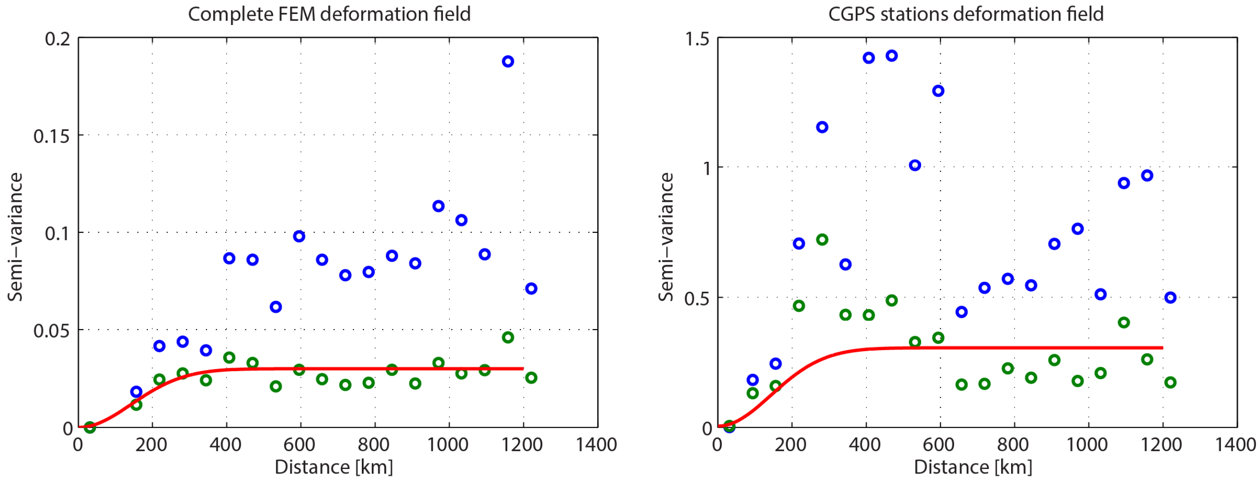

Figure 3. Semi-variogram of the deformation field (0.5º by 0.5º grid), left. Blue circles: deformation without detrending; green circles: detrended deformation; red line: Gaussian semi-variogram model. Right, semi-variogram of the deformation field sampled at the CGPS stations.

Figure 3 (left) shows the semi-variogram plot (see data sources section) of the east component co-seismic deformation for the FEM grid (blue circles), the detrended data semi-variogram (green circles) and the semi-variogram model (red line). We will only present the results for the east component, since most of the deformation was east-west, however, this procedure was also applied to the north-south component as well. We assumed the following Gaussian model:

$$\gamma(d) = C_0 + C_1\left(1 - \exp\left(-3\left(\frac{d}{r}\right)^2\right)\right), \tag{11}$$

where C_0, C_1 are the a priori variance and covariance (sill), d is the distance between point pairs and r is the correlation length (Vieira et al., 2009).

From Figure 3 (left), we observe that the semi-variogram presents an approximate plateau or sill that suggests that the deformation field describes a stationary process. Therefore, after detrending the data using the lowest degree polynomial that produces a sill (two variable, degree five), LSC can be applied using a unique covariance function to describe the stochastic behavior of the deformation field. If we plot the semi-variogram using only the available GPS data (i.e. using only the observations at the CGPS stations) the semi-variogram does not present a clear sill (Figure 3, right). This behavior can be explained by the low number of CGPS observations. Because the maximum polynomial degree that this dataset allows is two, we cannot increase the degree of the polynomial, which would allow the detrending function to produce a semi-variogram with a sill, as in Figure 3, left.

Because less data points are available when using the CGPS observations, the degree of the polynomial has to be low, as discussed earlier. Degree two, however, is not enough to correctly detrend the deformation field (due to the roughness of the co-seismic displacements) and therefore, the semi-variogram does not show a clear sill. When more data points are added to the polynomial fit (as in Figure 3, left), we can increase the polynomial degree and the detrending procedure correctly removes the trend, producing a sill in the semi-variogram. This result suggests that a minimum number of observations exists for which the detrending procedure produces a dataset to which LSC can be applied (Gómez et al., 2014). However, only a limited number of GPS stations were available at the time of the earthquake. Although other datasets could be added such as campaign observations and non-publicly available GPS solutions, at this time we have only used the currently available data (see the acknowledgements section).

Darbeheshti and Featherstone (2009) showed that when the stochastic behavior of the variable under study cannot be described using a stationary covariance function, either a non-stationary covariance function or a partitioned domain can be used to apply LSC. Following Darbeheshti and Featherstone (2009), and to avoid discontinuities in our interpolated deformation field, we have partitioned the domain in triangular sections to apply a stationary covariance function using the data from the nearby locations of the sub-domain. Using this partitioned domain, we applied LSC to obtain an interpolated deformation field that we compared against the FEM to validate our results.

Results

We proceeded to apply LSC to the deformation field to produce an interpolated field on a 0.5° grid in latitude and longitude. In order to reduce the non-stationary characteristics of the elastic deformation field, we have partitioned the domain into sub-domains defined by triangles that enclose similar deformation observations. One covariance function was calculated for each sector using the nearby data. Because bounding triangles share the same observations for two vertices, the boundary patching discussed by Darbeheshti and Featherstone (2009) is less visible than when taking arbitrary rectangular limits. Nevertheless they exist and some smoothing procedure should be applied to remove it, although we did not apply any.

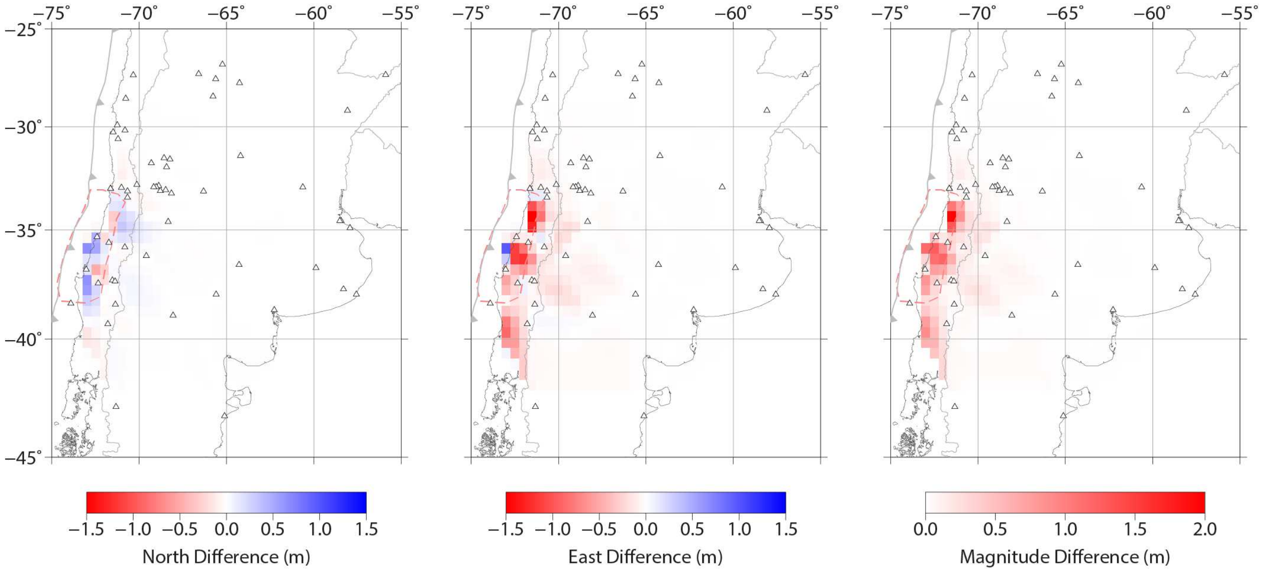

Figure 4. Differences between LSC and synthetic co-seismic deformation. Left: North difference; middle: east difference; right: total (magnitude) difference. Triangles: GPS stations used to apply LSC.

Figure 4 shows the results of the LSC deformation field. The mid- to far-field LSC interpolation is in good agreement with the FEM results. The good fit of the interpolation to the FEM model can be attributed to the smoothness of the far-field data. This smooth behavior of the deformation field yields a subdomain that can be correctly described as stationary process. Regardless of this good fit, some areas could benefit from extra measurements, although the differences never exceed five to nine millimeters. We should also mention that after analyzing the far-field stochastic component of the interpolation, calculated using equation (9), we found that the deformation field was almost completely modeled using the detrending polynomial. As a result, the residual from equation (2) was very small and the stochastic signal obtained with the LSC method had a very low influence on the final solution, obtained from equation (10).

In the near-field, however, it can be seen that the LSC produced outliers of up to 1.5 meters. These results are in agreement with the semi-variogram obtained during the previous section, which revealed that with the number of available observations, the dataset trend cannot be correctly removed. Moreover, partitioning the domain introduces an important limitation. Because there are fewer data points to fit the polynomial function (since we only use the data inside the partitioned domain), we cannot use a high degree polynomial to remove the trend. If short wavelength deformation exists in the subdomian that cannot be absorbed by the lower degree polynomial, the detrended dataset will not satisfy the intrinsic hypothesis.

In the northern and southern edges of the rupture zone (marked in Figure 4 with a red dashed line), some of the interpolated points are highly influenced by the lack of observations in their neighborhood. In these regions, due to the edge effects of the fault rupture, the behavior of the deformation changes very rapidly when crossing outside the rupture zone boundary. The same effect can also be observed in the central section of the rupture zone, as this region also presents rapid changes in deformation vector orientation. This observation suggests that by incorporating more measurements to the LSC, the near-field interpolation could be improved. However, these observations might not be available or could be highly influenced by post-seismic deformation. Since the post-seismic deformation produced by the earthquake affects the velocity of the GPS stations, obtaining a direct measurement of the co-seismic jump (e.g. from campaign stations observations) might provide an unreliable value that will affect the result of the interpolation. Other options, such as using InSAR data could also be used to increase the number of observations, although they will also be affected by the post-seismic deformation.

Discussion and conclusions

The application of LSC to predict the elastic deformation of the 2010 Maule earthquake was proposed by Drewes and Sánchez (2013), where they showed some results of the interpolation process. To better test the proposed application of LSC, we produced synthetic observations for the earthquake using a FEM. These observations allowed us to analyze and quantify the results of the LSC method of elastic deformation data.

The semi-variogram plot of synthetic data showed that when using the available number of CGPS stations (Figure 3, right), the semi-variogram does not clearly show a sill and therefore, the intrinsic hypothesis is not satisfied, resulting in inaccurate interpolations, especially in the near-field. This shortcoming can be resolved by either using more observations (since we showed that the semi-variogram of the whole deformation field presents a more stable sill) or a partitioned domain to estimate individual covariance functions. A third option that we did not investigate is the application of non-stationary covariance functions as in Darbeheshti and Featherstone (2009).

Although obtaining more observations is the best option, such observations might not exist, or might not be sufficiently accurate for geodetic and geophysical applications. Campaign data obtained a few months after the main event, for example, will be affected by post-seismic deformation. We could resolve this shortcoming by estimating the ongoing post-seismic deformation to predict the coordinates at the epoch immediately after the earthquake, although this procedure introduces an undetermined uncertainty. We note, however, that the post-seismic effect in campaign data (and InSAR) could be negligible for the purposes of creating an interpolated deformation field using LSC, depending on the intended application of such interpolation.

At this time, instead of adding more observations, we have partitioned the domain into triangular sections of similar deformation to obtain individual covariance functions of these subdomains. Partitioning the domain, however, introduces an important limitation. Because there are fewer data points to fit the polynomial function (since we only use the data inside the subdomains), we cannot use a high degree polynomial to remove the trend. If there is a significant deformation change in the subdomain that cannot be absorbed by the lower degree polynomial, the detrended dataset will not satisfy the intrinsic hypothesis. An alternative that we tested was to detrend the whole domain followed by partitioning. This option does not provide good results, since the covariance function should be estimated using the entire detrended domain (not just a portion of the detrended domain) to guarantee that the intrinsic hypothesis is satisfied.

We proceeded to interpolate the deformation field using the proposed partitioned domain. The far-field predictions show overall good agreement with the FEM data. In the near-field, nonetheless, collocation produces large outliers at the edges of the rupture zone (of ~1.5 m). The rapid change of the deformation field is characteristic of thrust fault earthquakes such as the 2010 Maule event, which prevents the LSC method from correctly interpolating the deformation field with the available GPS observations.

Moreover, a smoothing effect in the near-field was observed after applying LSC, which is probably further evidence for a lack of observations. A better partitioning of the near-field domain, the use of non-stationary covariance function and the addition of extra observations could improve the results. Nevertheless, the far-field collocation showed that the detrending polynomial can “absorb” almost all of the deformation, leaving a very small residual for the stochastic component to model. This suggests that, if the necessary observations were added during the near-field collocation procedure, the elastic behavior will be smooth enough between samples so that other interpolation techniques can be applied to the data.

Based on the results presented here, we found that LSC is not an appropriate tool to “predict” elastic deformation using the available dataset. We have shown that more observations are needed in order to obtain a dataset that satisfies the intrinsic hypothesis. We also note that the complexity of the deformation field can be reproduced by a physical representation of the problem, using the equations of elasticity.

To provide observations of the co-seismic deformation between CGPS stations, we propose using a FEM such as that used to obtain the synthetic data presented here. Even with a very rough model, we showed that the FEM produced a deformation field that is in very good agreement with the CGPS observations. By using a better mesh and a more complex finite fault model, we hope to obtain a more accurate representation of the near and far-fields. The development of such model is under study and will be presented in the near future.

Acknowledgements

We would like to thank Benjamin Brooks and James Foster for providing additional datasets that were used for this work. We would like to thank Wolfgang Schwanghart for providing his semi-variogram code calculation (see Data sources section). The authors would like to thank two anonymous reviewers for their insightful comments and suggestions that have contributed to improve this paper.

This work was supported by the NSF Office of Polar Programs grant Collaborative Research: IPY: POLENET-Antarctica: Investigating Links between Geodynamics and Ice Sheets (NSF-ANT-062339 and supplement -0948103) and the Center for Earthquake Research and Information, University of Memphis.

Data sources

Pylith web page: http://geodynamics.org/cig/software/pylith/. Semi-variogram code provided by Wolfgang Schwanghart: http://www.mathworks.com/matlabcentral/fileexchange/29025-ordinary-kriging. USGS slab 1.0 model obtained from: http://earthquake.usgs.gov/data/slab/. Maps were made using the Generic Mapping Tools version 5.1.1 (Wessel and Smith, 1998)

References

Aagaard, B.T., Knepley, M.G., Williams, C.A., (2013). A domain decomposition approach to implementing fault slip in finite-element models of quasi-static and dynamic crustal deformation. Journal Geophysical Research Solid Earth, 118: 3059–3079. doi:10.1002/jgrb.50217.

Darbeheshti, N., Featherstone, W.E., (2009). Non-stationary covariance function modelling in 2D least-squares collocation. Journal of Geodesy, 83: 495–508. doi:10.1007/s00190-008-0267-0.

Drewes, H., (1978). Experiences with least squares collocation as applied to interpolation of geodetic and geophysical quantities, in: Proceedings of Symposium on Mathematical Geophysics, Caracas.

Drewes, H., Heidbach, O., (2012). The 2009 Horizontal Velocity Field for South America and the Caribbean, in: Kenyon, S., Pacino, M.C., Marti, U. (Eds.), Geodesy for Planet Earth. Springer Berlin Heidelberg, Berlin, Heidelberg, pp. 657–664.

Drewes, H., Sánchez, L., (2013). Modelado de deformaciones sísmicas en el mantenimiento de marcos geodésicos de referencia. Presented at the SIRGAS 2013 Meeting, Instituto Geográfico Nacional Tommy Guardia, Panama City, Panama.

Dziewonski, A.M., Anderson, D.L., (1981). Preliminary reference Earth model. Physical Earth Planet. Inter. 25: 297–356.

Gómez, D., Smalley, R., Piñón, D., Cimbaro, S., (2014). Colocación por mínimos cuadrados de la deformación co-sísmica del sismo de Maule, Chile 2010: Estimación de observaciones mínimas. Presented at the XXVII Reunión Científica de la Asociación Argentina de Geofísicos y Geodestas, San Juan, Argentina. doi:10.13140/2.1.4254.9445

Hayes, G.P., Wald, D.J., Johnson, R.L., (2012). Slab1. 0: A three-dimensional model of global subduction zone geometries. Journal Geophysical Research. Solid Earth, 1978–2012, 117.

Kearsley, W., (1977). Non-Stationary Estimation in Gravity Prediction Problems. DTIC Document.

Ligas, M., Kulczycki, M., (2010). Simple spatial prediction-least squares prediction, simple kriging, and conditional expectation of normal vector. Geodesy and Cartography. 59: 69–81.

Lorito, S., Romano, F., Atzori, S., Tong, X., Avallone, A., McCloskey, J., Cocco, M., Boschi, E., Piatanesi, A., (2011). Limited overlap between the seismic gap and coseismic slip of the great 2010 Chile earthquake. Nature Geosciences. 4: 173–177. doi:10.1038/ngeo1073

Moreno, M., Melnick, D., Rosenau, M., Baez, J., Klotz, J., Oncken, O., Tassara, A., Chen, J., Bataille, K., Bevis, M., Socquet, A., Bolte, J., Vigny, C., Brooks, B., Ryder, I., Grund, V., Smalley, B., Carrizo, D., Bartsch, M., Hase, H., (2012). Toward understanding tectonic control on the Mw 8.8 2010 Maule Chile earthquake. Earth Planet. Science Letter. 321-322: 152–165. doi:10.1016/j.epsl.2012.01.006.

Moritz, H., (1980). Advanced physical geodesy. Advanced Planet. Geol. 1.

Moritz, H., (1978). Least-squares collocation. Review Geophysics, 16: 421–430.

Moritz, H., (1972). Advanced least-squares methods. Department of Geodetic Science, Ohio State University Columbus, USA.

Pollitz, F.F., Brooks, B., Tong, X., Bevis, M.G., Foster, J.H., Bürgmann, R., Smalley, R., Vigny, C., Socquet, A., Ruegg, J.-C., Campos, J., Barrientos, S., Parra, H., Soto, J.C.B., Cimbaro, S., Blanco, M., (2011). Coseismic slip distribution of the February 27, 2010 Mw 8.8 Maule, Chile earthquake: CHILE EARTHQUAKE COSEISMIC SLIP. Geophysical Research Letter, 38, n/a–n/a. doi:10.1029/2011GL047065.

Sevilla, M., (1987). Colocación mínimos cuadrados. Publicación Univ Complut. Fac Cienc. Mat Inst Astron. Geod. Tong, X., Sandwell, D., Luttrell, K., Brooks, B., Bevis, M., Shimada, M., Foster, J., Smalley, R., Parra, H., Báez Soto, J.C., Blanco, M., Kendrick, E., Genrich, J., Caccamise, D.J., (2010). The 2010 Maule, Chile earthquake: Downdip rupture limit revealed by space geodesy: DOWNDIP RUPTURE MAULE, CHILE EARTHQUAKE. Geophysical Research Letter, 37, n/a–n/a. doi:10.1029/2010GL045805.

Vieira, S.R., Carvalho, J.R.P. de, Ceddia, M.B., González, A.P., (2009). Detrending non stationary data for geostatistical applications. Bragantia 69: 01–08.

Wessel, P., Smith, W.H., (1998). New, improved version of Generic Mapping Tools released. Eos, Transactions American Geophysical Union, 79: 579–579.

CHAPTER 3

Reference frame access under the effects of great earthquakes: a least squares collocation approach for non-secular post-seismic evolution

Published in the Journal of Geodesy

Introduction

In traditional geodesy and surveying, reference frames (RF) were realized using a combination of astronomical, trilateration and triangulation observations that resulted in apparent fixed benchmark coordinates due to the low precision of such observations. With the advent of high precision GPS surveying we can no longer assume benchmark coordinates are fixed, since GPS can easily observe secular plate motions. The precision available from GPS/GNSS surveying therefore requires taking the observed motions into account by additionally stating both the epoch of the RF definition and the secular velocity of each benchmark. With the continuing improvements of GNSS technology, additional secular and non-secular crustal deformation signals such as plate boundary deformation, co-seismic static offsets, years long post-seismic deformations, and glacial isostatic adjustment have also become observable and must be taken into account to produce very stable RFs (Bevis and Brown 2014). Co-seismic offsets, estimated using GPS measurements, range from ~10 m in the rupture zone to several millimeters at distances >1000 km for subduction megathrust (Mw9+) earthquakes (Pollitz et al. 2011). Such earthquakes also produce post-seismic deformations that can occur for decades before returning to the secular inter-seismic deformation component of the earthquake cycle (Khazaradze et al. 2002; Zweck et al. 2002; Hu et al. 2004; Wang et al. 2007). The description of the time evolution of a continuous GPS (CGPS) station’s position, therefore, must take all these effects into account and can be described using an extended trajectory model (ETM) (Bevis and Brown 2014).

Estimation of a passive benchmark's position at a given epoch, which allows accessing the RF, can be made through interpolation, such as least squares collocation (LSC), if the number and density of observations suffice and the velocity or deformation field is sufficiently smooth (Gómez et al. 2015), or using geodynamics based results such as finite element (FEM) or analytic models (Tong et al. 2010; Lorito et al. 2011; Pollitz et al. 2011; Moreno et al. 2012; Snay et al. 2013; Lin et al. 2013). To estimate passive benchmark positions at a given epoch in South America in the Geocentric Reference System for the Americas (*Sistema de Referencia Geocéntrico para las Américas*, SIRGAS) RF (Seemüller et al. 2009) one can use the existing Velocity Model for SIRGAS (VEMOS2009) (Drewes and Heidbach 2012) that only considers plate motion and boundary deformation, both of which are secular.

The 2010 (Mw 8.8) Maule, Chile, earthquake, in the region spanning 28°S and 40°S extending from the Pacific to the Atlantic oceans, produced large, static, co-seismic displacements and an ongoing deformation associated with non-secular after-slip and visco-elastic relaxation that will last for decades. The coordinates of the stations in the RF, therefore, suffered both a large jump on the day of the earthquake, and a large, non-secular change in their trajectories. Due to these effects, the secular VEMOS2009 model no longer provides useful estimates of passive benchmark trajectories, in the affected area, since it does not provide estimates of the co- and post-seismic deformation components.

Many geodetic and land surveying applications require passive benchmarks and CGPS station coordinates to be given in a specific RF and at a specific epoch, which in general is the epoch of the RF definition. In Argentina, the official RF is called *Posiciones Geodésicas Argentinas* 2007 (POSGAR07), which is a densification of the International Terrestrial Reference Frame 2005 (ITRF05) (Altamimi et al. 2007). Its materialization was performed using measurements between 2006 and 2007 and defined at the average measurement epoch 2006.632. When a new CGPS station or geodetic benchmark is installed at a location without pre-Maule earthquake measurements, determining the POSGAR07 coordinate (i.e. accessing the RF) is difficult, as there is no practical procedure to "remove" the co-seismic discontinuity and post-seismic deformation to obtain its epoch 2006.632 coordinate. Furthermore, before the Maule earthquake, positions in POSGAR07 of passive benchmarks were known with an accuracy of ~1 to 10 cm. After the earthquake, the co-seismic displacements changed the accuracy of passive benchmark coordinates within the region affected by the earthquake. When using the POSGAR07 coordinates (those defined at epoch 2006.632), the accuracy of the passive network is now estimated to be ~10 – 70 cm, depending on the size of the co-seismic displacement at the position of the benchmark. This level of accuracy is not sufficient for many applications such as civil engineering and land surveying. Moreover, the coordinates continue to change with undetermined trajectories, preventing access to the RF using observations obtained after the earthquake. This is especially problematic during regional geodetic network adjustments in the region with large horizontal displacements and strong post-seismic motions.

To obtain POSGAR07 coordinates starting from post-earthquake coordinates, or vice versa, it is therefore necessary to establish a model to access the RF. This model has to take into account all the effects produced by the Maule earthquake and provide continuous temporal and spatial estimates of benchmark trajectories. We will refer to this as a trajectory prediction model (TPM). The creation of a TPM to access the RF has broader implications than just the practical use of a terrestrial RF such as POSGAR07. During the past 20 years, the Central Andes GPS Project (CAP) has been collecting campaign GPS data throughout the central and southern Andes. For "historic" stations, i.e. GPS sites with at least two measurements before and one after the Maule earthquake, a model of the post-seismic deformation TPM provides additional information regarding the co-seismic displacements. We will show that the post-seismic deformation TPM tracks the positions/coordinates of campaign GPS data very well. The application of this model provides additional control on estimates of co-seismic displacement that can be used to constrain models of the earthquake and the tectonic evolution of the Andes.

Snay et al. (2013) also developed models to predict station coordinates under the effects of great earthquakes. Although our approach is similar, there are several significant differences in our proposed methodology. First, they used a dynamic model for the secular inter-seismic velocities, while we used the LSC approach of Drewes and Heidbach (2012). Another difference is the type of dynamic model used to estimate the co-seismic displacements. We used a spherical FEM for the Maule earthquake, while Snay et al. (2013) used analytic dislocation theory in a half-space (Okada 1985). Finally, for post-seismic deformation, we propose a kinematic approach similar to that of Snay et al. (2013), but using a spatial taper function and LSC to model the first-order behavior of the observed post-seismic transients.

To obtain the TPM, we used CGPS data from the Argentine Continuous Satellite Monitoring Network (*Red Argentina de Monitoreo Satelital Continuo,* RAMSAC), CAP, the International GNSS Service (IGS), and several other scientific CGPS networks (see Supplementary Material). We used CGPS time series from the Argentine Scientific Processing Center **(***Centro de Procesamiento Científico Argentino*, CPC-Ar) at the Argentine National Geographic Institute (*Instituto Geográfico Nacional,* IGN) for stations they process (all stations in Argentina, plus a handful of nearby IGS stations) and the Nevada Geodetic Laboratory daily solutions, published on-line, for other stations, mostly in Chile. We applied the ETM method of Bevis and Brown (2014) to the time series to obtain estimates of both the non-secular, post-seismic transients generated by the earthquake and the secular plate motion and inter-seismic velocities. Using CGPS stations installed after the earthquake and post-earthquake CAP campaign data, we will show that the standard deviations (95% confidence level) for the north and east components of our post-seismic TPM are 3.8 and 5.5 mm, respectively. Finally, we use POSGAR's pre- and post-seismic measurements with a FEM of the co-seismic displacements to show that the TPM allows accessing POSGAR07, using post-seismic coordinates, within the original accuracies at ~91% of the test benchmarks. Although this work presents a model that has been applied to CGPS and campaign data within Argentina, it can be used in any region with post-seismic deformation and a limited number of observations.

Underlying secular inter-seismic velocities of the CAP, RAMSAC and IGS networks

Bevis and Brown (2014) present an ETM and demonstrate that its application to RF materialization can considerably reduce systematic errors in RF realization. In addition to the secular velocities used in constant velocity models (CVM), their ETM contains static offsets to model equipment changes and co-seismic jumps, sinusoidal components to model observed periodic displacements, and logarithmic transients to model non-secular after slip and visco-elastic relaxation. The linear mathematical expression for the ETM is:

$$\begin{aligned}\mathbf{x}(t) = &\sum_{i=1}^{n_p+1} \mathbf{p}_i (t-t_R)^{i-1} + \sum_{j=1}^{n_j} \mathbf{b}_j H(t-t_j) + \\ &+\sum_{k=1}^{n_F} [\mathbf{s}_k \sin(\omega_k t) + \mathbf{c}_k \cos(\omega_k t)] \\ &+\sum_{i=1}^{n_T} \mathbf{a}_i \log[1+\Delta t_i / T_i]\end{aligned} \tag{1}$$

where *t* is time, n_P is the number of polynomial terms, $\mathbf{p}_i$ is the amplitude of the i^{th} polynomial term and t_R is the reference epoch (adopted by convention). Using one polynomial term, $n_p = 1$ provides a secular, or constant, velocity that describes plate motion and effects such as inter-seismic deformation. “Jumps”, used to model equipment changes, earthquake co-seismic jumps, etc., are modeled using the Heavside function, *H*, where n_j is the total number of jumps, with amplitude $\mathbf{b}_j$ at time t_j for the j^{th} jump. For the periodic component, n_F is the number of frequencies used, with the k^{th} frequency being ω_k. Phase is determined by using both sine and cosine terms, with amplitudes $\mathbf{s}_k, \mathbf{c}_k$. The final component models logarithmic transients. As with the jumps, a number of transients can be included, n_T. Each transient has its own amplitude, $\mathbf{a}_i$ and a relaxation time T_i. For each *i* seismic event, $\Delta t_i = 0$ for $t < t_{EQ}$, where t_{EQ} is the reference epoch of the earthquake, and $\Delta t_i = t - t_{EQ}$ for $t >= t_{EQ}$ since the post-seismic transient exists only after t_{EQ}. Bevis and Brown (2014) provide an exhaustive description of the evolution of the trajectory models and how to select and apply the various components of the model.

To describe the CGPS trajectories we used $n_P = 1$, since none of the time series display observable pre-seismic non-linearity, i.e. they are typical secular CGPS time series associated with plate motions and the regional plate boundary tectonics. Two frequencies, annual and semi-annual, are typically sufficient to model the observed periodic behavior and we used $n_F = 2$ for these components. As would be expected from a least squares adjustment, the inclusion of additional parameters in the ETM (i.e. the periodic terms) reduces the misfit. This variance reduction in misfit, however, should be statistically significant in order to justify the inclusion of additional model parameters. To determine if the misfit reduction was significant, we applied an

F-test to a set of ETMs from 37 CGPS stations with data from before and after the Maule earthquake, and found that only 7 stations (BCAR, CHLT, JUNT, LHCL, LPGS, RWSN and SRLP) did not show a statistically significant improvement of the residuals' variance on any of their three components (although the misfits were always reduced). Analyzing the north, east and up components independently, we found statistically significant improvements in 24 stations for the north, 15 stations for the east and 18 stations for the up components.

The inclusion of periodic terms in most cases also helps to better constrain the adjustment of the ETM parameters. We compared the least squares estimated uncertainty of the velocity, co-seismic jump and logarithmic transient for the ETM both with and without periodic terms. From the estimated uncertainties, Figure 1a shows the north, east and up histograms of the percentage change in the uncertainty of the velocity estimate. In these plots, a positive percentage change represents a precision increase (uncertainty reduction) with respect to the precision of the ETM without the periodic terms. For three stations examined, we observe an increase in precision of up to 40-45 percent, although most of the increases are less than 25 percent. There are only two cases where we observe a precision decrease in the north velocity estimate (stations RWSN and SJAV), two stations in the east velocity estimate (COYQ and SJAV) and two stations in the up velocity estimates (SJAV and VAL3), although we only note one considerable reduction in the east component for station SJAV of ~16 percent. We also note that the mean uncertainty (95% confidence level) for the three velocity components varies between 0.4 mm/yr and 1.4 mm/yr, which make these changes (positive or negative) very small. Histograms for the other two parameters (co-seismic jump and logarithmic transient), show very similar distributions and are therefore not shown.

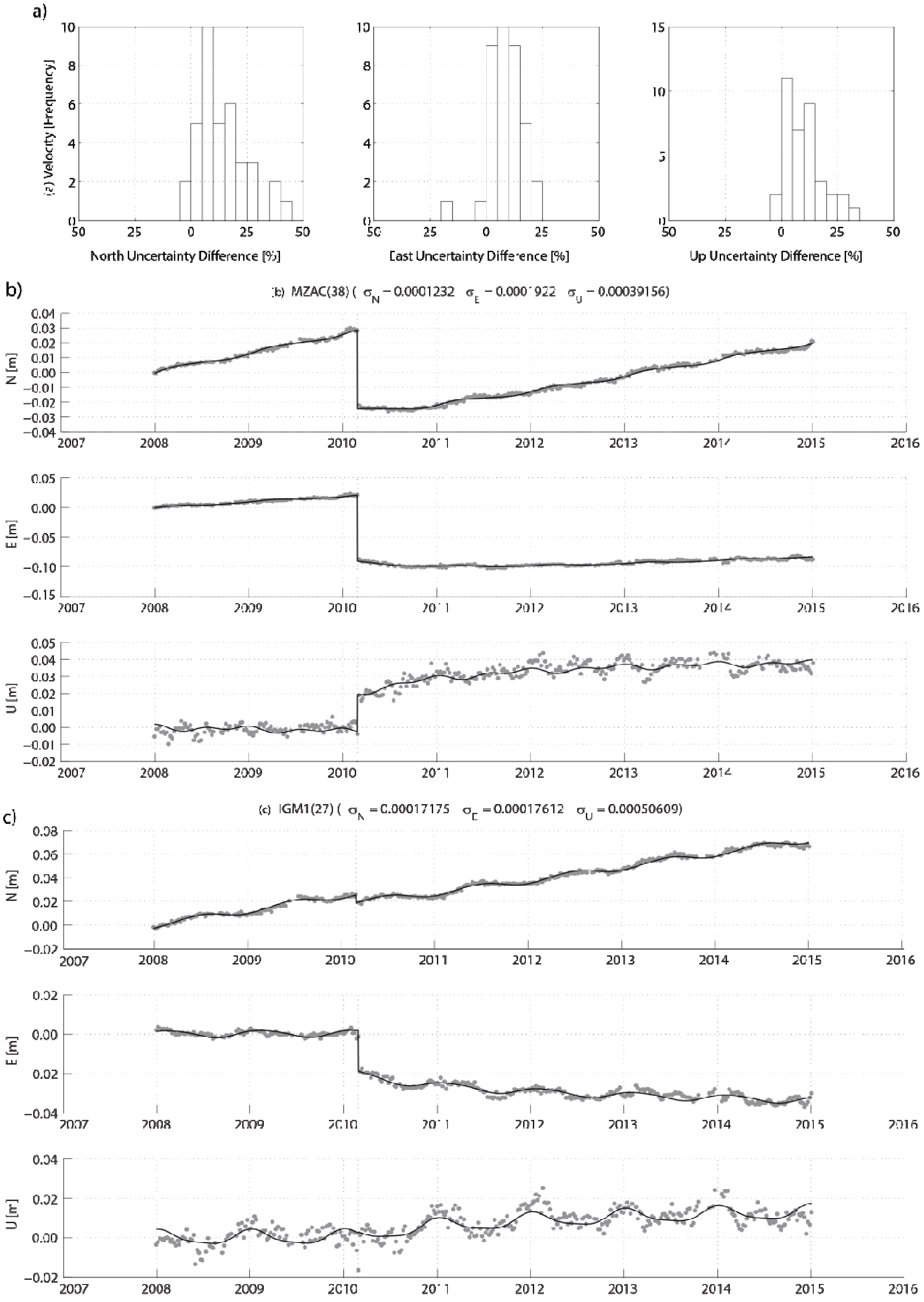

Figure 1. Histograms and time series. (a) North, east and up histograms of the least squares estimated uncertainty change (in percentage) for the velocity component of the ETMs with and without periodic terms. A positive value represents a decrease in uncertainty (precision increase). (b) ETM of RAMSAC station MZAC. Co-, post- and inter-seismic components can be observed. (b) ETM of RAMSAC station IGM1. Periodic terms are more visible (compared to MZAC) since the scales of the co-seismic jumps are smaller than those from MZAC.

To model the logarithmic post-seismic transients from the Maule earthquake, we applied a value of $T_i = 0.5$ years for the relaxation time of all the CGPS time series. This is different from the value $T_i = 1$ year proposed by Bevis and Brown (2014). In general, the logarithmic transient adjustment is relatively insensitive to the exact value of *T*, and we found that using $T_i = 0.5$ allowed use of a single relaxation time for the whole network while providing a good fit for both the near and far-field post-seismic time series.

One of the features of the ETM is that the least squares adjustment is done in a single step, without breaking the model into pre- and post-seismic adjustments. If a sufficient number of pre-seismic observations exist, estimation of the secular component is dominated by the pre-seismic part of the time series. To obtain a stable secular velocity, we only used time series with more than ~two years of pre-earthquake data. This provides a robust estimate of the CGPS stations' underlying inter-seismic velocities, which are assumed to remain constant throughout the earthquake cycle. Figure 1b and c shows two examples of the ETM adjustment for RAMSAC stations MZAC, located in the near-field of the Maule earthquake (Mendoza, Argentina), and IGM1, located in the far-field (Buenos Aires, Argentina), both of which have ~two years of pre-earthquake data. These plots show the three components (north, east and up) although the TPM developed does not include the vertical component.

Drewes and Heidbach (2012) noted that vertical signals are much more complex and are very difficult to model using either interpolative (e.g. LSC) or numerical models, and therefore, we also only model the horizontal components, although Snay et al. (2013) estimated both horizontal and vertical components using numerical modeling and obtained very good results. The selection of LSC to produce our TPM was made based on the fact that the LSC approach is much simpler to implement than numerical models, and provides equally good results (Drewes and Heidbach 2012), nevertheless, this selection comes at the expense of not modeling the vertical component.

To estimate the inter-seismic velocities, we developed an LSC interpolation to estimate the velocity field on a 1º grid. To apply LSC we first remove plate motions using the ITRF compatible, no-net-rotation (NNR), Actual Plate Kinematic Model (Drewes 2009). The problem of estimating an empirical covariance function for inter-seismic velocities has been described by Drewes and Heidbach (2012). They show that correlation lengths for the north and east velocity components are quite different in regions suffering crustal deformation (e.g. the Andes cordillera) than in stable South America (e.g. the east coast). The empirical covariance functions are therefore estimated using a point by point calculation, as in Drewes and Heidbach (2012). We proceeded as follows. For each point for which velocity is to be estimated, 1) we perform a Delaunay triangulation over the set of vertices consisting of the CGPS stations plus the point of interest; 2) we then select only those triangles that include the point of interest; 3) using only the CGPS stations from step 2 with pre-earthquake data, we estimate the empirical covariance function; 4) we apply LSC at the point of interest using this empirical covariance function and the detrended CGPS inter-seismic velocities.

Figure 2a shows the velocity model, known as the “linear Argentine Velocity” model (*Velocidades Argentinas Lineales*, Vel-Ar-Lin), obtained using this procedure. We also compare Vel-Ar-Lin against VEMOS2009 (Figure 2b), which shows that their difference never exceeded 8 mm. The largest differences are in Patagonia (Río Negro, Chubut and Santa Cruz Provinces), where we used additional CPGS stations that were not available in the preparation of VEMOS2009. A few large differences can be observed near the edges of Vel-Ar-Lin (in Bolivia and west from Tierra del Fuego) but these areas are outside the intended limits of the model.

Note that in this version of Vel-Ar-Lin, we are not considering the deformation associated with the South America – Scotia plate boundary across the Magallanes-Fagnano transform fault in Tierra del Fuego. This improvement will be taken into account in future versions of Vel-Ar-Lin.

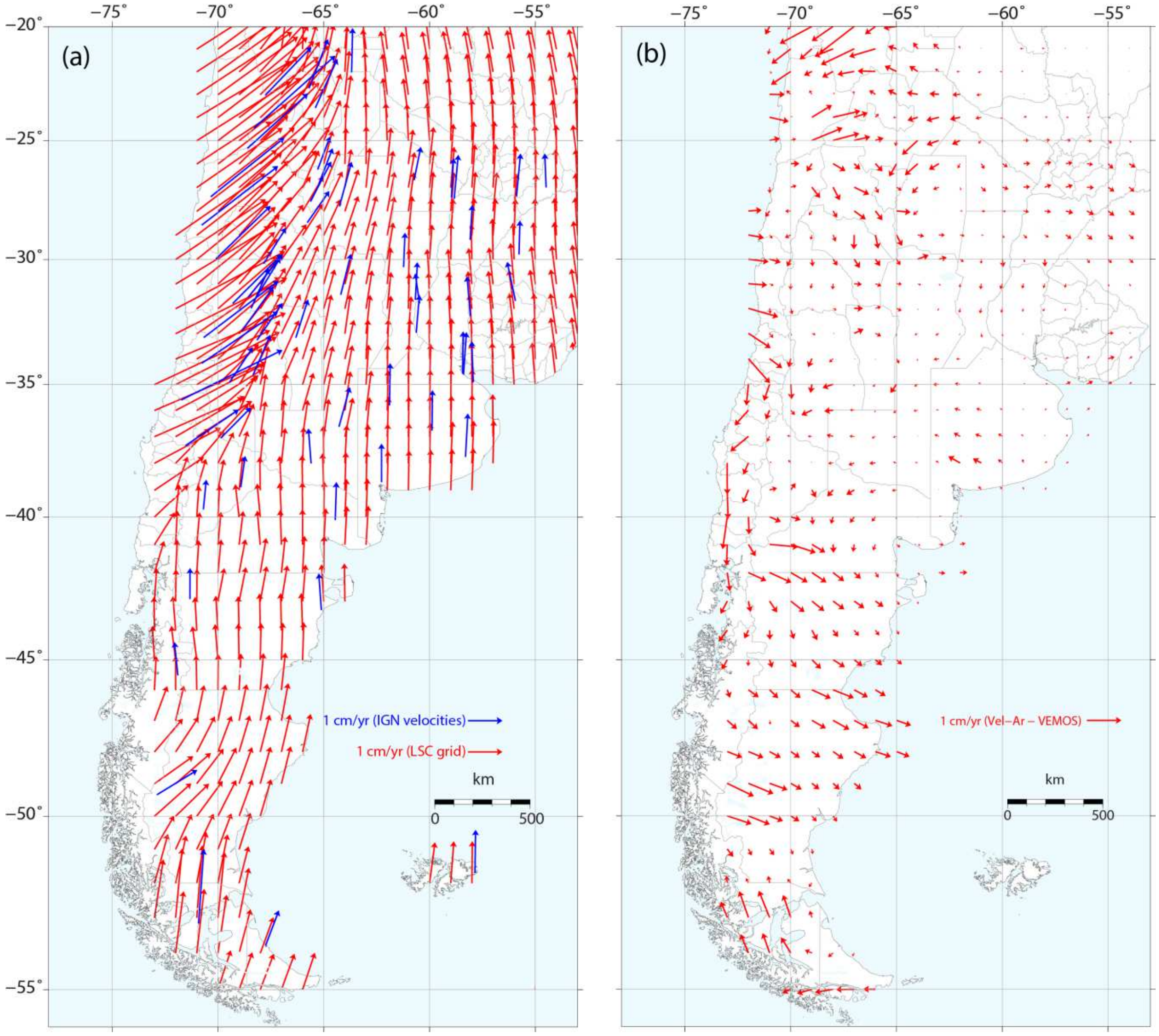

Figure 2. Difference between Vel-Ar-Lin and VEMOS2009. (a) Least squares collocation of the secular inter-seismic velocities of the RAMSAC, CAP and IGS networks in POSGAR07. Blue arrows show the CGPS stations used for the interpolation. Red arrows show the 1º grid in latitude and longitude of interpolated velocities. (b) Residual of the difference between Vel-Ar-Lin and VEMOS2009 velocity model. Due to the addition of new CGPS sites, the largest differences are located in Patagonia.

Least squares collocation of post-seismic deformation

To obtain an estimate of the amplitude of the post-seismic signal, we need to add the logarithmic transients to the secular, inter-seismic velocity field. The ETM of the CGPS time series provide point measurements of the transient amplitude components at the location of the CGPS stations. These point measurements will be interpolated using an LSC to obtain a spatially continuous logarithmic transient field.

Within a few weeks of the Maule earthquake, the CAP group installed several dozen CGPS stations in and around the epicentral area in Chile and Argentina, while also reoccupying existing campaign sites and installing new ones (in Argentina only) to densify sampling of the post-seismic deformation field. As previously discussed, the ETM assumes that the secular velocity associated with plate motion and plate boundary interaction deformation is constant throughout the earthquake cycle, even after the post-seismic deformation starts. Unfortunately, as the basis functions of the secular and logarithmic transient components of the ETM are not orthogonal, we cannot constrain the secular and logarithmic components of the ETM simultaneously. Therefore, we need a sufficiently long pre-earthquake time series to independently constrain the secular component.

To include the new, post-earthquake only, CGPS stations in the post-seismic deformation model, we removed their motion under the Vel-Ar-Lin model before adjusting for the post-seismic component of the ETM (see Supplementary Material). The transients estimated using this procedure are compatible with those estimated for CGPS stations with pre-earthquake data and can, therefore, be included into a single LSC interpolation for the logarithmic transient amplitudes. Adding this transient interpolation to Vel-Ar-Lin, we obtain one of the TPM components necessary to access POSGAR07 coordinates based on the measured post-seismic coordinates (less the component due to the co-seismic displacement that will be discussed later).

To apply LSC to a data set, it must meet the intrinsic hypothesis (Ligas and Kulczycki 2010; Vieira et al. 2010), which in its simplest and most often used form requires that the data do not exhibit a trend. There are few restrictions on the function used to remove the trend, although in practice, low order polynomials are oftentimes used. The quality of the trend removal can be tested with a semi-variogram, which displays a sill near the expectation value of the detrended data (Vieira et al. 2010). Following Vieira et al. (2010), we detrended the data using polynomials of increasing degree, until the semi-variogram displayed a stable sill. We found that a degree four polynomial adequately removed the post-seismic transient trend, but produced undesired edge effects near the model limits. Further examination of the post-seismic deformation field, however, showed that as we move away from the rupture zone, amplitudes of the transient fall to near zero with a decaying exponential shape. We therefore used spatial exponential tapers, one for the E-W and one for the N-S trends, respectively, that provide a first order approximation to the trend of the data, while also decaying to zero as we move away from the rupture zone. The detrending function is:

$$A = a \exp\left(-\frac{(x-x_0)^2 + (y-y_0)^2}{2\sigma} \right) \tag{2}$$

where x_0, y_0 is the origin of the taper, *a* is the maximum amplitude and σ is the decay distance. We found the best fitting parameters x_0, y_0, a and σ for the north and east components of the transients by performing a grid search over the space of residuals produced by (2).

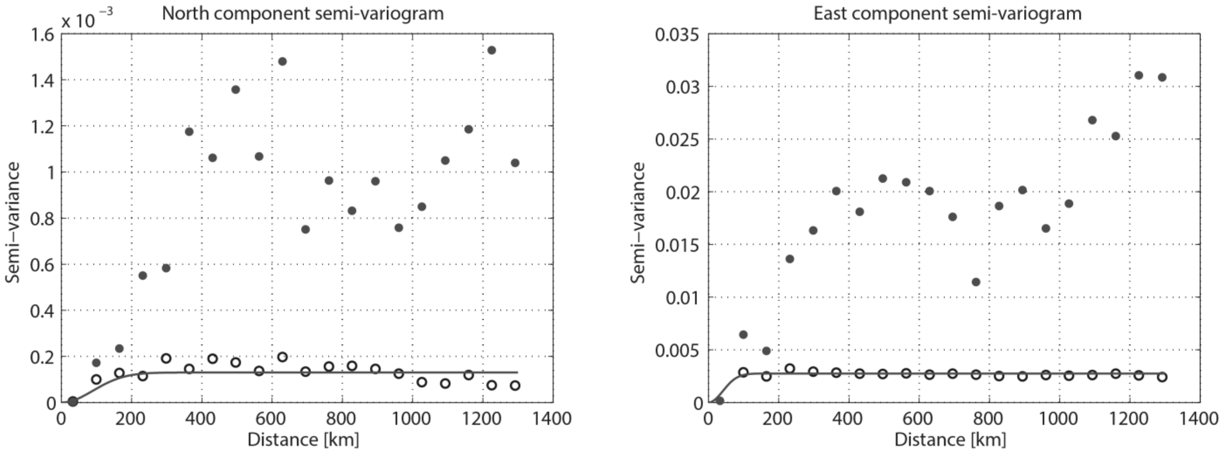

Figure 3. Semi-variogram plots of the north and east components of the post-seismic transient after applying an exponential taper detrending function. Empty circles show the detrended data, filled circles show the original data, and the solid line is the Gaussian semi-variance model.

From Figure 3, we note that it is possible to apply LSC to the detrended data, since the semi-variograms show a stable sill after removing the trend. The stability of the sill also shows that the data can be modeled as a stationary process, which means that we can use a single co-variance function for the entire domain. Therefore, we applied the LSC method to the logarithmic transients to produce a 0.25º grid. This spacing was selected so the transient data between grid nodes can be linearly interpolated, which simplifies using the model. The spacing was verified by comparing the transients obtained from the ETMs against the transients obtained by linearly interpolating the post-seismic deformation LSC model. A larger grid spacing (say, 1º) would produce interpolated transients that are not in agreement with the observed data, due to the non-linearity of the spatial change of the logarithmic transients.

Figure 4a and b shows the LSC interpolated logarithmic amplitudes (in meters), which we have called “Argentine Non-Linear Velocities” (*Velocidades Argentinas No Lineales*, Vel-Ar-NoLin), while Figure 4c and d shows two snapshots of the instantaneous velocity field (in cm/yr) two years and four years after the earthquake (epochs 2012.15 and 2014.15). To test Vel-

Ar-Lin and Vel-Ar-NoLin, we examined the residuals calculated by subtracting the LSC estimated positions from observed time series for a set CAP campaign and CGPS sites that were not included in the development of the LSC models (sites indicated by red circles in Figure 4a and b). We fit normal distributions to the residual histograms (Figure 5a and b) were we found standard deviations (95% confidence level) of 3.8 and 5.5 mm in the north and east components, respectively. A slight tendency towards negative values can also be observed, which reveals the presence of a small systematic bias that is probably due to the misfit of the logarithmic transient to the data, observed during the first month after the earthquake. Bevis and Brown (2014) showed this misfit can be reduced by adjusting the value of the relaxation time for each time series. As discussed earlier, we did not apply this procedure since we used a common relaxation time for the entire network. For the precision and purposes of the model developed here, however, these misfits can be ignored.

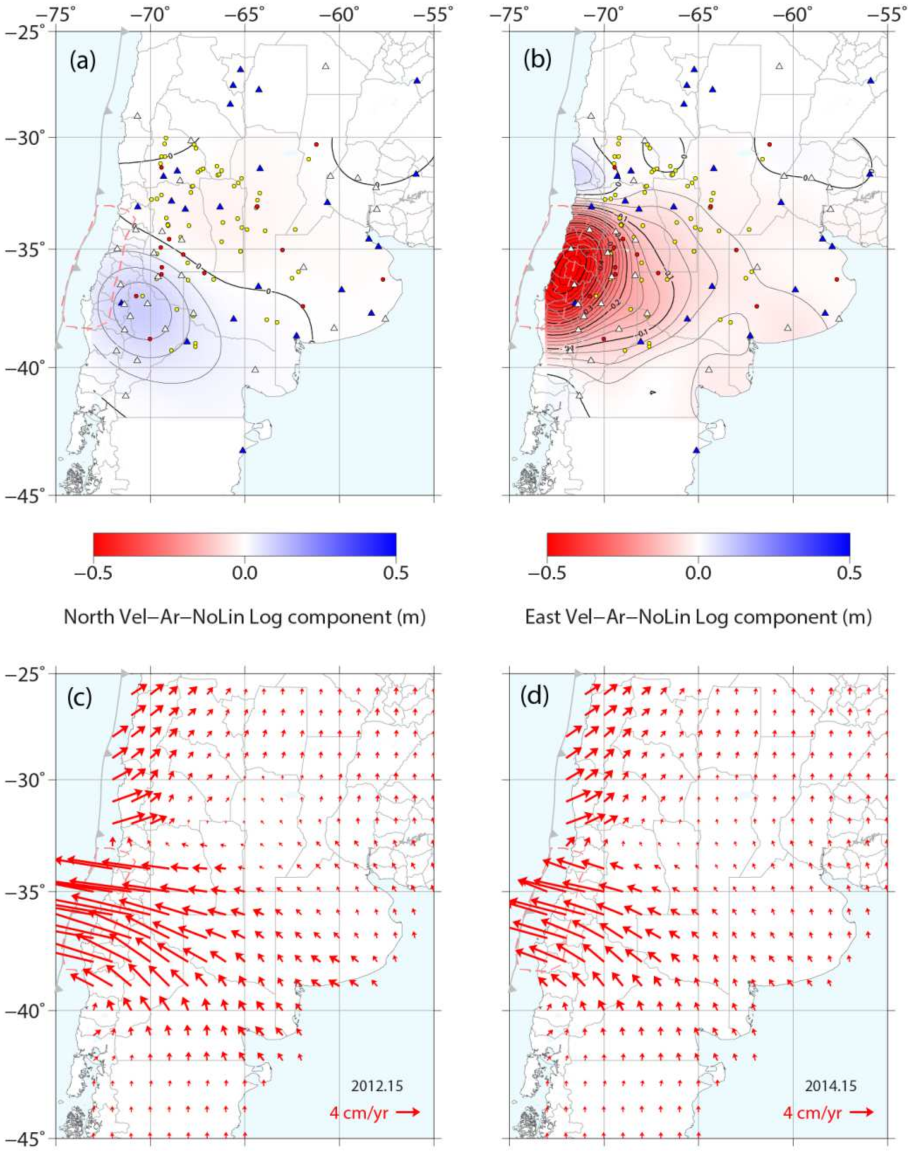

Figure 4. Least squares collocation model of the logarithmic transients for (a) north and (b) east components. Blue triangles show the CGPS stations that have ~2 or more years of pre-earthquake data. White triangles show CGPS that don't meet the condition to be included in the Vel-Ar-Lin estimation. Red circles show the test stations, which have multiple measurements, used to verify the quality of the Vel-Ar-Lin and Vel-Ar-NoLin models. Yellow circles are POSGAR benchmarks with only one measurement before and one after the earthquake. Contours of logarithmic transients every 0.025 m. Red dashed line shows the 2010 Maule earthquake rupture zone as defined by aftershocks. (c) Snapshot of the instantaneous velocity field at epoch ~2012.15. (d) Same as d at epoch ~2014.15.

(a) Vel–Ar north differences; μ: 5.18e–10; 2 σ: 0.0038

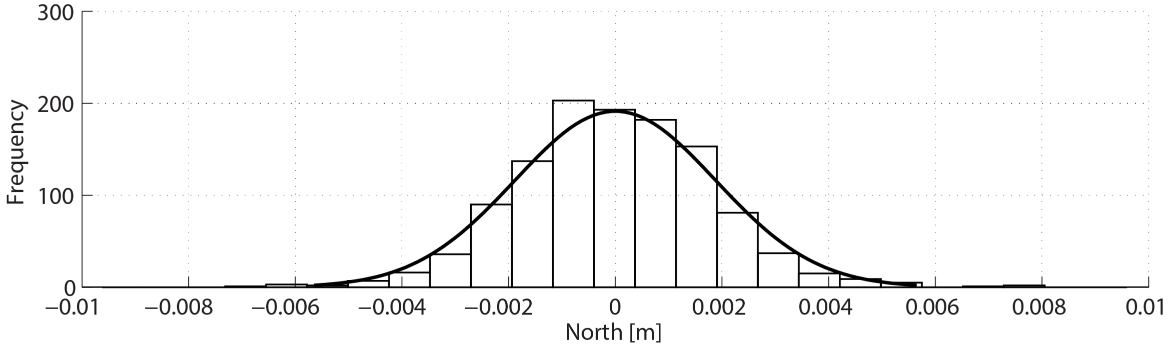

(b) Vel–Ar east differences; μ: –1.06e–09; 2 σ: 0.0055

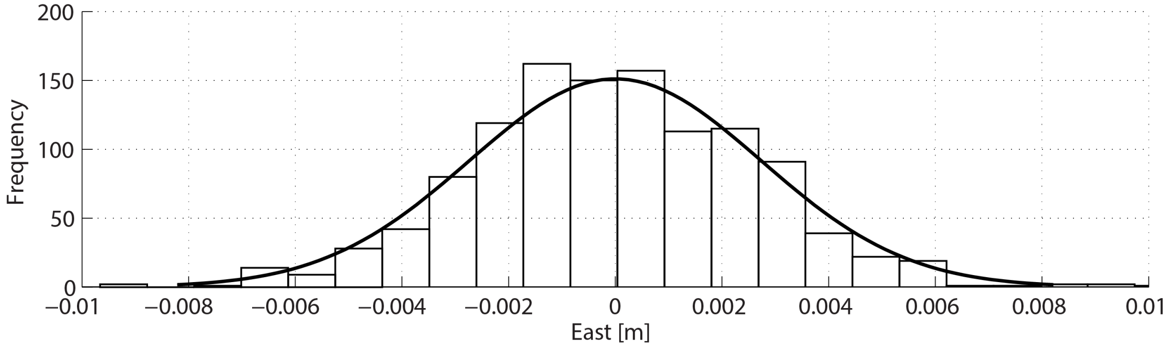

Figure 5. Histogram of the difference between the modeled and observed trajectories and their fits to normal distributions for (a) north and (b) east components, for CAP and RAMSAC CGPS sites and CAP campaign sites with multiple measurements used in the Vel-Ar-Lin and Vel-Ar-NoLin test.

Accessing POSGAR07 using post-seismic coordinates: co-seismic displacements

To successfully access POSGAR07 using post-seismic coordinates, a co-seismic displacement model must also be included. This model, combined with the secular and non-secular LSC models (Vel-Ar-Lin and Vel-Ar-NoLin) results in the final, complete TPM “Argentine Velocities” (*Velocidades Argentinas*, Vel-Ar) connecting the post-seismic coordinates to the pre-seismic coordinates.

Immediately after the Maule earthquake (between epochs 2010.2 and 2010.9) teams from CAP and IGN performed measurements on ~60 existing CAP and POSGAR benchmarks (see Supplementary Material) to quantify the co-seismic displacement and begin measurements of the post-seismic deformation. Based on results of the immediate post-earthquake campaign, IGN produced a set of recommendations for land surveyors operating in the region suffering deformation due to the Maule earthquake. Although most land surveyors do not use scientific GPS processing software to determine coordinates, the crustal deformation effects of the Maule earthquake are large enough, especially in the Provinces of Mendoza and Neuquén, that even with commercial GPS processing software application of Vel-Ar TPM is necessary to estimate coordinates that are within the working tolerances of the original network.

As with the plate velocity, inter-seismic and post-seismic signals, there are two general methods to estimate the co-seismic displacements at a non-CGPS benchmark: 1) kinematic model method: interpolate from nearby sites with CGPS measurements or 2) dynamic model method: use a physical/geodynamic model for the crustal deformation effects generated by the earthquake. LSC, an example of interpolation in a kinematic model, has previously been applied, highly successfully, to model secular plate motions and inter-seismic deformations, and we have extended it here to also model post-seismic transients. Geodynamic models can be analytic solutions or numerical models such as FEM. In the case of using LSC to interpolate the co-seismic static offset for the Maule earthquake, Gómez et al. (2015) showed that due to the small number of CGPS stations and the rapid variation of the co-seismic displacement field, especially in the near-field, an LSC of the co-seismic offset dataset does not produce an adequate interpolation. Although it has been suggested to use the LSC post-seismic and inter-seismic models to estimate the co-seismic displacements at sites with a few observations before and after the earthquake (Drewes and Sánchez 2013), this method only provides indirect, unverifiable estimates, with unknown precision, of the co-seismic displacement field. We have therefore estimated the co-seismic displacements with a FEM using Pylith (Aagaard et al. 2013). FEM is a numerical technique for finding approximate solutions to differential equations. Pylith, one of many programs available to compute finite element solutions, is a numerical approach to solve dynamic and quasistatic elasticity problems. We will later show that the FEM model satisfies our target precision.

FEM is one of the many classes of solutions to geodynamic models. For example, Snay et al. (2013) applied dislocation theory to a flat earth model to quantify the co-seismic displacements of 29 major earthquakes that produced co- and post-seismic deformation in and around the United States. As the region affected by the Maule earthquake, studied here, extends from Chile to eastern Argentina, a flat earth or half-space model is inappropriate and we therefore used a layered spherical FEM with Preliminary Earth Model (Dziewonski and Anderson 1981) layer thicknesses and elastic properties. Although we used a FEM, a spherical analytical solution to the problem is also available from Pollitz (1996) that has been applied to the Maule earthquake (Pollitz et al. 2011).

The construction of a FEM starts by defining a mesh of nodes to which the finite element method will be applied. This mesh or grid of nodes is, in general, not a uniformly sampled domain, since the mesh is a discretization of the modeled geometry and, therefore, the spacing and shape of the figures formed by the FEM nodes changes to adapt to the model geometry. The FEM used for Vel-Ar is an ongoing project of the CAP group and only includes the first order geometrical characteristics that have the greatest impact on estimating co-seismic deformation. It uses triangular elements and has an approximate spacing of 30 km between nodes, although in the near-field (where the co-seismic displacements are less smooth) the spacing averages ~ 20 km.

After the model geometry is defined, which includes both earth structure and properties and an a priori fault geometry, the GPS data is used to invert for a finite fault slip model. The input data for the finite fault slip model least squares inversion are the co-seismic jumps obtained from the ETMs. The design matrix used to solve the least squares problem is formed by the so-called Green's functions or impulse responses of the CGPS sites obtained from the FEM, and a discrete smoothing operator (Maerten 2005). The inversion yields the approximate slip distribution on the predefined fault surface that we defined by the USGS South American subduction zone slab model (Hayes et al. 2012). Once the finite fault slip model is obtained, we run a forward calculation to estimate the co-seismic displacements at each node of our FEM. Finally, we extract the co-seismic displacement information from the nodes located on the surface of the FEM.

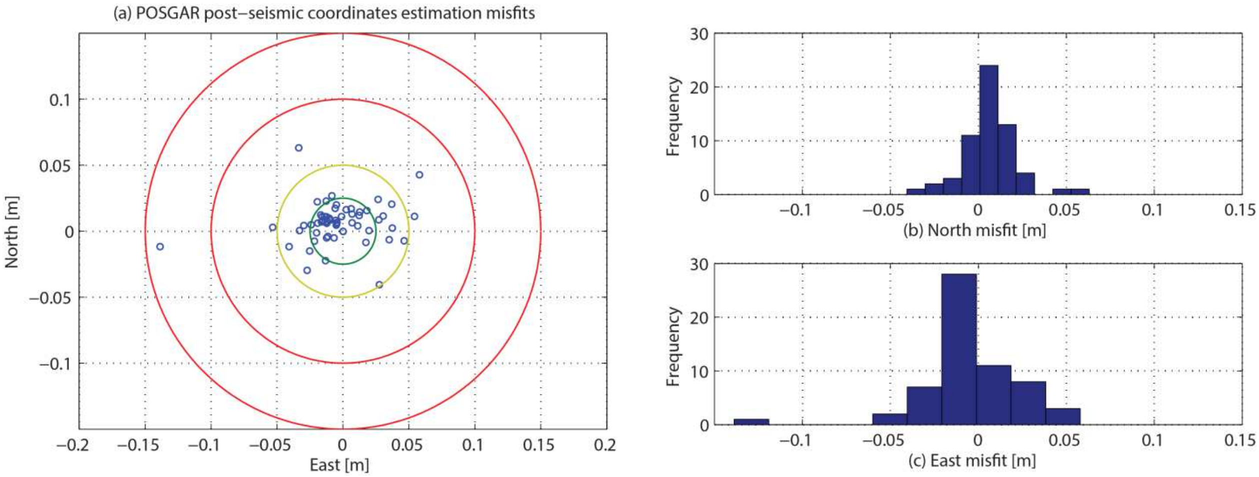

Figure 6. Full Vel-Ar model test. (a) Misfit between the post-seismic measurements of POSGAR benchmarks. Green, yellow and red circles represent a misfit distance of 2.5 cm, 5 cm, 10 and 15 cm. Test sites are shown in Figure 4a and b by yellow filled circles. (b) Histogram of north component differences shown in a. (c) Histogram of east component differences shown in a.

We tested the ability of the TPM to access POSGAR07 using the POSGAR sites that were not used in the calculation of Vel-Ar (Figure 4a and b, yellow filled circles). Using the pre-seismic coordinates (obtained between epochs 2006 and 2007.5), we applied Vel-Ar-Lin and Vel-Ar-NoLin to estimate the inter-seismic and post-seismic displacements at the POSGAR benchmark sites and the jumps obtained from the FEM co-seismic model to estimate the total displacement and added this to the RF definition coordinate to obtain the estimate of the post-seismic coordinate. Finally, we compared the predicted post-seismic coordinate to the post-seismic measurement. The misfits in the north and east components are shown in Figure 6a, where we note that 38 of 60 sites (~63%) fall inside the 2.5 cm limit, 17 (~28%) fall between 2.5 and 5 cm, and 5 (~8%) fall outside the 5 cm limit. Only one measurement falls outside the 10 cm limit (with a misfit of 13.8 cm), although we do not discard the possibility of a blunder in the measurement or processing of that site. Figure 6b and c shows the histograms of the misfits shown in Figure 6a, where we note a systematic bias in both the north and east components, respectively. These biases are a result of the misfit between the FEM and the observed co-seismic displacements.

Conclusion

We have shown how to use the post-seismic logarithmic transients, estimated using an ETM, to produce a LSC model of the post-seismic deformation field of the 2010, (Mw8.8), Maule earthquake. As our focus is the region affected by the Maule earthquake, we produced our own, updated, inter-seismic velocity model (Vel-Ar-Lin), using more CGPS data within Argentina than was available during the creation of VEMOS2009. This methodology we developed can be used to update VEMOS2009 to include the effects of the Maule earthquake by incorporating a logarithmic transient LSC model and a co-seismic displacement model. Updating

VEMOS2009 in this manner would allow it to predict the trajectories of the passive benchmarks in the SIRGAS RF using a non-linear-model (*modelos no lineales*, MoNoLin), without having to break the time series into multiple, sequential, linear segments, with periodic updates, as proposed by Drewes and Sánchez (2014).

Our results show that ~63% of the test sites (i.e., those not used to produce Vel-Ar, Figure 4a and b) have misfits less than 2.5 cm and ~28% have misfits between 2.5 cm and 5 cm (Figure 6a). The application of Vel-Ar TPM to provincial geodetic benchmark networks will provide access to POSGAR07 with an accuracy that is approximately the same as that of the POSGAR network before the earthquake occurred. Examining the estimated precision of the post-seismic deformation estimates (Figure 5a and b), we conclude the majority of the misfit in the POSGAR benchmark test is due to the co-seismic model, not the post-seismic LSC model (Vel-Ar-NoLin). Nevertheless, the FEM developed by Gómez et al. (2015) produces a much better fit than an LSC of the co-seismic displacement field and we therefore selected the FEM to estimate the co-seismic displacement field. A finite element model is currently under development by the CAP geodynamics group for both the co-seismic and post-seismic components. IGN is currently developing a legal implementation of the Vel-Ar TPM that will be available from their website.

While the method presented here successfully provides trajectory estimates of passive and CGPS sites after the Maule earthquake, it requires at least two years of observations to correctly constrain the post-seismic deformation (Bevis and Brown 2014). This kinematic approach is therefore reasonable to produce a TPM for an earthquake that occurred five years ago. In the case of future great earthquakes, dynamic models, as in Hu et al. (2004), could provide immediate estimation of the deformation field without waiting for months to years to measure and fit the post-seismic effects. Such dynamic models should be considered for immediate post-earthquake surveying activity and future TPM developments.

Acknowledgements

We thank Hernán Guagni, Agustín Raffo and the Department of Geodesy of the IGN for providing the GPS processing and additional support. We thank Benjamin Brooks and James Foster for providing additional GPS data used in this work and Wolfgang Schwanghart for providing his semi-variogram code through the Matlab® File Exchange. The authors would also like to thank three anonymous reviewers for their insightful comments and suggestions that have contributed to improve this paper. This work was supported by the NSF Collaborative Research: Great Earthquakes, Megathrust Phenomenology and Continental Dynamics in the Southern Andes, award number EAR-1118241, and the Center for Earthquake Research and Information, University of Memphis.

Data sources

Pylith web page: http://geodynamics.org/cig/software/pylith/

Maps were made using the Generic Mapping Tools version 5.1.1 (Wessel and Smith 1998)

Additional publicly available time series of CGPS stations located in Chile (and that are not part of CPC-Ar) were obtained from the Nevada Geodetic Laboratory: http://geodesy.unr.edu/

References

Aagaard BT, Knepley MG, Williams CA (2013) A domain decomposition approach to implementing fault slip in finite-element models of quasi-static and dynamic crustal deformation. J Geophys Res Solid Earth 118:3059–3079. doi: 10.1002/jgrb.50217

Altamimi Z, Collilieux X, Legrand J, et al (2007) ITRF2005: A new release of the International Terrestrial Reference Frame based on time series of station positions and Earth Orientation Parameters. J Geophys Res Solid Earth 112:B09401. doi: 10.1029/2007JB004949

Bevis M, Brown A (2014) Trajectory models and reference frames for crustal motion geodesy. J Geod 88:283–311. doi: 10.1007/s00190-013-0685-5

Drewes H (2009) The actual plate kinematic and crustal deformation model APKIM2005 as basis for a non-rotating ITRF. In: Geodetic Reference Frames. Springer Berlin Heidelberg, pp 95–99

Drewes H, Heidbach O (2012) The 2009 Horizontal Velocity Field for South America and the Caribbean. In: Kenyon S, Pacino MC, Marti U (eds) Geodesy for Planet Earth. Springer Berlin Heidelberg, Berlin, Heidelberg, pp 657–664

Drewes H, Sánchez L (2013) Modelado de deformaciones sísmicas en el mantenimiento de marcos geodésicos de referencia. http://www.sirgas.org/fileadmin/docs/Boletines/Bol18/36_Drewes_Sanchez_2013_Modelado_deformaciones_sismicas.pdf. Accessed 4 Jan 2014

Drewes H, Sánchez L (2014) Actualización del modelo de velocidades SIRGAS. http://www.sirgas.org/fileadmin/docs/Boletines/Bol19/60_Drewes_et_al_2014_ActualizacionVEMOS.pdf. Accessed 2 May 2015

Dziewonski AM, Anderson DL (1981) Preliminary reference Earth model. Phys Earth Planet Inter 25:297–356.

Gómez D, Smalley R, Langston C, et al (2015) Co-seismic deformation of the 2010 Maule, Chile earthquake: Validating a least squares collocation interpolation. GeoActa 40:(In press).

Hayes GP, Wald DJ, Johnson RL (2012) Slab1. 0: A three-dimensional model of global subduction zone geometries. J Geophys Res Solid Earth 1978–2012. doi: 10.1029/2011JB008524

Hu Y, Wang K, He J, et al (2004) Three-dimensional viscoelastic finite element model for postseismic deformation of the great 1960 Chile earthquake. J Geophys Res Solid Earth 109:B12403. doi: 10.1029/2004JB003163

Khazaradze G, Wang K, Klotz J, et al (2002) Prolonged post-seismic deformation of the 1960 great Chile earthquake and implications for mantle rheology. Geophys Res Lett 29:7–1.

Ligas M, Kulczycki M (2010) Simple spatial prediction-least squares prediction, simple kriging, and conditional expectation of normal vector. Geod Cartogr 59:69–81.

Lin YN, Sladen A, Ortega-Culaciati F, et al (2013) Coseismic and postseismic slip associated with the 2010 Maule Earthquake, Chile: Characterizing the Arauco Peninsula barrier effect: CHARACTERIZING ARAUCO BARRIER EFFECT. J Geophys Res Solid Earth 118:3142–3159. doi: 10.1002/jgrb.50207

Lorito S, Romano F, Atzori S, et al (2011) Limited overlap between the seismic gap and coseismic slip of the great 2010 Chile earthquake. Nat Geosci 4:173–177. doi: 10.1038/ngeo1073

Maerten F (2005) Inverting for Slip on Three-Dimensional Fault Surfaces Using Angular Dislocations. Bull Seismol Soc Am 95:1654–1665. doi: 10.1785/0120030181

Moreno M, Melnick D, Rosenau M, et al (2012) Toward understanding tectonic control on the Mw 8.8 2010 Maule Chile earthquake. Earth Planet Sci Lett 321-322:152–165. doi: 10.1016/j.epsl.2012.01.006

Okada Y (1985) Surface deformation due to shear and tensile faults in a half-space. Bull Seismol Soc Am 75:1135–1154.

Pollitz FF (1996) Coseismic deformation from earthquake faulting on a layered spherical Earth. Geophys J Int 125:1–14.

Pollitz FF, Brooks B, Tong X, et al (2011) Coseismic slip distribution of the February 27, 2010 Mw 8.8 Maule, Chile earthquake: CHILE EARTHQUAKE COSEISMIC SLIP. Geophys Res Lett 38:n/a–n/a. doi: 10.1029/2011GL047065

Seemüller W, Seitz M, Sánchez L, Drewes H (2009) The position and velocity solution SIR09P01 of the IGS Regional Network Associate Analysis Centre for SIRGAS (IGS RNAAC SIR). Munich Ger Dtsch Geod Forschungsinstitut Rep 85:96.

Snay RA, Freymueller JT, Pearson C (2013) Crustal Motion Models Developed for Version 3.2 of the Horizontal Time-Dependent Positioning Utility. J Appl Geod. doi: 10.1515/jag-2013-0005

Tong X, Sandwell D, Luttrell K, et al (2010) The 2010 Maule, Chile earthquake: Downdip rupture limit revealed by space geodesy: DOWNDIP RUPTURE MAULE, CHILE EARTHQUAKE. Geophys Res Lett 37:n/a–n/a. doi: 10.1029/2010GL045805

Vieira SR, Carvalho JRP de, Ceddia MB, González AP (2010) Detrending non stationary data for geostatistical applications. Bragantia 69:01–08.

Wang K, Hu Y, Bevis M, et al (2007) Crustal motion in the zone of the 1960 Chile earthquake: Detangling earthquake-cycle deformation and forearc-sliver translation. Geochem Geophys Geosystems 8:Q10010. doi: 10.1029/2007GC001721

Wessel P, Smith WH (1998) New, improved version of Generic Mapping Tools released. Eos Trans Am Geophys Union 79:579–579.

Zweck C, Freymueller JT, Cohen SC (2002) Three-dimensional elastic dislocation modeling of the postseismic response to the 1964 Alaska earthquake. J Geophys Res Solid Earth 1978–2012 107:ECV–1.

CHAPTER 4

Virtual array beamforming of GPS TEC observations of co-seismic ionospheric disturbances near the Geomagnetic South Pole triggered by teleseismic megathrusts

Published in the Journal of Geophysical Research, Space Physics

Introduction

Vertical ground displacement during seismic activity produce, by dynamic coupling, near and far-field acoustic and gravity waves that propagate in the neutral atmosphere. As acoustic waves propagate upwards, their amplitudes increase by a factor of $\sim 10^4$ in the ionosphere due to energy conservation as the density in the atmosphere decreases. At ionospheric altitudes, neutral particles couple with the ionized plasma perturbing the ionospheric electron density. The ionosphere is dispersive, with the dispersion proportional to the total electron content (TEC), the integrated electron density along the satellite-receiver line of sight (LOS). To correct for the effects of the dispersion, the GPS system uses two frequencies to estimate the TEC. These GPS TEC estimates can also be used to study ionospheric perturbations [*Mannucci et al.*, 1993].

Several authors have studied the propagation of TEC perturbations produced by different sources such as explosions, rocket launches [e.g. *Fitzgerald*, 1997; *Calais and Minster*, 1998; *Afraimovich et al.*, 2001], tsunamis [*Artru et al.*, 2005] and earthquakes [*Calais and Minster*, 1995] that produce a combination of acoustic and gravity waves that may be detected in the ionosphere. These studies have found that the generation and detection of these perturbations in the F-layer of the ionosphere depends on the orientation of the neutral perturbation with respect to the geomagnetic inclination and the sensitivity of the observational method being used (e.g. GPS, Doppler sounding and Over-The-Horizon radar) [*Occhipinti et al.*, 2013]. Therefore, the combination of geographic location (low-, mid- or high-latitude), observational method and type of disturbance (gravity or acoustic wave) play an important role in both the generation and detection of these signals. In this paper, we will discuss the application of a particular methodology (virtual array beamforming) in Antarctica, where the orientation of the geomagnetic field allows generating and observing acoustic wave-induced TEC signals produced by seismic activity.

The TEC perturbations produced by seismic activity are called co-seismic ionospheric disturbances (CID) [*Calais and Minster*, 1995; *Heki and Ping*, 2005; *Astafyeva and Afraimovich*, 2006; *Astafyeva et al.*, 2009]. There are two types of CIDs: low-frequency acoustic waves triggered in the epicentral area by vertical co-seismic offsets, and acoustic waves induced by the vertical component of propagating Rayleigh waves [*Rolland et al.*, 2011]. The propagation properties of these signals (e.g. apparent velocity and azimuth) are of great importance to understand the physical mechanism that governs this phenomenon. Most of the publications that use GPS to study these signals, obtain the apparent velocity using a time-distance diagram, a plot that shows the TEC perturbation amplitude as a function of time and distance from the source. The use of this diagram, however, depends on visual detection of the perturbation and, therefore, its signal to noise ratio (SNR) has to be high enough to allow the disturbance to be visually observed in the diagram as high and low TEC lineaments. The time-distance plot also does not provide azimuth information. While the first type of TEC wave can only be generated within approximately one fault length from the epicenter, the second type may be generated at teleseismic distances. Observations at teleseismic distances, or regions with noisy ionospheric environments, may result in signals with very low SNR (especially with low magnitude events), making use of a time-distance diagram challenging or even impossible.

To increase the SNR of the signal and estimate both apparent velocity and back azimuth (the direction to the source) we can use array beamforming, which is commonly used in seismology. For plane wave ionospheric disturbances, *Calais et al.* [2003] showed how to beamform observations obtained by a dense GPS network. This technique was developed for the analysis of traveling ionospheric disturbances (TIDs) rather than acoustic plane wave induced TEC signals, such as CIDs, although some authors have applied slant-stacking, a 1-D version of beamforming, to CIDs [*Afraimovich et al.*, 2001; *Astafyeva et al.*, 2009; *Dautermann et al.*, 2009]. A significant difference between the seismic and TEC GPS arrays is that the former provides measurements at fixed locations, those of the seismometers, while the latter provides measurements at the ionospheric piercing points (IPP), the moving intersections of the satellite-receiver LOS and the peak electron density in the ionospheric F-layer. The most basic GPS array is built from the IPPs between a set of GPS stations and a single satellite. We will refer to the array of IPPs where the TEC measurements are made as a virtual array because the observations are not obtained by physical sensors at the IPPs. Each GPS receiver records a TEC signal at the IPP that for a plane wave has a delay proportional to the apparent velocity of the signal and the position of the sensor along the raypath. Beamforming searches the delay space to find the set of delays producing the maximum energy of the stacked data, therefore amplifying the signal. This set of delays defines the plane wave apparent velocity and back azimuth.

Although GPS arrays have proven useful for observing TEC waves, the standard application does not take into account the following four effects. The first and second effects are related to coupling between the neutral atmospheric wave and the ionospheric plasma, and the geometrical relationship between the LOS and the propagation direction of the acoustic wave [*Georges and Hooke*, 1970]. These two effects alter the phase and amplitude of the TEC signals with respect to the inducing acoustic wave, i.e. the TEC signals are no longer plane waves and cannot be used in beamforming. The third effect is related to the average movement of the array, which can change the estimated apparent velocity and back azimuth, although in certain cases this effect may be ignored. Finally, deformation of the internal geometry of the array can result in an incorrect stacking.

To apply beamforming based on GPS TEC data, we will obtain an inverse transfer function using a model for GPS TEC observations to invert for the neutral acoustic wave that produced the TEC perturbation. Next, virtual array beamforming will be described and applied to the inverted neutral acoustic waves. Finally, we will apply virtual array beamforming to the inverted neutral acoustic waves during the passage of seismic waves from the Maule and Tohoku-Oki earthquakes from the Antarctic Network (ANET) component of the Polar Earth Observing Network project. The apparent velocities, back azimuths and waveforms are found to agree with the hypothesis that they were produced by Rayleigh wave-induced acoustic waves from the earthquakes. The epicentral distances of ~7,500 km and 12,500 km from the Maule and Tohoku-Oki earthquakes, respectively, make these, to our knowledge, the farthest observations of CIDs ever recorded with GPS.

A model for GPS TEC observations

Georges and Hooke [1970] developed a model (henceforth, the G&H model) coupling mono-frequency acoustic waves to the ionospheric plasma. This model quantifies the phase and amplitude of the induced GPS TEC measurements occurring in a plane-stratified F layer in the presence of a constant geomagnetic field, observed along the LOS to geostationary or moving satellites. We applied the G&H model at each IPP to account for the spatial variation of the geomagnetic field using the International Geomagnetic Reference Field (IGRF, see Data Sources section) to improve modeling of the acoustic wave-induced TEC signals. We use this model with some further approximations to estimate the effect of Rayleigh waves on the ionosphere because our goal is to develop a beamforming technique rather than study the TEC response in detail. For a complete model of the effect of Rayleigh waves in the ionosphere, the reader should refer to *Rolland et al.* [2011] (using TEC observations) and *Artru et al.* [2004] (using Doppler sounding observations).

We simulate Rayleigh wave-induced acoustic wave packets in the neutral atmosphere by modulating a mono-frequency traveling wave with a moving exponential traveling taper, both traveling with the same speed:

$$u(\mathbf{r},t) = A\exp[i(\omega t - \mathbf{k}\cdot\mathbf{r})]\exp\left[-(\omega t + \mathbf{k}\cdot\mathbf{r})^2 / \sigma\right] \tag{1}$$

where **k** is the wave-number and **r** is the IPP LOS vector, *A* is the amplitude of the traveling wave packet, ω is the angular frequency of the traveling wave, and σ is a constant that controls the width of the exponential taper. This simplistic mono-frequency model is consistent with the G&H model, which requires a mono-frequency wave input to obtain the TEC response. Furthermore, the solid earth modes couple efficiently with the atmosphere at resonant frequencies of ~3.7 and ~4.4 mHz [*Lognonné et al.*, 1998, 2006; *Artru et al.*, 2004; *Rolland et al.*, 2011]. This coupling acts as a narrow band-pass filter on the induced atmospheric wave, which then couples to the ionospheric plasma. To remove other TEC signals that do not match the resonant frequency of ~4.4 mHz, we will apply a narrow band pass filter to the TEC times series. The filtering is also appropriate for use with beamforming and the G&H mono-frequency model.

Another simplification that we have imposed is that the transfer function between the solid earth and the atmosphere is equal to one, which means that we have not modeled the solid earth-atmosphere coupling. Equation (1), therefore, can be used to model both the acoustic wave and the inducing solid earth Rayleigh wave, both of which have back azimuths that approximately point to the location of the epicenter. The vertical component of the Rayleigh wave will produce an acoustic wave with a take-off inclination angle that can be estimated using simple wave propagation geometry. For a reasonable value of Rayleigh wave speed (~4 km/s) and sound speed at sea level (~0.33 km/s), the take-off inclination angle is ~5°. To provide the best estimate of the acoustic wave at the ionosphere we raytrace the acoustic wave from the ground surface to ionospheric altitudes before applying the G&H model. During this raytrace, we did not consider atmospheric dispersion, since this effect is small and usually ignored in propagation models for TEC perturbations, especially in low energy events [*Dautermann et al.*, 2009].

Garcés et al. [1998] presented a tau-*p* method for sound waves propagating in a stratified atmosphere under the influence of horizontal height-dependent winds. Using this 1-D raytrace, we estimate the propagation azimuth and incidence angle of the acoustic wave at ionospheric altitudes. The initial propagation azimuth at ground level is assumed to be that of the Rayleigh wave propagating from the epicenter. As the wave propagates upwards, this initial azimuth will suffer from changes produced by horizontal winds. Atmospheric temperature and height-dependent winds were estimated using the NRL-MSISE model [*Picone et al.*, 2002] and the Horizontal Wind Model 2007 (HWM07) [*Drob et al.*, 2008]. In Antarctica, strong winds produce variations in azimuth and inclination between ~-40º to 40º and ~10º to 17°, respectively. Previous implementations of similar ray tracing techniques have proven to be adequate to estimate the acoustic ray path [*Dautermann et al.*, 2009].

Next, we couple the neutral wave with the ionospheric plasma to obtain the TEC response observed using GPS. For a LOS that crosses the whole ionospheric F layer, the observed change in ambient TEC induced by an acoustic plane wave is given by:

$$C = \left[u e^{i(\omega t + \eta h_m)} \right] \left[\frac{1}{\omega \cos^2(\chi)} \right] [(\hat{\mathbf{k}} \cdot \hat{\mathbf{b}})(\hat{\mathbf{r}} \times \hat{\mathbf{b}}) \times \hat{\mathbf{z}} \cdot \mathbf{k}] \left[\int_{-\infty}^{\infty} n_{e0}(h_m + z') e^{(i\eta z')} dz' \right] \quad (2)$$

where $\hat{\mathbf{b}}, \hat{\mathbf{r}}, \hat{\mathbf{z}}, \hat{\mathbf{k}}$ are the unit vectors for the geomagnetic field, LOS, vertical and wave propagation directions, ω is the angular frequency, u is the amplitude of the neutral gas motions, $\mathbf{k}$ is the wave-number vector of the neutral gas wave (for a neutral acoustic wave, $\mathbf{U} = u\hat{\mathbf{k}}$), χ is the satellite zenith angle, $\eta = -\frac{\mathbf{k} \cdot \mathbf{r}}{h_m}$, h_m is the altitude of the peak ionospheric electron density, $\mathbf{r}$ is the position vector of the IPP, $z' = z - h_m$, and $n_{e0}(z)$ is the unperturbed electron density value as a function of altitude [*Georges and Hooke*, 1970]. It should be noted that we are only considering pressure waves, such as those observed in Rayleigh wave-induced acoustic waves. This can be justified by calculating the acoustic cut-off frequency, estimated using the atmospheric temperature values from the NRL-MSISE model. The estimated acoustic cut-off frequency has a typical value of ~3.3 mHz [*Artru et al.*, 2004] up to an altitude of ~90 km, where it reaches a maximum value of ~3.9 mHz, below the narrow band pass filter (4 - 7 mHz) applied to the TEC time series. To facilitate discussion of (2), we have broken it into four terms (in brackets): the travelling wave, satellite elevation, geometrical, and phase cancellation terms. A very detailed analysis and the derivation of this model can be found in *Georges* [1968], *Hooke* [1968] and *Georges and Hooke* [1970].

To use the virtual array beamforming technique, we need to obtain the transfer function between the neutral wave and the ionospheric plasma. Following *Georges and Hooke* [1970] and integrating the phase cancellation term in (2) for an α-Chapman profile, we obtain:

$$PC = \frac{2^{-i\eta H}}{\sqrt{\pi}} \Gamma\left(\frac{1}{2} - i\eta H\right), \tag{3}$$

where *PC* denotes the phase cancellation term of an acoustic plane wave propagating with **k**, Γ is the gamma function of complex argument, and *H* is the α-Chapman scale height (thickness of the ionosphere). Equation (3), which is complex valued, provides an estimate of the phase and amplitude of the TEC response at each IPP [*Georges and Hooke*, 1970]. The phase change of the TEC response with respect to the neutral acoustic wave, expressed by (3), will have the largest impact in beamforming, and will be discussed later.

We will now briefly examine the geometrical term:

$$G = [(\hat{\mathbf{k}} \cdot \hat{\mathbf{b}})(\hat{\mathbf{r}} \times \hat{\mathbf{b}}) \times \hat{\mathbf{z}} \cdot \mathbf{k}] \tag{4}$$

Amplitude changes of the TEC response do not have a large influence on beamforming, because they only produce a weighting effect on each trace, affecting the magnitude of the stacked signal. These terms, however, are important because they can produce a sign change in the TEC response, which masquerades as a 180º phase shift that would change constructive interference into destructive interference during beamforming. Since $\hat{\mathbf{b}}$ is near vertical at the geomagnetic poles and Rayleigh wave induced acoustic waves propagate almost vertically, the $\hat{\mathbf{k}}$ and $\hat{\mathbf{b}}$ are sub parallel in Antarctica and the $\hat{\mathbf{k}} \cdot \hat{\mathbf{b}}$ term should not produce sign changes in the TEC response. The $(\hat{\mathbf{r}} \times \hat{\mathbf{b}}) \times \hat{\mathbf{z}} \cdot \mathbf{k}$ term, however, is related to the relative orientation of the geomagnetic field and the observation direction (assuming a constant $\mathbf{k}$). If we consider the case of having constant **k** and $\hat{\mathbf{b}}$, a change in direction of $\hat{\mathbf{r}}$ can generate a change in sign of the dot product with **k**.

Finally, we have the satellite elevation term:

$$SE = \left[\frac{1}{\omega \cos^2(\chi)} \right] \tag{5}$$

which provides another amplitude change. This term expresses the sensitivity change of a GPS LOS to an acoustic wave-induced TEC signal, which varies with LOS zenith angle, χ, as $\cos^{-2}(\chi)$. This term has no influence in beamforming other than increasing the SNR of the acoustic wave-induced TEC signal. We will return to the influence of GPS orbit geometry and satellite elevation angle on the sensitivity to acoustic wave-induced TEC signals in Antarctica later.

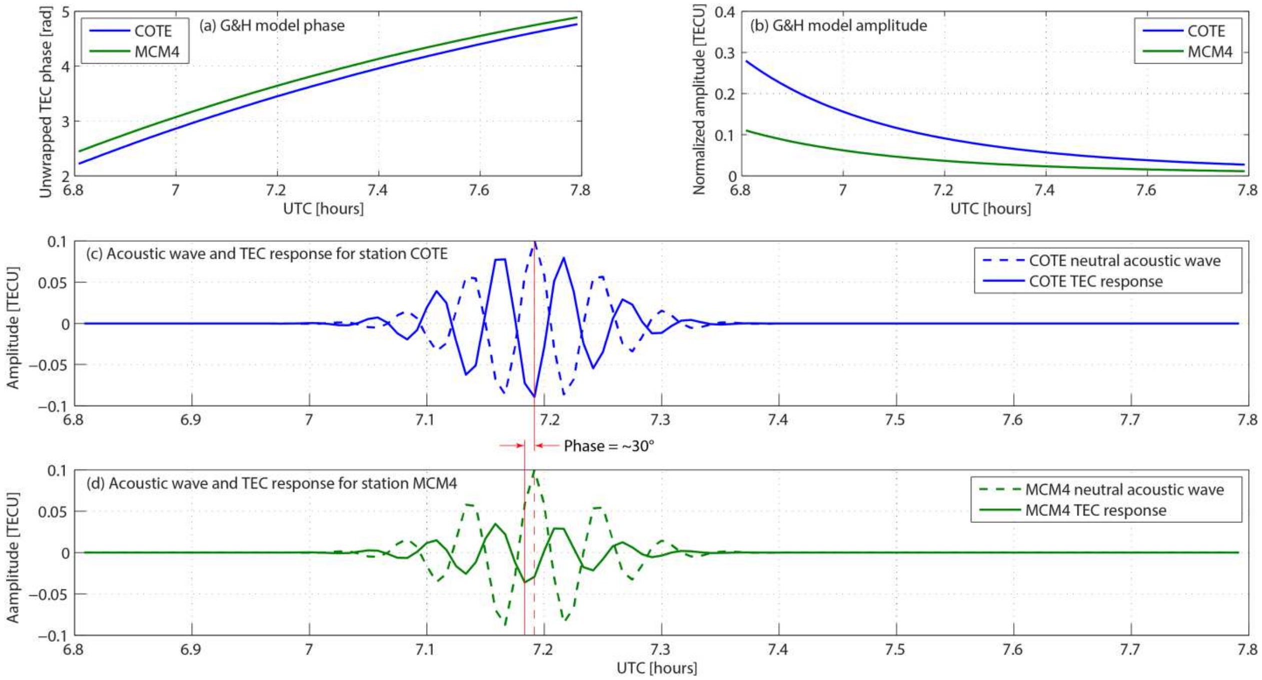

Figure 1. Synthetic TEC response to an acoustic wave using the G&H transfer function. (a): Phase of the TEC response as a function of time for GPS stations COTE and MCM4. (b): TEC amplitude response as a function of time. c) Acoustic wave produced using a simple Rayleigh wave model (dashed line) and the corresponding TEC response (solid line) for station COTE. Vertical solid red line shows the maximum amplitudes of the TEC and acoustic wave signals that have a phase difference of ~180º. (d): Same as (c), for station MCM4. Vertical solid red line shows the maximum amplitude of the TEC signal, while the dashed line shows the maximum amplitude of the acoustic wave signal with a phase difference is ~150º. The phase difference between the TEC responses at COTE and MCM4 is ~30º.

Combining (3), (4) and (5), we obtain the equation of the G&H transfer function, which is independent of the shape of the mono-frequency acoustic wave:

$$T = \left[\frac{1}{\omega\cos^2(\chi)}\right][(\hat{\mathbf{k}}\cdot\hat{\mathbf{b}})(\hat{\mathbf{r}}\times\hat{\mathbf{b}})\times\hat{\mathbf{z}}\cdot\mathbf{k}]\left[\frac{2^{-i\eta H}}{\sqrt{\pi}}\Gamma\left(\frac{1}{2}-i\eta H\right)\right]. \tag{6}$$

We analyzed the phase and amplitude effects of (6) using the acoustic wave model in (1) with the parameters of a synthetic acoustic wave produced by the Maule earthquake, two GPS stations located in Antarctica (COTE and MCM4), the International Reference Ionosphere (IRI) model [*Bilitza et al.*, 2014], and the IGRF model to obtain values for H, h_m and $\hat{\mathbf{b}}$. Figure 1a and b shows the phase and amplitude of the transfer function as a function of time, where we show that the phase of the TEC response can be different for the two IPP, and that this difference changes as a function of time. A similar effect can be observed for the amplitude in Figure 1b, since the amplitude of the TEC response is different and also changes as a function of time.

Figure 1c and d show a phase shift of ~180° in the TEC responses. The response for MCM4, however, differs from that of COTE by ~30°. In addition to the time delay introduced by the distance between COTE and MCM4, the phase shift introduced by the G&H transfer function adds an additional phase shift, marked in Figure 1d by the difference between the vertical solid and dashed red lines. This synthetic test shows that, for two locations relatively close to one another, the TEC response to an acoustic wave can have a significant time shift difference introduced by the phase cancellation term in (3). Since the phase of the wave-induced TEC signal changes non-uniformly across an array, we cannot beamform the raw TEC data because their phases do not correspond to those of a plane wave. In the following section we will describe how to invert for the plane acoustic wave that induced the TEC signal.

Recovery of the neutral acoustic wave

The transfer function between the acoustic wave and the resulting induced TEC wave is complex, producing amplitude and phase changes in the TEC observation with respect to the acoustic wave. We will now develop the inverse transfer function to obtain the neutral acoustic wave from the TEC observations.

First, we will isolate the terms that only affect the phase of the transfer function: the phase cancellation, (3), and geometrical, (4), components. Normalizing (3) and considering only the sign of (4), we find the G&H forward transfer function phase contribution:

$$F = sgn([(\hat{\mathbf{k}}\cdot\hat{\mathbf{b}})(\hat{\mathbf{r}}\times\hat{\mathbf{b}})\times\hat{\mathbf{z}}\cdot\mathbf{k}])\left[\frac{\dfrac{2^{-i\eta H}}{\sqrt{\pi}}\Gamma\left(\dfrac{1}{2}-i\eta H\right)}{\left|\dfrac{2^{-i\eta H}}{\sqrt{\pi}}\Gamma\left(\dfrac{1}{2}-i\eta H\right)\right|}\right]. \tag{7}$$

As $\eta, H, \mathbf{k}, \hat{\mathbf{k}}, \hat{\mathbf{b}}, \hat{\mathbf{r}}$ and $\hat{\mathbf{z}}$ are known, we can evaluate (7). To invert for the acoustic input wave, therefore, we divide the analytic signal (obtained using the Hilbert transform) of the TEC time series by (7) keeping only the real part. Note that because (7) is normalized, the input acoustic wave will have the same amplitude as the TEC signal.

Assuming a **k** for (7), which corresponds to a wave produced by a “test” source, we can invert for the acoustic wave that induced the observed TEC signal. We then beamform these inverted signals, using the virtual beamform algorithm described later, to stack and amplify the acoustic plane wave and obtain an estimate of its **k**. If the beamformed **k** agrees with the **k** of the test source, and the synthetic TEC signal, obtained from forward modeling using (1) and (6), also agrees with the observed TEC time series, this provides a solid confirmation that the observed TEC signals were produced by the test source used to obtain the inverted acoustic waves.

In this work we have only applied the inverse transfer function using the test sources that correspond to those of the Maule and Tohoku-Oki earthquakes, because it is out of our scope to search for other TEC signals. Therefore, the acoustic plane wave of another TEC signal produced by a different source (ergo, with a different **k**) is not correctly recovered. As a consequence, the beamform will not correctly stack signals with other than the test **k**. This limitation is also related to the fact that performing an acoustic ray trace for each **k** in the search space is very computationally expensive. If the effect of the winds can be ignored, applying the inverse transfer function for each **k** is, more or less, trivial and the inverse transfer function can be applied for every **k** in the search space allowing the beamform to find the acoustic plane wave that produces the maximum energy in the stack. In Antarctica the effect of the strong winds cannot be ignored and, therefore, one ray trace is needed for each **k** if we want to allow the beamform to search for the signal without any a priori information. In this work, however, we are searching for a specific signal for which we know the propagation parameters that allow us to use a test source.

We should note that, even for cases where we select an incorrect test source, the beamform will not detect a false signal if no acoustic plane wave is present in the time series. Furthermore, if a signal corresponding to a different source randomly stacks when applying an incorrect test source, the synthetic TEC time series will not agree with the GPS TEC measurements and, therefore, the test source can be discarded as the origin of the TEC disturbance. For the case of Rayleigh wave-induced signals, the detection of a signal can be further confirmed by comparing a seismogram waveform with the stacked acoustic wave signal.

Virtual array processing

We now present the virtual array technique and how it can be applied in a more general context, allowing array movement and deformation. A traveling wave at a fixed observation point located at $\mathbf{r}$ can be represented by:

$$u(t,\mathbf{r}) = f(t - \mathbf{p}\cdot\mathbf{r}), \tag{8}$$

where $u(t)$ is the observed signal at $\mathbf{r}$ (e.g. a seismogram), $f(y)$ gives the shape of the wave as a function of the argument, $y = t - \mathbf{p}\cdot\mathbf{r}$, t is time, and $\mathbf{p}$ is the slowness vector or ray parameter, defined as $\mathbf{p} = v^{-1}\left[\cos(\theta), \sin(\theta)\right]$, where v is the apparent velocity of the wave and θ is the horizontal azimuth of the traveling wave. For an array of sensors, each array element, *i*, will produce a time series:

$$u_i(t, \mathbf{r}_i) = f(t - \mathbf{p}\cdot\mathbf{r}_i). \tag{9}$$

As the ray parameter is a constant, it can be estimated by finding the time shifts, which are a function of $\mathbf{r}_\mathbf{i}$ and the ray parameter, that align the $u(t,\mathbf{r}_\mathbf{i})$ such that they constructively interfere. This is accomplished by performing a grid search over the domain of the ray parameter (see *Rost and Thomas* [2002] for a complete review).

When observing TEC in the ionosphere using GPS, the array sensors are the IPPs. Because of the relative motion between the satellites and a point on the surface of the Earth, the position of the IPPs is a function of time. Taking this movement into account (9) becomes:

$$u_i\left[t, \mathbf{r}_i(t)\right] = f[t - \mathbf{p}\cdot\mathbf{r}_i(t)]. \tag{10}$$

Since $\mathbf{r}_i(t)$ is now a function of time, this introduces potential rotation with respect to the geographic coordinate system, translation, and deformation of the array.

To apply beamforming to a moving array we first need to address some geometrical considerations related to the rotation of the array with respect to the geographic coordinate system that are especially important near the geographic poles. In standard beamforming, where the sensors are fixed, a local coordinate system is used to specify the coordinates $\mathbf{r}_i$. This coordinate system is constant during the time of the analysis, and typically aligned with true north to obtain the orientation of the traveling plane wave, since **p** is a function of the horizontal azimuth, θ, in the coordinate system. In general, for the case of a moving array, both the location of the array and the direction of true north will change as a function of time. This change in the direction of true north is particularly strong at high latitudes, where small changes in position result in large rotations in a local coordinate system aligned with true north. In this study, the Rayleigh wave-induced signals are ten to twenty minutes in duration, and we are far enough from the geographic pole that the change in orientation during this time period, due to the rotation with respect to true north of the array, is small and can be ignored.

We will now examine the effects of the translation and deformation of an array on beamforming. The deformation of the array will produce a changing internal array geometry that, due to the dependence on $\mathbf{r}_i(t)$, is equivalent to having a different array at each time sample. This can be illustrated by considering a series of snapshots of the wavefield centered on the array and oriented with respect to true north, with the position of the array sensors marked in each snapshot. A Doppler shift in the time series at each sensor will be generated by the movement of the sensors with respect to the wavefield. By considering each time sample as an independent array, however, we will see that we do not have to explicitly correct for this Doppler shift.

To beamform, each time series is shifted to bring it to the origin of the instantaneous coordinate system, which can be a particular array sensor. Because each snapshot (time sample) is considered to form an independent array, it will have its own time shift given by:

$$\tau_i[\mathbf{p},\mathbf{r}_i(t)] = \mathbf{p}\cdot\mathbf{r}_i(t) = p_x x_i(t) + p_y y_i(t). \tag{11}$$

where $x_i(t), y_i(t)$ are in the instantaneous local Cartesian coordinate system. The standard beamform time shift $\tau_i[\mathbf{p},\mathbf{r}_i(t)]$ applied to the instantaneous array removes the requirement to explicitly correct for the Doppler shift due to the array deformation. We should note that because the components of both **p** (recalling that **p** is a function of the horizontal azimuth) and $\mathbf{r}_i(t)$ are a function of an instantaneous local coordinate system, the time shift to bring each sample to the origin position, $\tau_i[\mathbf{p},\mathbf{r}_i(t)]$, is not constant and the shifting operation for beamform stacking must therefore be performed in the time domain.

Let the origin of the instantaneous local coordinate systems be assigned to one of the array sensors, hereafter the “reference sensor” (RS). By (11) no time shifts will be applied to its time series. While we do not have to explicitly consider the Doppler shift from the array deformation, the Doppler shift generated by the movement of the RS itself still has to be considered. This Doppler shift will generate a difference in the estimated ray parameter and back azimuth. If the velocity of the array is much, much, less than the apparent velocity of the wave, the error introduced into the back azimuth and apparent velocity estimate will be small and the apparent velocity found by beamforming will be the sum of the wave apparent velocity and the velocity of the array.

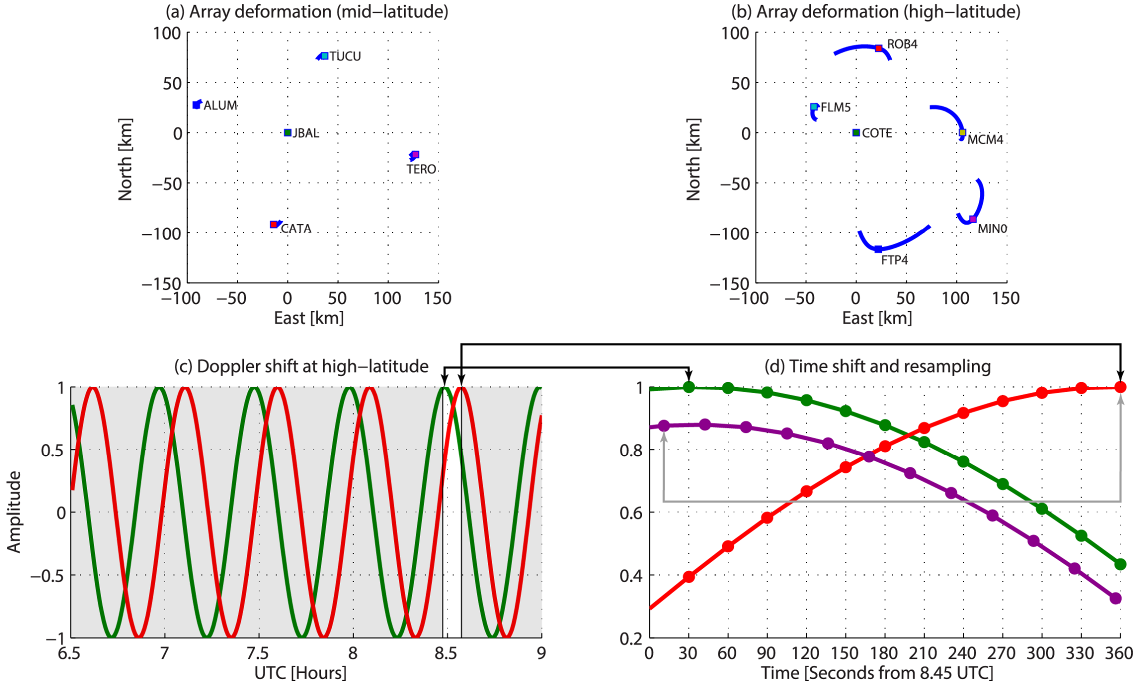

Figure 2. Comparison of deformation as a function of time for a virtual array over four hours at mid-latitudes (a) and two and a half hours at high-latitudes (b) showing deformation is insignificant for the mid-latitude array but very large for the high-latitude array. (c) During the high-latitude time window, we show a traveling sine wave with a back azimuth of 270º recorded by COTE (the RS, green) and ROB4 (red). The Doppler shift observed in the time series due to the deformation of the high-latitude array is removed by the time shift based on the instantaneous array geometry during beamforming. (d) We show the unshifted traveling sine waves between ~8.45 and ~8.55 UTC (white section of the plot in c). Dark arrows connecting plots c and d show the correspondence between time samples of each time series. The time samples of the red and green traces match (solid circles). We apply the variable beamforming time shifts to align the time series of ROB4 (purple) with COTE (green). The light arrow shows the correspondence between the unshifted and beamform shifted position of a time sample. The time samples of the beamform shifted ROB4 time series are no longer coincident with those of COTE (green), and therefore, resampling is necessary before stacking. We applied a small vertical offset to the amplitude component of ROB4 to better visualize both time series.

Figure 2 shows a summary of these effects and how observations at different latitudes can produce different array deformations. Figure 2a and b show two virtual arrays around the time of the Maule earthquake, one at mid-latitudes from the Maule area of South America during a four hour time window (Figure 2a) and the other at high-latitudes in Antarctica during a two and a half hour time window (Figure 2b). The blue traces show the displacement time series of each

IPP in their local coordinate systems. As can be clearly seen, the deformation of the high-latitude array is significantly larger than that at mid-latitude. This difference is due to the GPS satellite orbit geometry. For the mid-latitude array, where satellites can be found at high elevation angles and the deformation is minimal, standard beamforming works as in *Calais et al.* [2003]. For high-latitude arrays, however, the satellite elevations are much lower, the IPPs move much faster than at mid-latitude, significantly deforming the array and requiring the procedure described here. We should note that basing an array on a low elevation satellite at mid-latitudes will also result in a similarly, rapidly deforming array.

In Figure 2c we show the time series of a traveling sine wave to illustrate the Doppler shift produced by the deformation of the array for two IPPs (COTE and ROB4) of the high-latitude array. Taking a smaller time window (between ~8.45 and ~8.55 UTC), we plot the unshifted time series in Figure 2d showing the individual, simultaneous, samples. We then time-shift each sample of ROB4 using the procedure above to align it with the RS, COTE. We now observe that in the time-shifted series of ROB4, the sample rate is non-uniform and the sample times are different from those of COTE. We therefore have to resample the time series of ROB4 before stacking.

Now we have time series representing a plane wave (we use the inverted acoustic wave signals obtained from the TEC observations, not the raw TEC data) crossing a standard array. This more general method, that allows a large deformation of the array, can be applied to acoustic wave signals inverted from the TEC time series to recover low SNR TEC signatures in noisy ionospheric environments such as Antarctica [*Hunsucker and Hargreaves*, 2002].

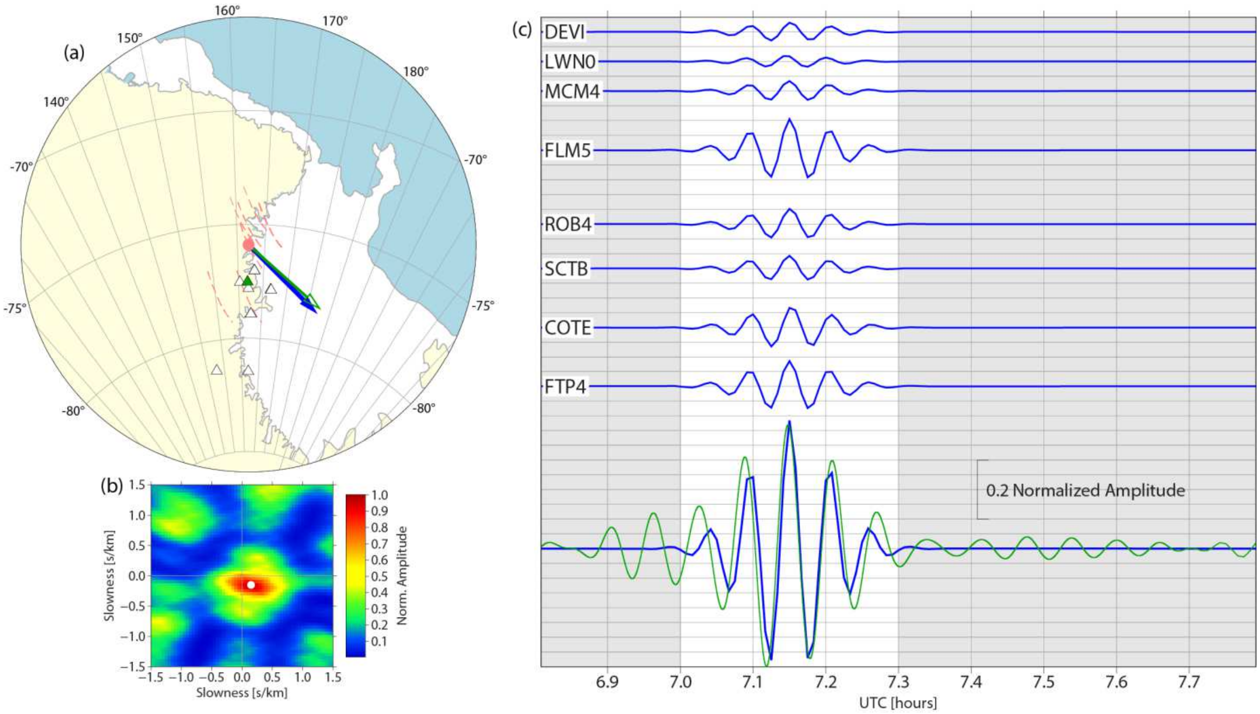

Figure 3. Results for virtual array beamform of synthetic acoustic waves, not coupled to the ionospheric plasma, produced by the Maule earthquake. This represents the input signal to the ionosphere. (a): map showing the beamform estimated back azimuth (blue arrow, ~135°), the great circle back azimuth (green arrow, ~131°) and the virtual array IPP's paths (red dashed lines) (b): beamform plot showing the maximum energy stack with a slowness of ~0.22 s/km (speed = ~4.5 km/s), in agreement with the synthetic Rayleigh wave speed of 4.2 km/s (c): Top, time shifted, acoustic wave synthetics at each GPS station (blue traces). Bottom, acoustic wave stack result (blue trace), and time-shifted seismogram (green trace) recorded at seismic station VNDA (green triangle), to show the agreement between our synthetic Rayleigh wave model and the seismic data.

We tested the virtual array beamform with synthetic data at an eight element array to show that it can successfully estimate apparent velocity and back azimuth of plane wave signals on an array that is experiencing large deformations, as happens in high-latitude locations. We used the simple Rayleigh wave model in (1) propagating with a phase velocity of 4.2 km/s and a back azimuth at the array of ~131°. The estimated apparent velocity and back azimuth was ~4.5 km/s and ~135°, respectively, which is in very good agreement with the input data (Figure 3a and b). We also note that the proposed simplistic Rayleigh wave model is a good approximation for a narrow-band passed Rayleigh wave signal, as shown by the agreement between the stacked synthetics in Figure 3c and the band passed (4 to 7 mHz) vertical component of the seismogram recorded at Wright Valley, (VNDA), Antarctica, during the passage of seismic waves from the Maule earthquake.

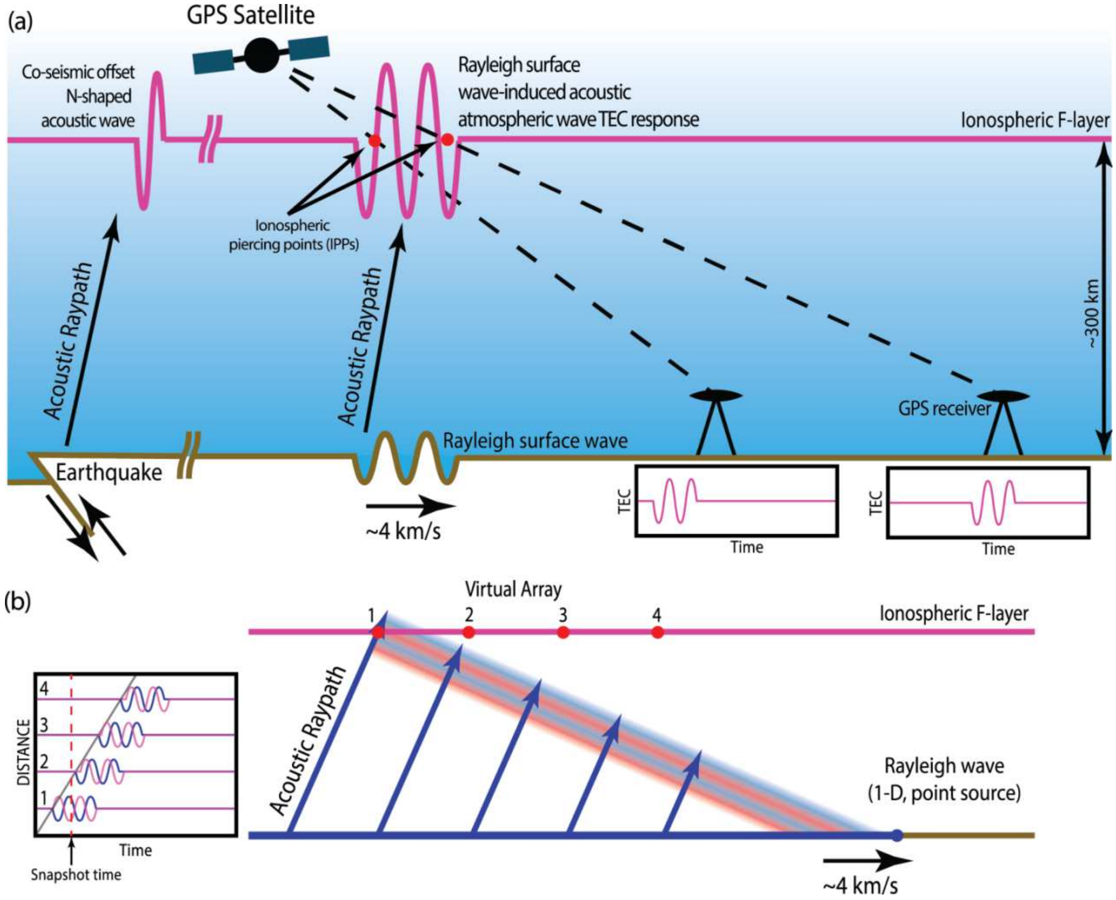

Figure 4. Ionospheric TEC observation diagram. (a): Diagram of the ionospheric piercing point (IPP) geometry and acoustic raypath. Two GPS stations are shown with their TEC signal plots. (b): Relation between virtual array beamformed apparent velocity and Rayleigh wave phase velocity. The diagram does not illustrate the temporal deformation of the array and assumes a windless and constant sound speed atmosphere. The left pane shows the acoustic wave amplitude as a function of time and distance (blue lines) and the TEC response (magenta lines). Note that the phase of the TEC response is different at each IPP to show the effect of the coupling between the neutral wave and the ionospheric plasma.

Before describing the conditions that allow observing teleseismic Rayleigh wave-induced TEC signals in Antarctica, we will review the relation between the apparent velocity obtained by beamforming on a virtual array and the Rayleigh wave phase velocity. Figure 4a presents a simple diagram showing the components of GPS ionospheric observations. When an earthquake occurs, an N-shaped acoustic wave from the co-seismic vertical component (first type of CID, see introduction) is induced in the near-field atmosphere. In the mid- to far-field, the Rayleigh wave induces an acoustic wave that produces TEC perturbations after coupling with the ionospheric plasma.

Figure 4b shows that, in 1-D, Rayleigh waves can be modeled as a traveling point source. The traveling point source releases energy into the atmosphere that travels almost vertically with the speed of sound. In this example, we have assumed a windless, homogeneous atmosphere to simplify our diagram. When the wave reaches each IPP of the virtual array (after coupling with the ionospheric plasma), the delay between each arrival is that of the horizontal speed or apparent velocity of the wave. The ray parameter determined by the beamform of the induced acoustic wave is equal to the ray parameter of the inducing Rayleigh wave, which is the inverse of its phase velocity. Although the ray parameter of an ideal wavefront is constant throughout the atmospheric propagation, localized winds and temperature variations may distort the wavefront and change the arrival time of individual rays to each IPP. This deformation of the wavefront due to winds, however, can be removed by raytracing the acoustic wave.

Observation of teleseismic Rayleigh waves in Antarctica

TEC signatures produced by Rayleigh wave-induced acoustic waves have previously been observed as far as ~3000 km from earthquakes [*Heki and Ping*, 2005; *Astafyeva and Afraimovich*, 2006; *Astafyeva et al.*, 2009; *Galvan et al.*, 2012]. Beyond this distance, attenuation of the ionospheric TEC response to Rayleigh waves appears to fall-off, either because of the attenuation of the Rayleigh waves or because conditions to observe ionospheric wave-induced perturbations (geomagnetic field inclination, LOS orientation, etc.) are not met beyond some distance.

The elevation angle of GPS satellites due to the GPS orbit inclination is of particular importance in Antarctica when observing Rayleigh wave-induced TEC signals. From (6) we find that the observation of the wave induced change in TEC varies with LOS zenith angle, χ, as $\cos^{-2}(\chi)$. This term becomes large for low satellite elevation (large χ), increasing the sensitivity to TEC waves as the LOS elevation decreases. A review of observations of ionospheric perturbations as a function of satellite elevation done by *Rolland et al.* [2011] also concluded that low satellite elevations favor the observation of ionospheric Rayleigh wave-induced perturbations.

Polar regions are therefore optimal for observing Rayleigh wave CIDs in the ionosphere, because of the low elevation of GPS satellites and the efficient coupling with the ionospheric plasma produced by acoustic waves that are sub parallel to the geomagnetic field. This is supported by the observations reported here of Rayleigh wave-induced TEC perturbations produced by very distant seismic sources in the vicinity of the Geomagnetic South Pole.

Virtual Beamforming the Maule earthquake TEC signals in Antarctica

We performed virtual array beamforming on band-passed (4 to 7 mHz, or 2.38 to 4.16 minute period) acoustic waves, inverted from the TEC time series using the G&H inverse transfer function (7), for a wave-number vector corresponding to Rayleigh waves of the Maule earthquake, for a set of ANET stations in the vicinity of McMurdo (DEVI, LWN0, MCM4, FLM5, ROB4, SCTB, FTP4 and COTE), using satellite PRN02 on the day of the Mw 8.8 Maule earthquake (location 35.909°S, 72.733°W, depth 35 km on 27/02/2010 at 06:34:14 UTC). Although the SNR of the TEC signals is much lower than that of signals typically observed around epicentral areas [*Calais and Minster*, 1995; *Astafyeva and Afraimovich*, 2006; *Astafyeva et al.*, 2009; *Galvan et al.*, 2012], the beamform clearly detected the signal at the array, even though it is difficult to identify the signal in each individual time series.

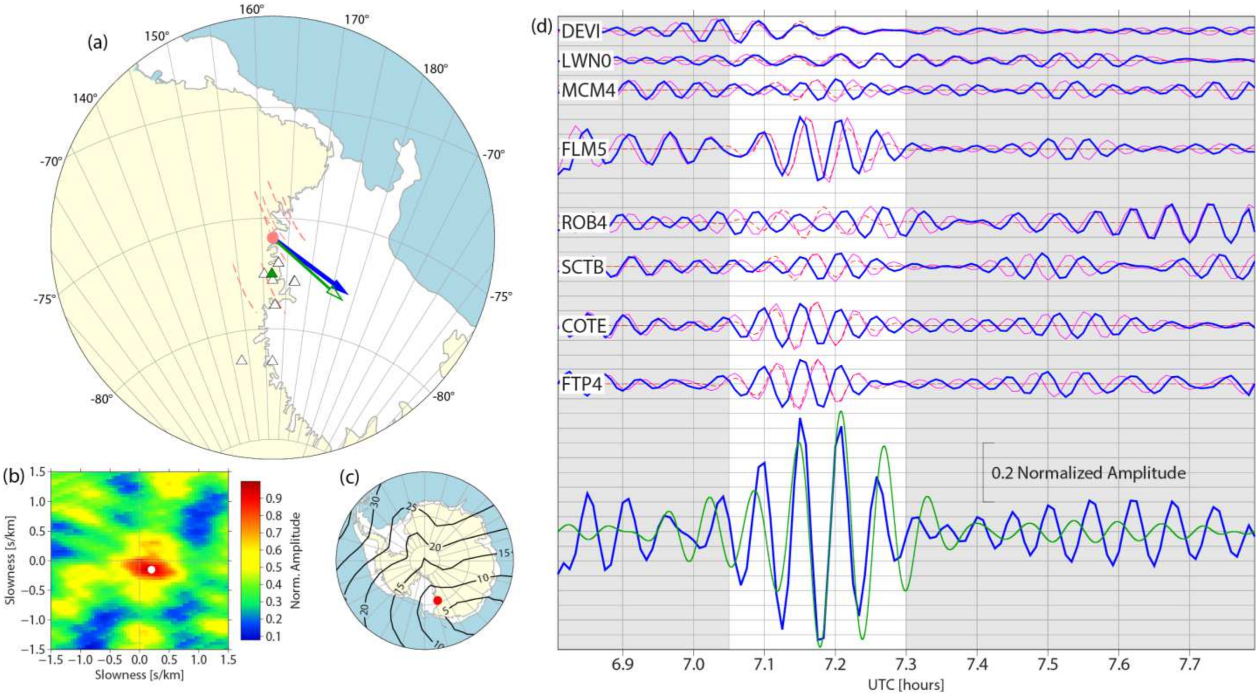

Figure 5. Results for virtual array beamform of CIDs produced by the Maule earthquake. (a): Location map. White triangles show GPS stations, green triangle shows VNDA seismic station. Red dashed lines show IPP paths. Red filled circle shows the array center location. Arrows show the back azimuths; to epicenter –green ~135°, estimated using beamforming –blue ~126°. (b): white circle shows the beamform stacking slowness (speed, ~4 km/s). (c): Contour map showing the inclination of the geomagnetic field lines and the position of the virtual array, red filled circle (~7.5°). (d), top: TEC observations -magenta, TEC synthetics –dashed red, using the Rayleigh wave back azimuth and speed (4 km/s), the atmospheric temperature (MSIS), wind (HWM07), geomagnetic (IGRF) and G&H models; bottom: stacked TEC signal using the beamform virtual array - blue; vertical component of seismogram recorded at VNDA station – green. The seismic trace is vertically scaled to match the acoustic wave amplitude and shifted in time using the atmospheric ray tracing.

Figure 5a and b show the map and beamform response, respectively, of a virtual array located in a region where the geomagnetic field lines are almost vertical (inclination of ~7.5°) as shown by Figure 5c. We estimated an apparent velocity of ~4 km/s (slowness of 0.25 s/km) and a back azimuth of ~126° that is in excellent agreement with the arrival of Rayleigh waves produced by the Maule earthquake. The virtual array response plot (Figure 5b) is also in good agreement with the synthetic test in Figure 3b.

Figure 5d shows the synthetic TEC traces obtained using the G&H model, and the observed TEC signals for each IPP. We verify that the synthetic TEC time series, obtained using the Rayleigh wave function described by (1), are in good agreement with the TEC measurements. To obtain a better fit between the synthetics and TEC measurements, we estimated the ionospheric scale height from the IRI model allowing a small variation of less than 5% until the residual between model and data was minimized. We also show the time shifted, acoustic wave signals inverted using the inverse transfer function. The beamform stacked inverted acoustic wave at the bottom of Figure 5d is in very good agreement with the vertical component of the seismogram recorded at VNDA, ~180 km from the center of the array, delayed by the calculated travel time from the ground to ionospheric altitudes. To better compare the agreement of the seismogram and the estimated acoustic wave signature obtained from TEC observations, we applied a small time offset necessary to better align these two traces, since the raytracing provides an arrival time that is accurate only within a few minutes. The synthetic TEC and the Rayleigh wave seismogram were scaled to match the TEC data and the amplitude of the stacked acoustic wave, respectively, because we have not modeled the coupling between the solid earth and the atmosphere, necessary to obtain the correct amplitudes.

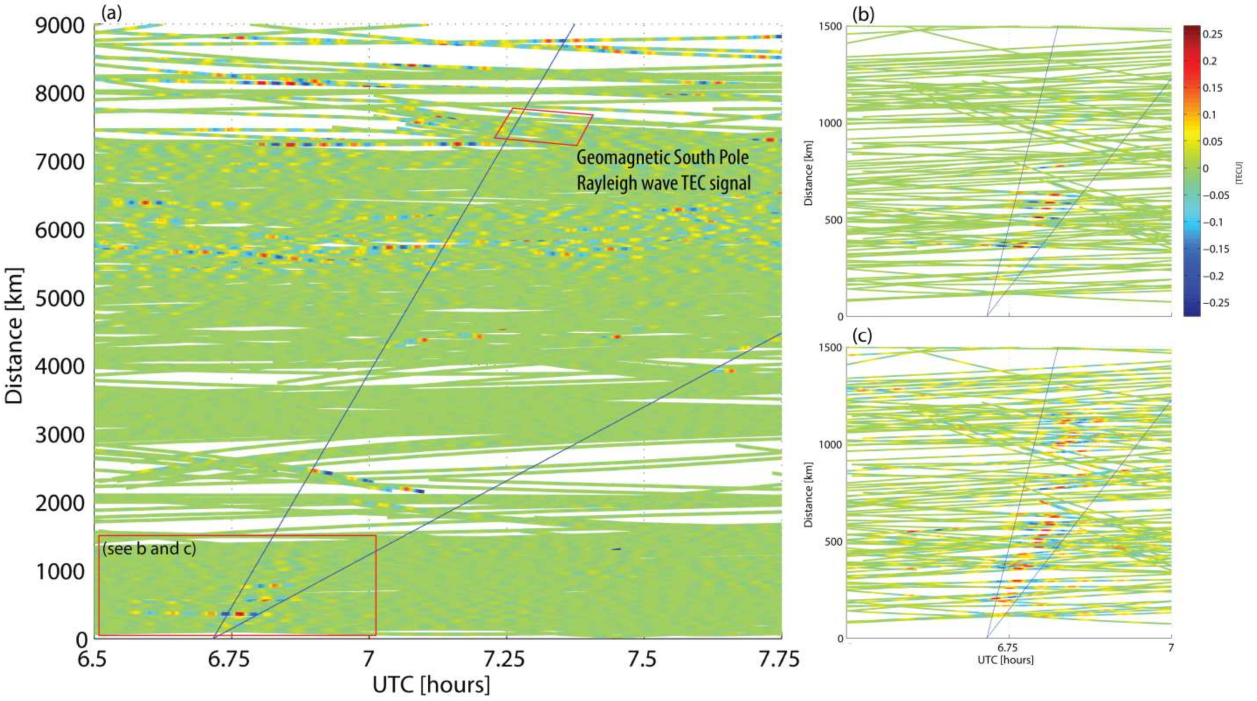

Figure 6. Traditional time-distance diagram of TEC. (a) for GPS stations between the epicentral region of the Maule earthquake and the McMurdo region in Antarctica. The Rayleigh wave-induced TEC signal from the Maule earthquake, processed in the beamform analysis, can be observed in Antarctica in the distance range 7200 to 7800 km (top red polygon). Due to the low number of GPS stations in southern South America and Antarctica, all GPS stations-satellite pairs are shown in the time-distance diagram. The steep blue line shows the Rayleigh wave propagation from the epicentral area (slope = 4 km/s). The shallower blue line shows the N-shaped acoustic wave (slope = 1 km/s). We applied a delay of ~10 minutes to the origin times of the blue lines to account for the travel time from the ground to the ionosphere. The earthquake origin time is ~6.5 UTC. To enhance visibility of the far-field signals, we only plotted TEC traces with both high SNR and absolute amplitudes < ~0.25 TECU on which the Rayleigh wave-induced TEC signals are observable. The data in the lower red box is shown in (b) and (c). (b): Zoom in showing the acoustic wave-induced TEC signals in the near-field. Blue lines as in (a). Because only TEC traces with amplitudes < ~0.25 TECU were ploted, the signals are less visible beyond ~800 km. (c): View of the TEC signals shown in (b), enhanced using an automatic gain control algorithm . This plot shows absolute amplitude differences from -1 (blue) to 1 (red).

The proximity of the Antarctic region to the epicentral area of the Maule earthquake allowed us to compare our results with those obtained by the traditional time-distance diagram. Figure 6a shows that the Rayleigh wave-induced ionospheric signal can also be identified from this diagram. This plot was generated using only TEC traces with high SNR, on which the Rayleigh wave-induced TEC signal is observable. Some induced signals in the near-field can also be observed at ~600 km from the epicentral area (lower red box). These near-field TEC signals are also shown in Figures 6b and c. While low SNR signals are visible in the time-distance plots, the information that can be obtained from them is less than that obtained from the virtual array. We examined other ANET virtual arrays that are farther away from the geomagnetic pole, but the presence of Rayleigh wave-induced TEC signals was less certain. We suggest that this can be explained by a geomagnetic field inclination > 10º at the location of the arrays, which significantly reduces the coupling between the acoustic wave and the ionospheric plasma.

Virtual Beamforming the Tohoku-Oki earthquake TEC signals in Antarctica

We performed the same procedure with TEC observations using satellite PRN25 for the arrival time window of Rayleigh waves from the Mw 9.0 Tohoku-Oki earthquake, (location 38.297°N, 142.372°E, depth 30 km on 11/03/2011 at 05:45:24 UTC). Figure 7a and b show results similar to those from the Maule earthquake.

For the Tohoku-Oki earthquake, we have estimated a back azimuth of ~350°, equal to the great circle back azimuth, and an apparent velocity of ~3.5 km/s (slowness of ~0.28 s/km). Although we assumed a Rayleigh wave phase velocity of ~4 km/s, our beamformed apparent velocity is within the observed Rayleigh wave velocity range found in previous studies [e.g. *Artru et al.*, 2001; *Rolland et al.*, 2011]. We also note that the location of both virtual arrays (Maule and Tohoku-Oki) is close together, as shown by Figure 7c, which suggests that a geomagnetic field inclination of less that ~10° favors the observation of this phenomenon.

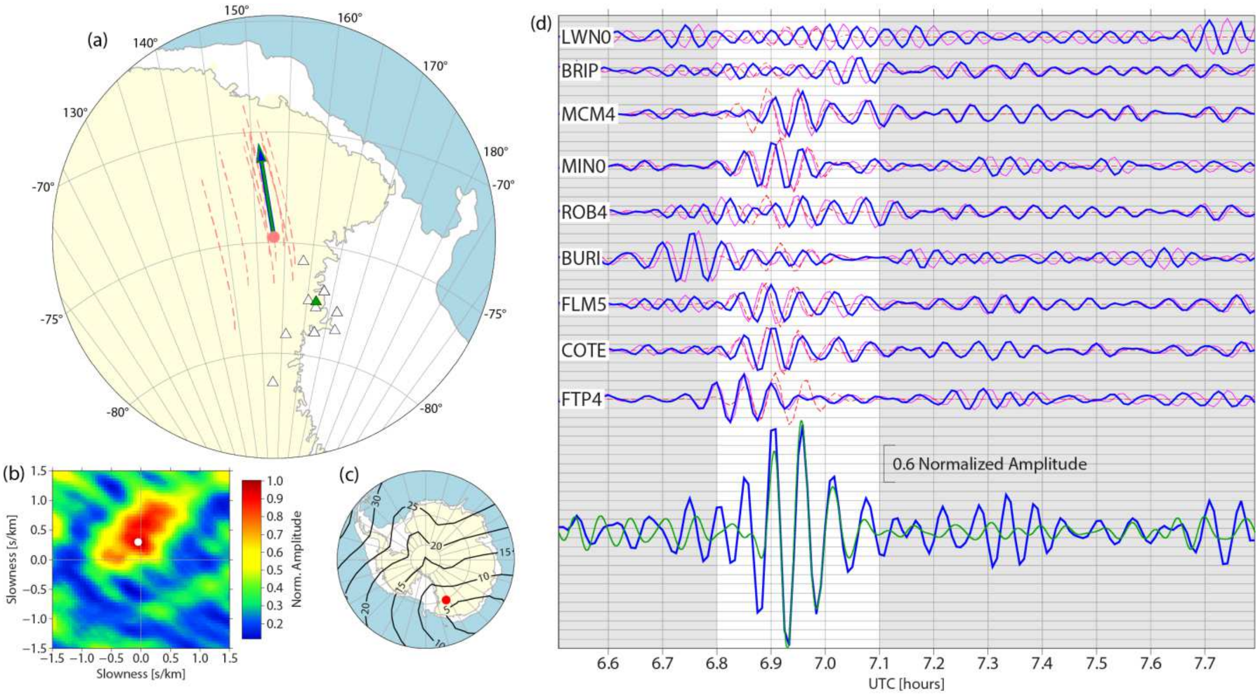

Figure 7. Results for virtual array beamform of CIDs produced by the Tohoku-Oki earthquake. Symbols as in Figure 5. (a): Location map. Back azimuths; to epicenter –green ~350°, estimated using beamforming –blue ~350°. (b): Beamform stacking slowness (speed, ~3.5 km/s). (c): inclination of the geomagnetic field lines (~6°). (d): Same as in Figure 5.

On Figure 7b, we note a "smeared" beamform response plot, which suggests the existence of a second TEC signal occurring within the time window of the TEC time series used for beamforming. Assuming the presence of a second TEC signal in the ionosphere, applying the inverse transfer function using the Tohoku-Oki test source could result in partial constructive interference. Secondary signals can be observed in the time series for stations BURI, FTP4 and LWN0 in Figure 7d, where wave packets outside the Rayleigh wave time window (gray section of the plot) can be seen. Nevertheless, coherent stacking among the nine elements of the virtual array beamform allowed us to distinguish the Rayleigh wave-induced acoustic wave from other signals and noise.

We also compared the amplitudes of the TEC response for Tohoku-Oki and Maule using the raw TEC data of GPS station COTE. We note that the amplitude at COTE of the Tohoku-Oki signal is about 4.6 times larger than that for Maule (Figure 8a), while the seismic displacement amplitude ratio is only a factor of three (Figure 8b). Assuming that the ratio of the acoustic wave is linearly proportional to the vertical amplitude of the Rayleigh waves, and multiplying this ratio by the TEC response ratio obtained from the G&H model (Figure 8c), we estimated a TEC ratio of ~5.1 (Figure 8d), which is roughly in agreement with the observed TEC ratio.

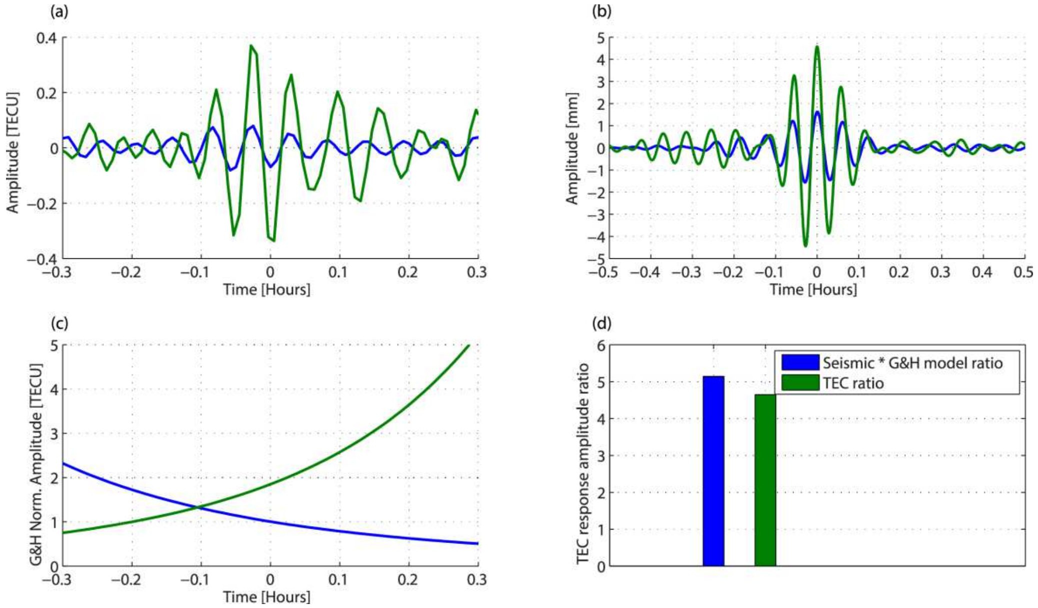

Figure 8. Amplitude comparison of the TEC response of the Maule and Tohoku-Oki earthquakes for two IPPs for the GPS station COTE. (a): TEC signals of the Maule (blue) and the Tohoku-Oki earthquakes (green). Time shifts were applied to place the Rayleigh wave-induced TEC signal at ~0 hours. The peak to peak TEC amplitude of the Tohoku-Oki earthquake is 4.6 times larger than that of Maule. (b): Amplitude comparison of the band passed and time shifted Rayleigh wave vertical component at seismic station VNDA for the Maule (blue) and the Tohoku-Oki (green) earthquakes. The peak to peak seismic amplitude shows that the Rayleigh wave from Tohoku-Oki is 3 times larger than that of Maule. (c): Transfer function amplitude scaled to the response of the Maule earthquake, which shows that the TEC response for the Tohoku-Oki earthquake is ~1.8 times larger than that for Maule. (d): Estimated response ratio using the seismic amplitude ratio times the transfer function ratio, which yields 5.1.

Conclusion

We have introduced a new approach, virtual array beamforming, for analyzing ionospheric TEC waves. This method allowed us to estimate the speed and back azimuth of seismically induced acoustic waves at the virtual array by amplifying the signals through coherent stacking. To recover the Rayleigh wave-induced acoustic waves from TEC observations, we used an inverse transfer function obtained from the G&H model. Our results strongly argue that the signals we observed in the ionosphere around the Geomagnetic South Pole were produced by the Maule and the Tohoku-Oki earthquakes.

We propose that the detection of CIDs in the region of the Geomagnetic South Pole is enhanced by two effects, the increase in sensitivity with lowering of the GPS LOS elevation, and the enhanced generation of CIDs due the sub parallel alignment of the geomagnetic field lines near the Geomagnetic Poles with the propagation direction of the acoustic wave. Although a high level of noise in the Antarctic ionosphere poses some difficulties for observing low SNR signals, by using virtual array beamforming we have observed Rayleigh wave-induced acoustic waves from events that are ~7,500 km and ~12,500 km distant. To our knowledge, this is the farthest observation of this phenomenon using GPS technology.

The amplitude of the TEC response for Tohoku-Oki is about 4.6 times larger than that for Maule. Although we cannot perform a direct comparison of the ionospheric response of each earthquake without the appropriate solid earth-atmosphere coupling, as in *Rolland et al.* [2011], we approximate the TEC ratio by assuming that the ratio of the acoustic waves is linearly proportional to the vertical amplitude of the Rayleigh waves. Multiplying this ratio by the TEC response ratio obtained from the G&H model, we estimated a TEC ratio of ~5.1, which is roughly in agreement with the observed TEC ratio.

Evidence supporting teleseismic Rayleigh wave-induced acoustic wave observations at very large distances can be found in *Occhipinti et al.* [2010], who showed that the R2 signal produced by the 2005 (Mw 8.6) Sumatra earthquake could be detected in the ionosphere using an over-the-horizon (OTH) radar and Doppler sounder observations. Their findings suggest that, if a lower magnitude earthquake R2 Rayleigh wave induces a TEC signal, R1 of the Maule and Tohoku-Oki earthquakes will also induce a TEC signal at large distances from the epicenter. Because of the appropriate observational conditions, these signals can be recorded using GPS in Antarctica.

Another important factor for observing seismogenic TEC signals is the magnitude of the earthquake producing them. We also analyzed data from the Mw 8.2 Pisagua earthquake (location at 19.642°S, 70.817°W depth of 20.1 km on 01/04/2014 at 23:46:47 UTC). Although our results suggest the presence of Rayleigh wave-induced TEC signals near the Geomagnetic South Pole, the beamformed signal has a very low SNR that reduces our confidence in the results. However, this result and results from *Occhipinti et al.* [2010] suggest that earthquakes smaller than Mw 8.8 will generate signals near the Geomagnetic Poles that may be visible with GPS. Further modeling and the inclusion of solid earth-atmosphere coupling will help to better understand this observed polar phenomenon.

Acknowledgements

This work was supported by National Science Foundation POLENET grants PLR0632339, PLR1247518 and PLR0948103 (Gómez and Smalley), ANT-0632322 and PLR-1249631 (Wilson, Bevis, Konfal, Willis and Caccamise), and ANT-06332330 and PLR-1249513 (Dalziel) and the Center for Earthquake Research and Information, The University of Memphis

(Langston). The authors would like to thank Giovanni Occhipinti and an anonymous reviewer for their insightful comments and suggestions that have contributed to improve this paper.

Data Sources

This material is based on data services provided by the UNAVCO Facility with support from the National Science Foundation (NSF) and National Aeronautics and Space Administration (NASA) under NSF Cooperative Agreement No. EAR-0735156. http://www.unavco.org/

Data for the Maule earthquake used to produce the time-distance diagram was obtained from the *Red Argentina de Monitoreo Satelital Continuo* (RAMSAC), Instituto Geográfico Nacional, Argentina. http://www.ign.gob.ar/NuestrasActividades/Geodesia/Ramsac

The International Geomagnetic Reference Field (IGRF) was obtained from the International Association of Geomagnetism and Aeronomy, Working Group V-MOD. doi: 10.1111/j.1365-246X.2010.04804.x

An empirical model of the Earth's horizontal wind fields: HWM07 was downloaded from http://nssdcftp.gsfc.nasa.gov/models/atmospheric/hwm07/

The NRL-MSISE-00 Empirical Model of the Atmosphere was downloaded from: ftp://hanna.ccmc.gsfc.nasa.gov/pub/modelweb/

The International Reference Ionosphere 2012 was downloaded from: http://iri.gsfc.nasa.gov/. doi:10.1051/swsc/2014004

References

Afraimovich, E. L., E. A. Kosogorov, N. P. Perevalova, and A. V. Plotnikov (2001), The use of GPS arrays in detecting shock-acoustic waves generated during rocket launchings, *J. Atmospheric Sol.-Terr. Phys.*, *63*(18), 1941–1957.

Artru, J., P. Lognonné, and E. Blanc (2001), Normal modes modelling of post-seismic ionospheric oscillations, *Geophys. Res. Lett.*, *28*(4), 697–700.

Artru, J., T. Farges, and P. Lognonné (2004), Acoustic waves generated from seismic surface waves: propagation properties determined from Doppler sounding observations and normal-mode modelling: Propagation of seismic acoustic waves, *Geophys. J. Int.*, *158*(3), 1067–1077, doi:10.1111/j.1365-246X.2004.02377.x.

Artru, J., V. Ducic, H. Kanamori, P. Lognonné, and M. Murakami (2005), Ionospheric detection of gravity waves induced by tsunamis, *Geophys. J. Int.*, *160*(3), 840–848, doi:10.1111/j.1365-246X.2005.02552.x.

Astafyeva, E., K. Heki, V. Kiryushkin, E. Afraimovich, and S. Shalimov (2009), Two-mode long-distance propagation of coseismic ionosphere disturbances, *J. Geophys. Res.*, *114*(A10), doi:10.1029/2008JA013853.

Astafyeva, E. I., and E. L. Afraimovich (2006), Long-distance traveling ionospheric disturbances caused by the great Sumatra-Andaman earthquake on 26 December 2004, *Earth Planets Space*, *58*(8), 1025.

Bilitza, D., D. Altadill, Y. Zhang, C. Mertens, V. Truhlik, P. Richards, L.-A. McKinnell, and B. Reinisch (2014), The International Reference Ionosphere 2012 – a model of international collaboration, *J. Space Weather Space Clim.*, *4*, A07, doi:10.1051/swsc/2014004.

Calais, E., and J. B. Minster (1995), GPS detection of ionospheric perturbations following the January 17, 1994, Northridge Earthquake, *Geophys. Res. Lett.*, *22*(9), 1045–1048, doi:10.1029/95GL00168.

Calais, E., and J. B. Minster (1998), GPS, earthquakes, the ionosphere, and the Space Shuttle, *Phys. Earth Planet. Inter.*, *105*(3), 167–181.

Calais, E., J. S. Haase, and J. B. Minster (2003), Detection of ionospheric perturbations using a dense GPS array in Southern California, *Geophys. Res. Lett.*, *30*(12), doi:10.1029/2003GL017708.

Dautermann, T., E. Calais, and G. S. Mattioli (2009), Global Positioning System detection and energy estimation of the ionospheric wave caused by the 13 July 2003 explosion of the Soufrière Hills Volcano, Montserrat, *J. Geophys. Res.*, *114*(B2), doi:10.1029/2008JB005722.

Drob, D. P. et al. (2008), An empirical model of the Earth’s horizontal wind fields: HWM07, *J. Geophys. Res.*, *113*(A12), doi:10.1029/2008JA013668.

Fitzgerald, T. J. (1997), Observations of total electron content perturbations on GPS signals caused by a ground level explosion, *J. Atmospheric Sol.-Terr. Phys.*, *59*(7), 829–834.

Galvan, D. A., A. Komjathy, M. P. Hickey, P. Stephens, J. Snively, Y. Tony Song, M. D. Butala, and A. J. Mannucci (2012), Ionospheric signatures of Tohoku-Oki tsunami of March 11, 2011: Model comparisons near the epicenter: TSUNAMI IONOSPHERIC SIGNATURES NEAR EPICENTER, *Radio Sci.*, *47*(4), n/a–n/a, doi:10.1029/2012RS005023.

Garcés, M. A., R. A. Hansen, and K. G. Lindquist (1998), Traveltimes for infrasonic waves propagating in a stratified atmosphere, *Geophys. J. Int.*, *135*(1), 255–263.

Georges, T. M. (1968), Collisional interaction of atmospheric waves with the ionospheric F region, in *Acoustic-Gravity Waves in the Atmosphere*, vol. 1, p. 377.

Georges, T. M., and W. H. Hooke (1970), Wave-Induced Fluctuations in Ionospheric Electron Content: A Model Indicating some Observational Biases, *J. Geophys. Res. Space Phys.*, *75*(31).

Heki, K., and J. Ping (2005), Directivity and apparent velocity of the coseismic ionospheric disturbances observed with a dense GPS array, *Earth Planet. Sci. Lett.*, *236*(3-4), 845–855, doi:10.1016/j.epsl.2005.06.010.

Hooke, W. H. (1968), Ionospheric irregularities produced by internal atmospheric gravity waves, *J. Atmospheric Terr. Phys.*, *30*(5), 795–823, doi:10.1016/S0021-9169(68)80033-9.

Hunsucker, R. D., and J. K. Hargreaves (2002), *The high-latitude ionosphere and its effects on radio propagation*, Cambridge University Press.

Lognonné, P., E. Clévédé, and H. Kanamori (1998), Computation of seismograms and atmospheric oscillations by normal-mode summation for a spherical earth model with realistic atmosphere, *Geophys. J. Int.*, *135*(2), 388–406.

Lognonné, P., R. Garcia, F. Crespon, G. Occhipinti, A. Kherani, and J. Artru-Lambin (2006), Seismic waves in the ionosphere, *Europhys. News*, *37*(4), 11–15.

Mannucci, A. J., B. D. Wilson, and C. D. Edwards (1993), A new method for monitoring the Earth's ionospheric total electron content using the GPS global network, in *Proceedings of the 6th International Technical Meeting of the Satellite Division of the Institute of Navigation (ION GPS 1993)*, pp. 1323–1332.

Occhipinti, G., P. Dorey, T. Farges, and P. Lognonné (2010), Nostradamus: The radar that wanted to be a seismometer: IONOSPHERIC SEISMOLOGY, *Geophys. Res. Lett.*, *37*(18), n/a–n/a, doi:10.1029/2010GL044009.

Occhipinti, G., L. Rolland, P. Lognonné, and S. Watada (2013), From Sumatra 2004 to Tohoku-Oki 2011: the systematic GPS detection of the ionospheric signature induced by tsunamigenic earthquakes, *J. Geophys. Res. Space Phys.*, *118*(6), 3626–3636.

Picone, J. M., A. E. Hedin, D. P. Drob, and A. C. Aikin (2002), NRLMSISE-00 empirical model of the atmosphere: Statistical comparisons and scientific issues, *J. Geophys. Res. Space Phys.*, *107*(A12), 1468, doi:10.1029/2002JA009430.

Rolland, L. M., P. Lognonné, and H. Munekane (2011), Detection and modeling of Rayleigh wave induced patterns in the ionosphere, *J. Geophys. Res.*, *116*(A5), doi:10.1029/2010JA016060.

Rost, S., and C. Thomas (2002), Array seismology: Methods and applications, *Rev. Geophys.*, *40*(3), doi:10.1029/2000RG000100.

CHAPTER 5

The lithospheric stress guide and far-field co-seismic deformation

Submitted to the Journal of Geophysical Research, Solid Earth

Introduction

The most widely used method to model co-seismic deformation is the homogeneous half-space model [*Okada*, 1985]. This method became popular during the early days of GPS due to ease of use and its ability to model sparse near-field inter- and co-seismic campaign data [*Feigl et al.*, 1993; *Massonnet et al.*, 1993; *Dong et al.*, 1998]. This method has the advantage of providing surface deformation without requiring complex modeling of the rheological properties of the rupture zone. Despite the aforementioned advantages, layered earth structure and sphericity cannot be ignored when studying megathrust earthquakes that produce co-seismic deformation fields that extend into the far-field. The influence of adding or removing sphericity, layering and gravity are already well described in previous studies [e.g., *Cattin et al.*, 1999; *Fu et al.*, 2010; *Dong et al.*, 2014] but mostly in terms of the observable surface deformation. The underlying physical mechanism that controls deformation in the far-field (> 400 km from the rupture zone) and the implications on tectonic studies are rarely discussed. While there are multiple models of the large time scale behavior of the lithosphere [*Thatcher*, 1995] and crust [*Burov and Watts*, 2006], there are fewer models that investigate the short term behavior of the lithosphere and asthenosphere that controls far-field co-seismic deformation produced by large earthquakes and the subsequent post-seismic deformation. Although some models investigate the geodetic time scale of the inter-seismic deformation field [e.g. *Lechmann et al.*, 2014], these studies aim to understand a specific tectonic environment, producing results that may be difficult to apply to other regions.

One mechanism that controls far-field deformation, and probably the most important, is the lithospheric stress guide that allows the transmission of stresses from the rupture zone. This is in line with the observations from *Pollitz* [1996] and *Dong et al.* [2014] who found that layering introduces the largest co-seismic deformation difference (~ 20%) when compared against uniform models. This result suggests the importance of layering relative to gravity and sphericity and that more work is necessary to understand the role of the lithosphere in short term tectonic processes, especially in the far-field.

Since the advent of GPS technology, co- and post-seismic far-field deformation has been observed on a wide variety of tectonic environments. Little effort, however, has been invested in understanding the implications of earthquake deformation at distances > 400 km and the dynamic role of the lithosphere in such observations. We consider that it is worth analyzing far-field deformation to properly understand the role of the short term lithospheric and asthenospheric strength during the co-seismic stage of the earthquake cycle.

This analysis is only possible where co-seismic and post-seismic deformation can be observed continuously from the near to the far-field. These conditions are met in South America, where large deformation fields (across more than 2000 km of continental lithosphere) occur on a regular basis due to megathrust earthquakes on the South American-Nazca plate boundary. Although this is not the only subduction zone with this characteristic (e.g. Cascadia), it has generated (to date) three megathrust earthquakes (Mw8+) in the last six years that released enough energy to produce detectable co-seismic signals from the Pacific to the Atlantic oceans. The conclusions of this work will therefore help to understand the deformation field after these large megathrust earthquakes.

This work discusses the concept of the lithospheric stress guide and how the layers of the earth and their rheology modify and control the observed co-seismic deformation, especially in the mid- and far-field where the half-space model does not accurately reproduce the deformation field. We examined the stress and strain fields throughout the lithosphere and upper mantle as a function of the strength of the layers. To simulate a subduction megathrust, we used a spherical model with a planar fault and the finite element method to compute the static elastic deformation produced by a finite slip patch.

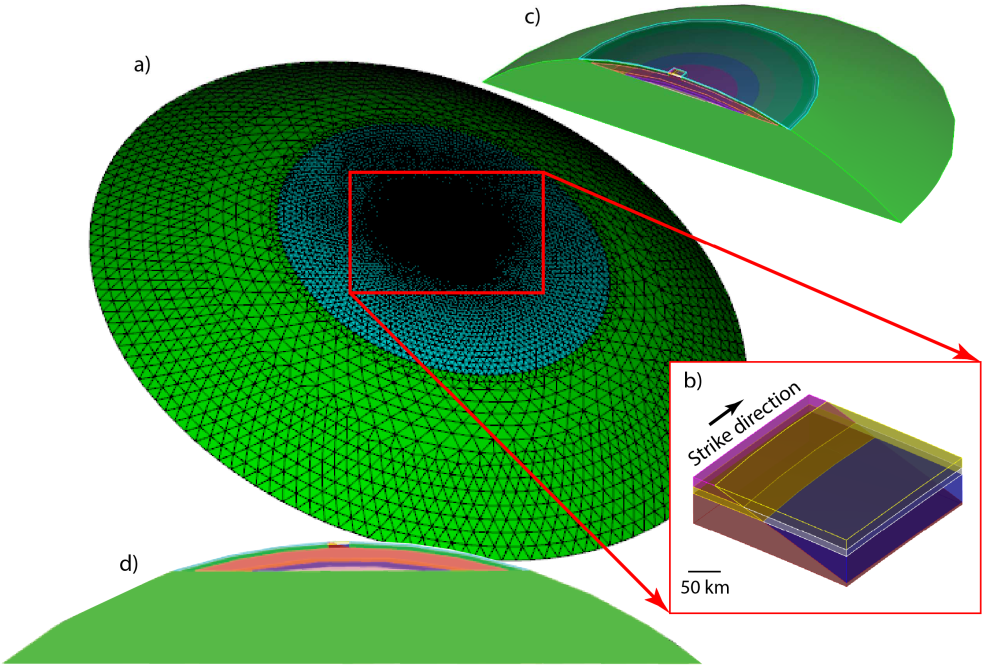

Figure 1. Finite element model schematic view. a) Spherical finite element cap showing the mesh refinement. The node spacing is ~ 2 km around the fault and increases linearly towards the edges, where the node spacing is ~ 90 km. The spherical cap has a sagitta of ~ 1300 km (chord ~ 7700 km; arc length ~ 8200 km). b) Fault geometry definition, where the cut across three layers can be observed. Colors show the different layers in the model. c) Cross section perpendicular to the strike direction. The mesh of this cross section was refined to improve the model's resolution (smallest node spacing ~ 1 km). d) 2D model obtained from the cross section in c.

Finite element model: validation against a semi-analytic solution

For this study, we used a three layered structure finite element model (FEM) on a spherical cap (Figure 1a). To facilitate post-processing, the FEM was constructed using the Earth Centered-Earth Fixed (ECEF) coordinate system. A planar fault dipping 18° (Figure 1b) was introduced at the center location of the spherical cap. To improve the resolution of the model and because in this study we are focusing on the effects along the dip direction of a thrust earthquake, we worked with a 2D model made from a vertical cross section perpendicular to the strike of the fault (Figure 1c and d). In the 2D model shown in Figure 1d, the fault is infinite in the direction perpendicular to the page and has zero stresses in that direction. This cylindrical model is appropriate to study the effects along the dip direction of the fault of a purely thrust earthquake on a spherical earth. For the 2D model, we used a discretization size (node spacing) of ~1 km, with linearly increasing spacing towards the edges. The 3D model in Figure 1a was used later in this section to validate the discretization size and problem setup (vertical direction, slip vectors, etc.) against semi-analytic solutions.

We considered three mechanically distinct layers; the crust, the lithosphere less the crust that we will simply refer to as “the lithosphere”, and the asthenosphere. The crust is from the surface to a depth of 25 km, the lithosphere is from 25 to 71 km and the asthenosphere is from 71 km to the base of the model (~ 1,300 km), with elastic properties described in Table 1. These elastic properties are the most common values assumed from models such as the Preliminary reference Earth model (PREM) [*Dziewonski and Anderson*, 1981].

Table 1. Elastic properties. Young's modulus (*E*) and shear modulus (*G*) of the three layers for our model.

Layer	***E* [GPa]**	***G* [GPa]**
Crust	68.2	26.6
Lithosphere	174.4	68.1
Asthenosphere	172.2	67.4

To validate the elastic deformation of our FEM, we first calculated the deformation using a homogeneous medium in the FEM, the semi-analytic solution of Static1d [*Pollitz*, 1996] on an homogeneous sphere, and a homogeneous half-space (hereinafter Okada as described in Okada, 1985). In the FEM component of the test, we used the 3D FEM to apply one meter of slip on a discrete fault patch composed of ~200 finite element (FE) nodes, equivalent to a square fault patch of ~20 km along strike and down dip. This fault patch size was selected to obtain a stable numerical solution given the FE discretization size. Results from this comparison showed a maximum rms difference of displacement between the FEM and Okada or Static1d of < 4% (maximum difference of ~2 mm).

We then computed the surface deformation using the FEM and Static1d for the same layered structure. We compared the results of the FEM against Static1d and found an rms difference of < 4% (maximum difference of ~3 mm), similar to the homogenous case for this pair of models. We also compared the layered FEM to the homogeneous half-space structure. The surface deformation produced by our FEM differs from the homogeneous half-space up to 21% rms (maximum difference of ~20 mm), in agreement with previous studies showing the influence of layers in co-seismic deformation [*Dong et al.*, 2014].

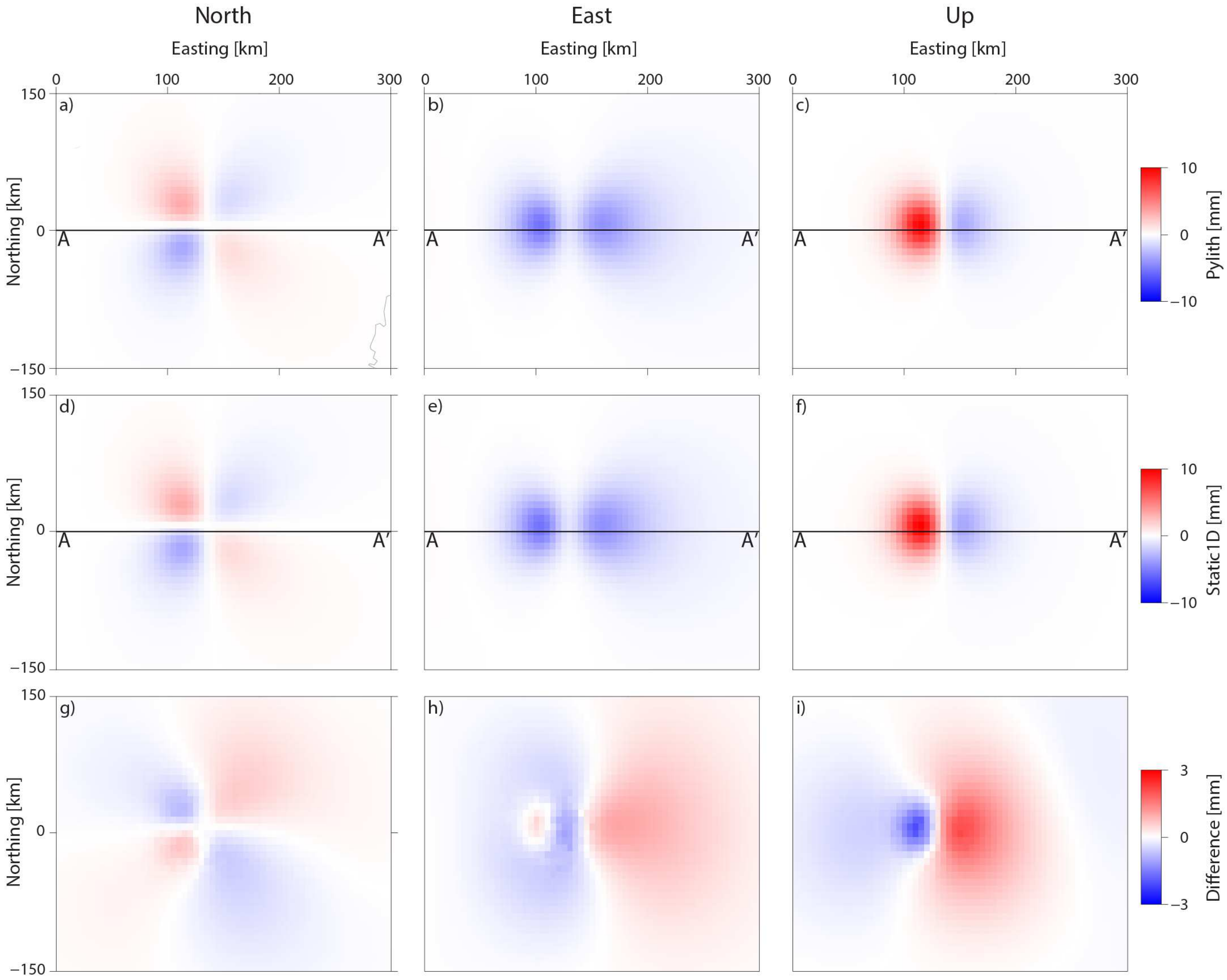

Figure 2. Comparison of surface displacements. a to c) surface displacement of the elastic spherical cap FEM; d to f) surface displacement computed using Static1d; g to i) surface displacement difference.

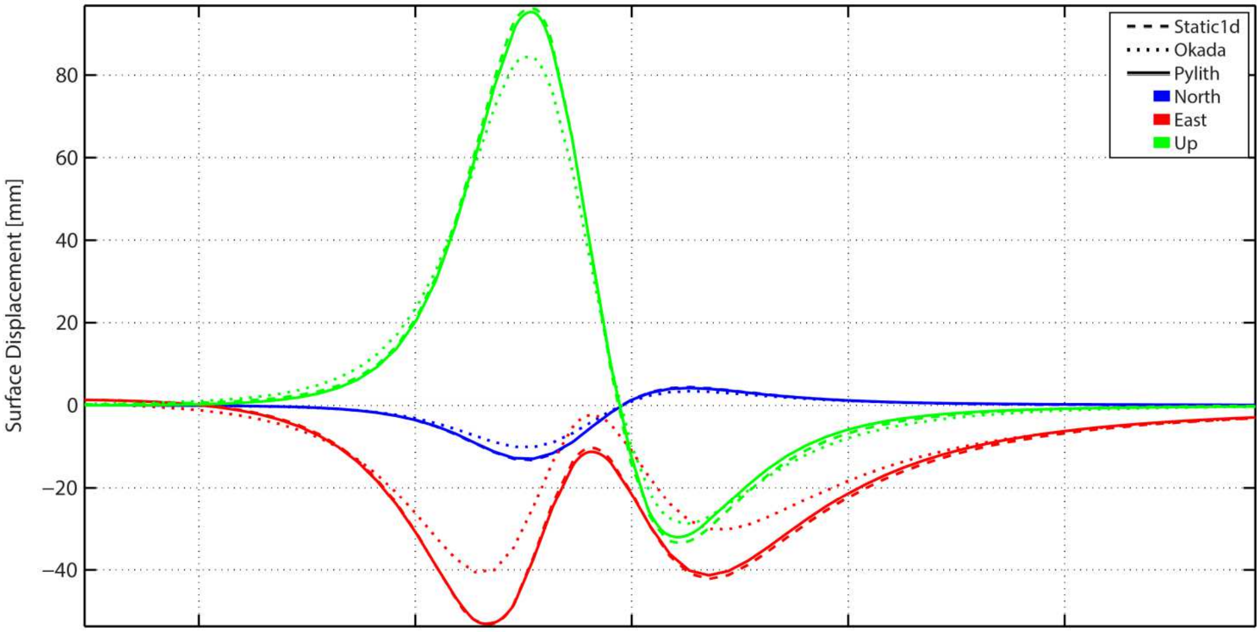

(a) A–A′ profile; RMS Pylith–Pollitz: 4%; RMS Pylith–Okada: 21 %

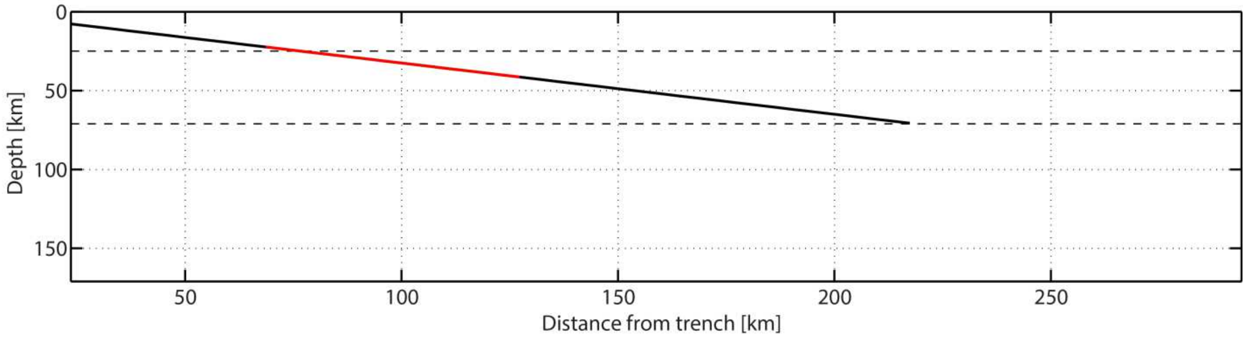

(b) Fault cross section

Figure 3. Surface displacement profiles. a) A-A’ profile of surface deformation shown in Figure 2a. b) Spatial distribution of slip in the 2D model. Horizontal black dashed lines show the layer boundaries. Black solid line shows the FE fault. Red line shows the slip distribution spanning from 22 to 42 km depth. The 2D model fault and slip distribution agrees with that used in the 3D version of the model.

Figures 2a to c show the north, east and up surface displacement computed using the finite element code Pylith [*Aagaard et al.*, 2013]. Figures 2d to f show the same using Static1d. We observe that the difference between the FE solution and Static1d never exceeds ~3 mm (Figure 2g to i), less than the error of co-seismic displacement observations estimated using GPS. In the mid- and far-field this difference is almost zero, showing that the FEM reproduces the deformation field very accurately. The profile A-A’ (Figure 3a), through the approximate center of the fault (shown in Figure 2a-f), shows the FE solution against Static1d and Okada for the three components of surface displacement. For the depth of the slip patch on the FE fault, we observed that the layered sphere produced larger surface displacements than the uniform half space. After this validation, we concluded that the discretization size of our FEM and the discretization size of the fault produce elastic deformation that is sufficiently accurate to study the lithospheric stress guide.

Problem description and setup

We applied one meter of down dip slip (between 22 and 42 km depth at a distance of ~125 km from the trench of our FE fault, Figure 3b) on our 2D model. The slip magnitude was selected to provide the centimeter-level displacements observed in the far-field regions of interest. As in the previous section, we run our FEM using both homogenous and layered elastic properties and we compared the displacement, stress and strain fields of these two models.

Before comparing models, we briefly discuss slip BCs and their implications. With slip BC, the resulting displacement field is independent of a global scaling of the material stiffness (Young’s modulus, *E*, multiplied by a constant), while the stress field scales with the stiffness. We can easily verify this statement by examining the inter-seismic velocity, *u*, for a strike slip fault in a half-space [*Weertman and Weertman*, 1964; *Savage and Burford*, 1973],

$$u = \frac{s}{\pi} \arctan\left(\frac{x}{a}\right), \tag{1}$$

where x is the perpendicular distance from the fault, a is the locking depth, and s is the velocity across the fault. We note that the velocity is a function of the dimensionless ratio $\frac{x}{a}$ but independent of the elastic constants. Although this expression uses velocity in the far-field as the BC, this is equivalent to using a displacement BC when multiplied by a time period. For an earthquake, the displacement, Δw_z, is given by [*Turcotte and Schubert*, 2014]

$$\Delta w_z = \pm \frac{\Delta w_{z0}}{2}\left[\left(1+\frac{x^2}{a^2}\right)^{1/2} - \frac{|x|}{a}\right], \tag{2}$$

where x and a are as before, Δw_{z0} represents the co-seismic displacement across the fault, i.e. the slip BC. This expression also does not depend on the elastic constants. Therefore, scaling the stiffness of the material will yield the same displacement and strain field. The stress field, however, scales with the stiffness of the medium. Finally, we can extend this behavior to a bimaterial strike slip fault (two quarter spaces stuck together), where the deformation field across the fault is asymmetric and depends on the ratio of the material properties [*Le Pichon et al.*, 2005]. If we scale the stiffness on both sides of the fault by the same factor, the displacement field will not change.

This discussion is intended to help understand the results when using models with different stiffness values, which are not immediately intuitive. The strain field is directly related to the slip BC. The stress field, however, is related to the strain field through Young's modulus. When using displacement BCs, therefore, the stress field can be treated as a dependent variable of the strain field and the stiffness, but not the other way around. This means that two layered models differing by a single fixed ratio of the stiffness of each layer, the strain field will be equal for both models, but the stress field will be scaled by the same ratio. Since an earthquake is displacement across a fault, the problem is defined with displacement BCs. If we use stress rather than displacement BC, the stress field will behave as the controlling variable between models of different stiffness.

The lithospheric stress guide

We examined how the stress, the dependent variable, is guided by the lithosphere. We perturbed a homogenous model by adding a stiff lithosphere. To follow the convention established in previous studies, we used the stiffness of the crust for our homogenous model, remembering that in this case, the displacement field is independent of the stiffness. We analyzed the effect produced by the perturbation representing the lithosphere.

Figure 4a shows a cross section of the east and vertical displacements for the layered model (hereafter LM) and homogenous model (hereafter HM). In Figure 4b we display a color contour field of the difference of the magnitudes of the displacements in Figure 4a. These values are positive when the magnitude of the LM displacements is larger than that of the HM. We observe that the LM shows a clear and consistent increase in displacement magnitude difference (Figure 4b).

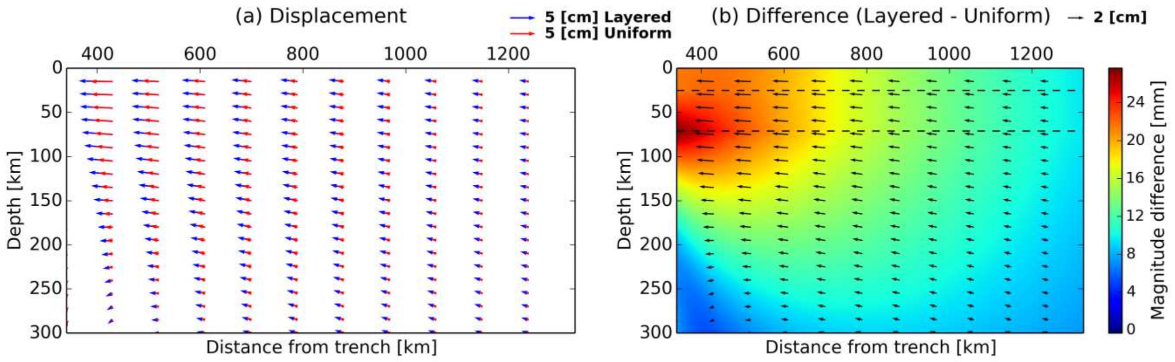

Figure 4. Displacement field cross sections. a) Displacement field cross section of layered spherical and uniform spherical model overlaid at the same scale. b) Color coded magnitude difference between layered and uniform model. Black arrows show the vector difference.

The strongest layer in the LM will concentrate the stress in that layer, which is the fundamental concept of a stress guide. This effect can be analyzed using plots showing the principal stresses as either pairs of vectors, ellipses, or as independent scalar fields. We find, however, that these types of plots are hard to interpret. To facilitate interpretation, we will work with the octahedral stress and strain [*Jaeger et al.*, 2009], and the strain energy density, since these quantities can be calculated using the stress and strain tensor invariants, which do not depend on the coordinate system being used. Before starting our analysis, we briefly justify the use of the octahedral stress and strain. We will also relate the octahedral strain to the strain energy density. To simplify the presentation, we work in the principal stress and strain coordinate system.

Consider a regular octahedron with its vertices aligned with the principal axes. Normal and shear components of stress or strain, which are vectors, act on each plane of the octahedron. The utility of the octahedral stress or strain is that the magnitude of these vectors is the same for all eight faces. The magnitude of the octahedral normal stress is

$$\sigma_{oct} = \frac{1}{3}(\sigma_{11} + \sigma_{22} + \sigma_{33}) = \frac{1}{3} I^{\sigma}{}_{1}, \tag{3}$$

where σ_{ii} are the principal stresses, $I^{\sigma}{}_{1}$ is the first invariant of the stress tensor, and $\frac{1}{3} I^{\sigma}{}_{1}$ is the pressure. The magnitude of the octahedral shear stress is

$$\tau_{oct} = \frac{1}{3}\sqrt{\left(\sigma_{11} - \sigma_{22}\right)^2 + \left(\sigma_{22} - \sigma_{33}\right)^2 + \left(\sigma_{33} - \sigma_{11}\right)^2} = \frac{1}{3}\sqrt{2 I^{\sigma}{}_{1}{}^{2} - 6 I^{\sigma}{}_{2}} = \sqrt{\frac{2}{3} J^{\sigma}{}_{2}}, \tag{4}$$

where $I^{\sigma}{}_{2}$ is the second invariant of the stress tensor, and $J^{\sigma}{}_{2}$ is the deviatoric second invariant, which is related to the stress produced by non-volumetric deformation. Accounting for both the pressure and deviatoric components, we obtain the square of the magnitude of the octahedral stress or traction vector,

$$T_{oct}{}^{2} = \sigma_{oct}{}^{2} + \tau_{oct}{}^{2}. \tag{5}$$

We can also rewrite (5) in terms of the tensor invariants as

$$T_{oct}{}^{2} = \frac{1}{3}\left[I^{\sigma}{}_{1}{}^{2} - 2 I^{\sigma}{}_{2} \right]. \tag{6}$$

We define the octahedral normal, shear and the square of the total strain using the strain tensor invariants $I^{\varepsilon}{}_{1}, I^{\varepsilon}{}_{2}$ as

$$\varepsilon_{oct} = \frac{1}{3}(\sigma_{11} + \sigma_{22} + \sigma_{33}) = \frac{1}{3} I^{\varepsilon}{}_{1}, \tag{7}$$

$$\gamma_{oct} = \frac{1}{3}\sqrt{2I^{\varepsilon}{}_{1}{}^{2} - 6I^{\varepsilon}{}_{2}} \text{ , and} \tag{8}$$

$$\varepsilon_{Toct}{}^{2} = \varepsilon_{oct}{}^{2} + \gamma_{oct}{}^{2} = \frac{1}{3}\left[I^{\varepsilon}{}_{1}{}^{2} - 2I^{\varepsilon}{}_{2} \right] \tag{9}$$

This quantity can be related to the strain energy density,

$$dU = \frac{1}{2}\sigma_{ij}\varepsilon_{ij} , \tag{10}$$

and assuming a Poisson solid $(\mu = \lambda)$ and rewriting (10) using the stress-strain relation and the tensor invariants yields

$$dU = \mu\left[\frac{3}{2} I^{\varepsilon}{}_{1}{}^{2} - 2I^{\varepsilon}{}_{2} \right]. \tag{11}$$

Notice that the octahedral stress and strain are both functions of only the stress and strain tensor invariants and the octahedral representation is therefore also an invariant. Equations (6), (9) and (11) provide invariant quantities that can be physically interpreted and reduce the stress and strain tensors to scalars that can be used to analyze the difference between models. For the two fields discussed here, stress and strain, (5) and (9) allow separating volumetric and non-volumetric deformations. The octahedral stress or traction vector can be interpreted as the total force applied on the octahedral planes, while the octahedral strain quantifies the total strain and the strain energy density of the system. We therefore calculate and plot our models' octahedral normal, shear and total stress (Figure 5) and strain (Figure 6). We will later take advantage of the similarities between (9) and (11) to use the octahedral strain to estimate the strain energy density.

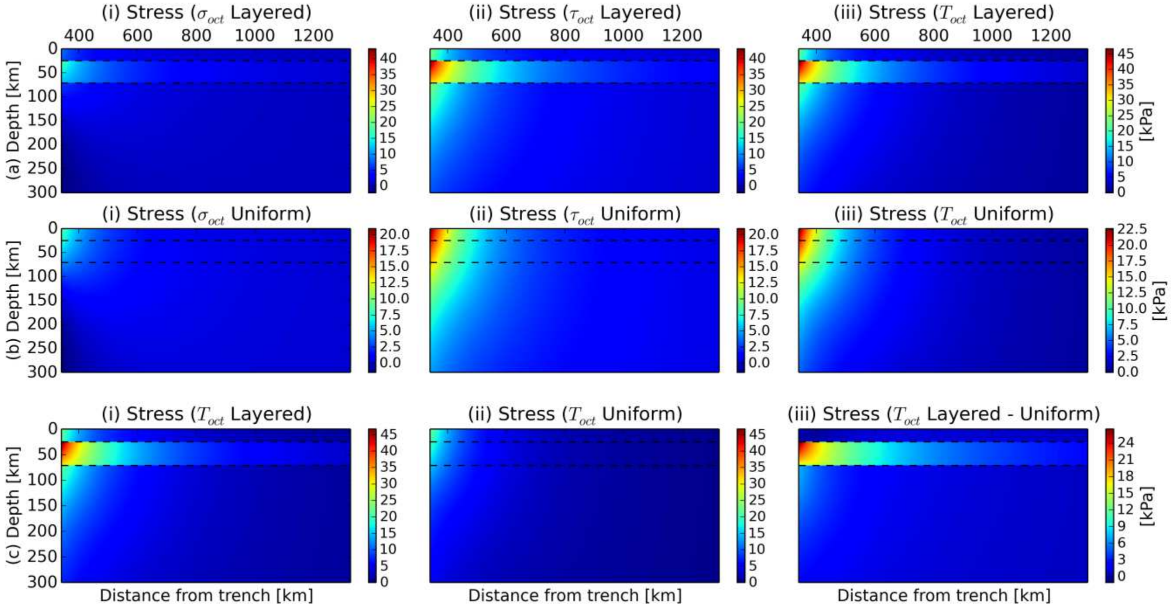

Figure 5. Stress cross sections. a) layered octahedral normal stress; b) layered octahedral shear stress; c) layered total octahedral stress; d) same as a for uniform model; e) same as b for uniform model; f) same as c for uniform model; g and h) layered and uniform total octahedral stress, respectively, shown at the same color scale; i) difference between g and h, where the lithospheric stress guide is visible.

Figure 5a-i to iii show the normal, shear and total octahedral stress fields for the LM. From Figures 5a-i and ii are plotted at the same color scale to show that the majority of the stress comes from the shear component rather than the normal component, which reveals that there is very little deformation associated with volume changes. We do the same in Figures 5b-i to iii for the HM. To compare the LM and HM, Figure 5a-iii and 5b-iii are shown with the same color scale in Figure 5c-i and Figure 5c-ii. Figure 5c-iii shows the difference between the LM and HM where the stress guiding effect is very clearly seen. The crust experiences approximately the same stress in both models, while the lithosphere experiences a peak of ~24 kPa of “extra” stress in the LM (although this value depends on the stiffness of the LM and HM). Below the lithosphere-asthenosphere boundary (LAB), we note that the stress difference drops rapidly to values < 6 kPa. It is important to note that the stress guide is visible for the LM in Figure 5c-i independent of the comparison to the HM. If we now let the stiffness of the HM be equal to the stiffness of the lithosphere in the LM, then the octahedral stress difference between the LM and HM would be zero in the lithosphere and negative in the crust and asthenosphere. The stress guide is defined, therefore, by the relative stiffness difference between the layers of the LM, not the difference with the HM.

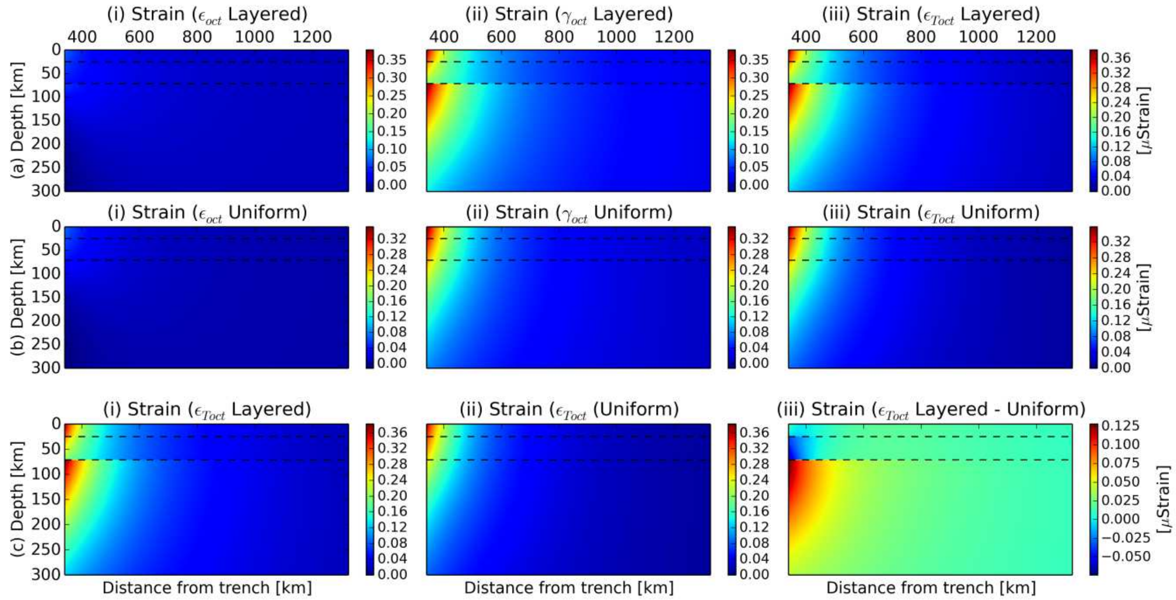

Figure 6. Strain cross sections. a) layered octahedral normal strain; b) layered octahedral shear strain; c) layered total octahedral strain; d) same as a for uniform model; e) same as b for uniform model; f) same as c for uniform model; g and h) layered and uniform total octahedral strain, respectively, shown at the same color scale; i) difference between g and h.

Figures 6a-i to iii show the octahedral strains for the LM and Figures 6b-i to iii show the same for the HM. We compute the total octahedral strain from (9), $\varepsilon_{Toct} = \sqrt{\frac{1}{3}\left[{I^{\varepsilon}_{1}}^{2} - 2I^{\varepsilon}_{2} \right]}$, shown in Figure 6a-iii and 6b-iii. Figure 6a-iii (LM) shows an octahedral strain maximum of ~0.4 μ-strain at the LAB, which is not observed in Figure 6b-iii (HM). These differences can further be examined in Figure 6c-i and ii where they are plotted using the same color scale. Figure 6c-iii shows that the majority of the strain difference is located just below the LAB. We should mention that this difference depends only on the ratios of the stiffness of the LM as the octahedral strain of the HM is independent of its stiffness due to the displacement BC.

The octahedral strain can also be used to estimate the strain energy density in the system. The term inside the brackets in (9) and (11) differ by $0.5{I^{\varepsilon}_{1}}^{2}$, however, due to the low normal octahedral strain (ε_{oct}) in both models, as can be seen graphically in Figures 6a-i and 6b-i (< 0.05 μ-strain), the maximum difference between these terms can be estimated to be $0.5{I^{\varepsilon}_{1}}^{2} = 0.5(3\varepsilon_{oct})^2 = 0.01$p-strain^2. From (7) and (8), $I^{\varepsilon}_{2} = \frac{(3\gamma_{oct})^2 - 2{I^{\varepsilon}_{1}}^{2}}{6} = 0.2$ p-strain^2, and $2I^{\varepsilon}_{2}$ is approximately 50 times larger than $0.5{I^{\varepsilon}_{1}}^{2}$. We can therefore safely compute the strain energy as $dU = \mu 3{\varepsilon_{Toct}}^{2}$.

Interpretation of displacement and strain

We will now show that the stiff lithosphere is the controlling element in the behavior of the model under displacement BC. To analyze the relationship between the LM and HM models we use displacement and strain because they are affected by relative changes, but not a global scale change, of stiffness among the layers. We don’t use stress in the comparison because changes in the stress field reflect both a combination of the change in the ratios, and a global scaling, of the stiffness. To analyze the changes in the stress field produced by a layer, a stiff lithosphere in our case, we used the strain energy density, which depends on the strain and the stiffness and is a proxy for stress. As we showed above, the strain energy density can be estimated directly using the octahedral strain.

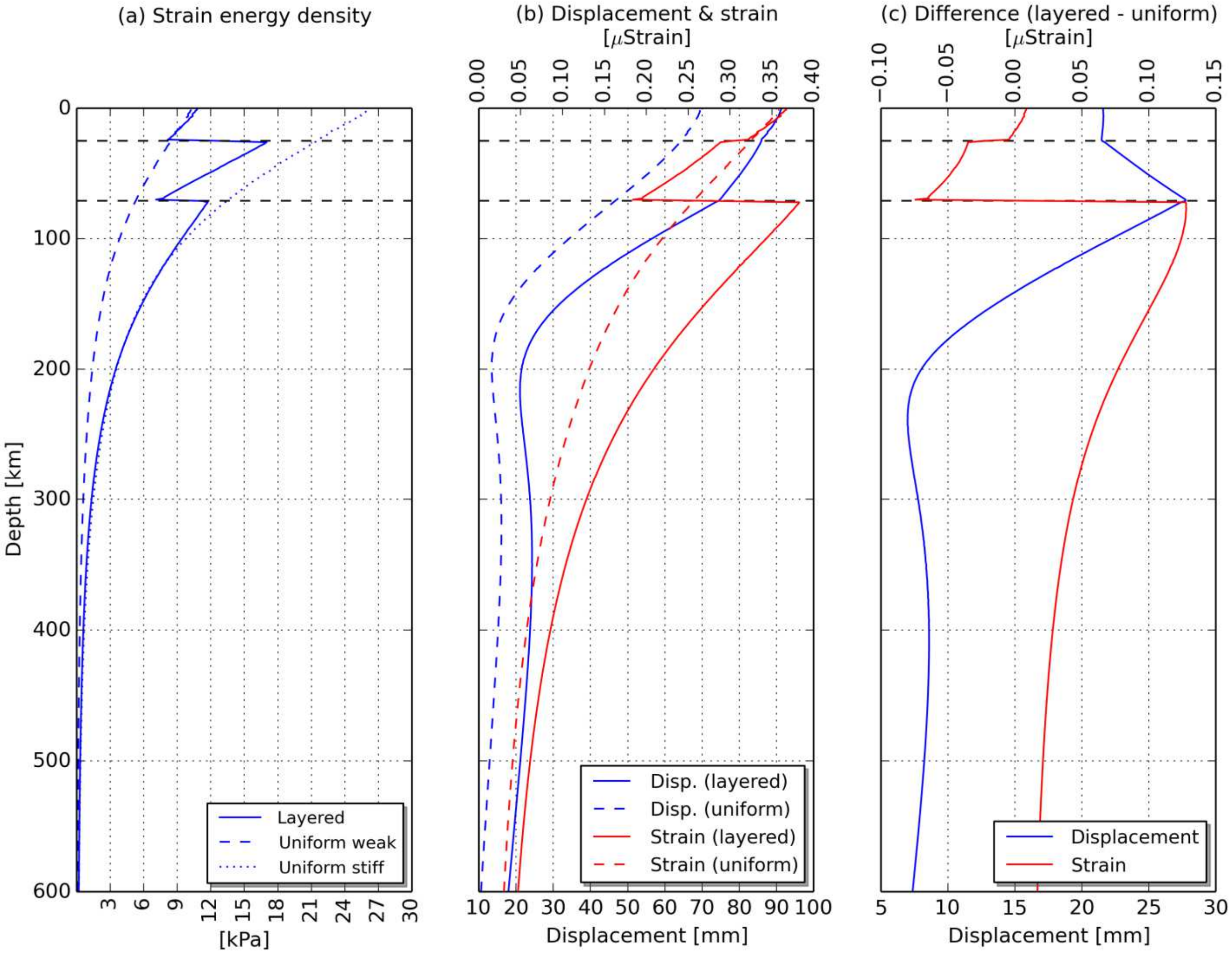

Figure 7. Depth profiles at ~400 km from the trench of a) Strain energy of the layered model (solid line), uniform model (dashed line) and a uniform model with the elastic properties of the lithosphere of the layered model (dotted line). Horizontal black dashed lines show the layer boundaries. b) Displacement (blue) and strain (red) for layered (solid line s) and uniform (dashed lines) models. c) Difference between displacement (blue) and strain (red).

We now examine the vertical distributions of the strain energy density (Figure 7a), the displacement and octahedral strain (Figure 7b), and the differences of displacement and octahedral strain (Figure 7c) at ~ 400 km from the trench. Figure 7a shows the strain energy density for the LM (solid line), the HM (dashed line) and a stiffer version of the HM which uses the stiffness of the lithosphere in the LM (stiff HM; dotted line). At this distance from the fault, the strain energy in the LM is approximately bounded by the strain energy of the HM and of the stiff HM, and the strain energy in the crust of the LM stays close to that of the HM. In the lithosphere, although the LM and the stiff HM have the same stiffness, the strain energy of the LM is significantly lower than that of the stiff HM. Interestingly, the strain energy in the asthenosphere of the LM stays very close to that of the stiff HM, although the asthenosphere has the same stiffness as the crust. These strain energy density plots will become key to understand the guiding effect later in this section.

We compared the displacement and octahedral total strain components. During this comparison we don't need to distinguish between the HM and stiff HM since displacement and strain do not depend on the stiffness due to the displacement BC. As mentioned before, we observed that the LM displacements are larger at all depths than those of the HM, while the strain is only larger below the LAB.

These differences are better shown in Figure 7c. The displacement difference increases above 220 km, having a maximum value at the LAB, where it then drops at about a constant rate up to the crustal boundary. Above 25 km depth, the displacement difference stays approximately constant up to the surface. For the strain field a similar behavior occurs up to the LAB, where there is a sudden discontinuity and the strain difference drops to negative values (LM strain < HM strain). Above the crustal boundary, the strain experiences another discontinuity with both models having approximately the same strain.

A first important observation is that the crustal layer is "carried" by the lithosphere, due to the contrast between the stiffness of the crust and lithosphere, experiencing some small strain differences observed in Figure 7c. This effect is independent of the asthenospheric stiffness and similar to what *Cattin et al.*, [1999] observed. It is easy to conclude that the larger displacement in the crust is produced by a rigid body translation and not straining, since both models experience approximately the same crustal strains.

Examining the displacement difference between LM and HM in Figure 7c, starting at 600 km and moving to the LAB the displacement difference increases up to the top of the asthenosphere due to the increasing difference in strain of the two models. Continuing upward from the top side of the LAB, the strain in the HM is larger than that in the LM and the displacement difference between the LM and the HM decreases reflecting more strain being accumulated in the HM. If the strain difference was approximately zero, then we would expect to observe the same effect as in the crust: a constant displacement difference as a function of depth.

To accommodate the larger displacement in the lithosphere of the LM compared to the HM (difference > 0, Figure 7c), the asthenosphere has to strain more than it would in the HM. The asthenospheric strain is driven by a “rigid body” displacement of the lithosphere dragging the asthenosphere along, although the lithosphere as a whole is not translating as a rigid body (therefore the quotation marks around the words rigid body). This effect will be further discussed below when comparing models with increasing asthenospheric stiffness.

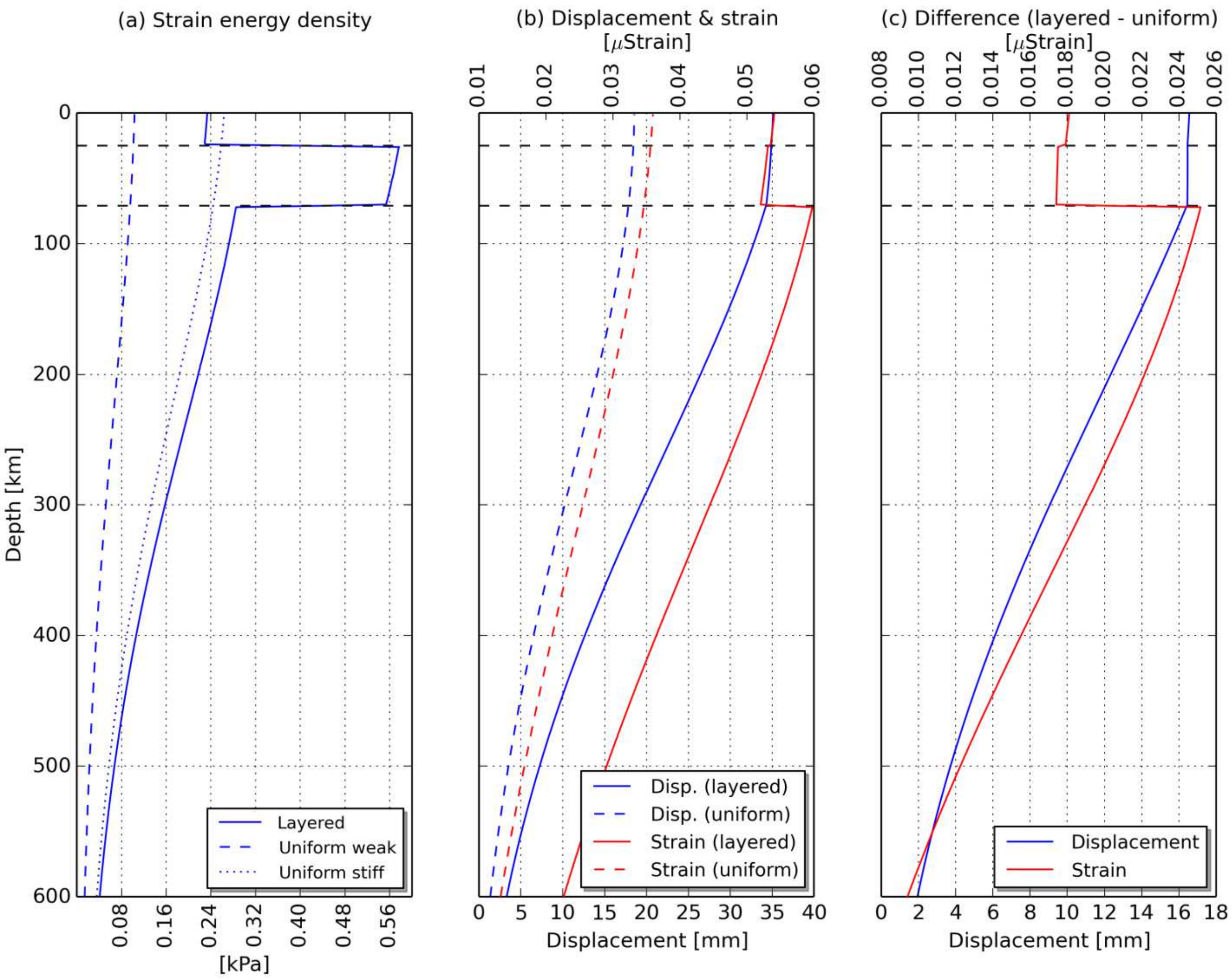

Figure 8. Depth profiles at ~800 km from the fault. Same as Figure 7.

The lithosphere experiences less deformation because it is stiffer than the rest of the model, while the weak asthenosphere strains to allow the lithosphere to approximately move as a block carrying the crust with it. The weak asthenosphere effectively decouples the lithosphere from the rest of the model. The stress guide effect in the lithosphere channels more strain energy (related to the stress increase in the layer) and more displacement, but less strain in that layer. While the maximum of the strain energy density is at the top of the lithosphere at 400 km from the trench, there is also a secondary maximum in the asthenosphere at the LAB, where the strain energy density is greater than that at the base of the lithosphere. This secondary maximum makes the stress guide less noticeable at this distance from the trench.

Doing the same analysis at ~ 800 km from the trench (Figures 8a to c), Figure 8a shows a very clear concentration of strain energy density in the lithosphere. Figure 8c shows a slower decrease in the strain field with depth at 800 km from the trench, which results in a wider strain field there, than seen in Figure 7c. At the LAB, we again observe a discontinuity in the strain field. Above 71 km depth the strain difference is slightly positive but very close to zero, which results in an approximately constant displacement difference in the lithosphere and asthenosphere. This is similar to what we observed in the crust in Figure 7c.

The effect of the asthenospheric stiffness

We increased the stiffness of the asthenosphere to produce three additional models and study their displacement difference, strain energy density and strain. We gradually increased the stiffness of the asthenosphere of the LM by multiplying E by ~ 1.5, 2 and 2.5 while keeping the same crust and lithosphere. When comparing strain energy, we also show the weak (equal to the crustal stiffness) and stiff (equal to the greatest asthenospheric stiffness) HM.

We observe that a stiffer asthenosphere produced a reduction in the rigid body displacement above the LAB from the displacement difference profiles at 400 km from the trench (Figure 9a). This was revealed by the approximately constant shape of the displacement differences, offset by ~ 20 mm (blue – green lines), 7 mm (green – red lines) and 6 mm (red – cyan lines). The cyan line represents the limit case model, where we make the asthenosphere as stiff as the lithosphere, which is equivalent to a half space with a weak layer on top [see *Cattin et al.*, 1999].

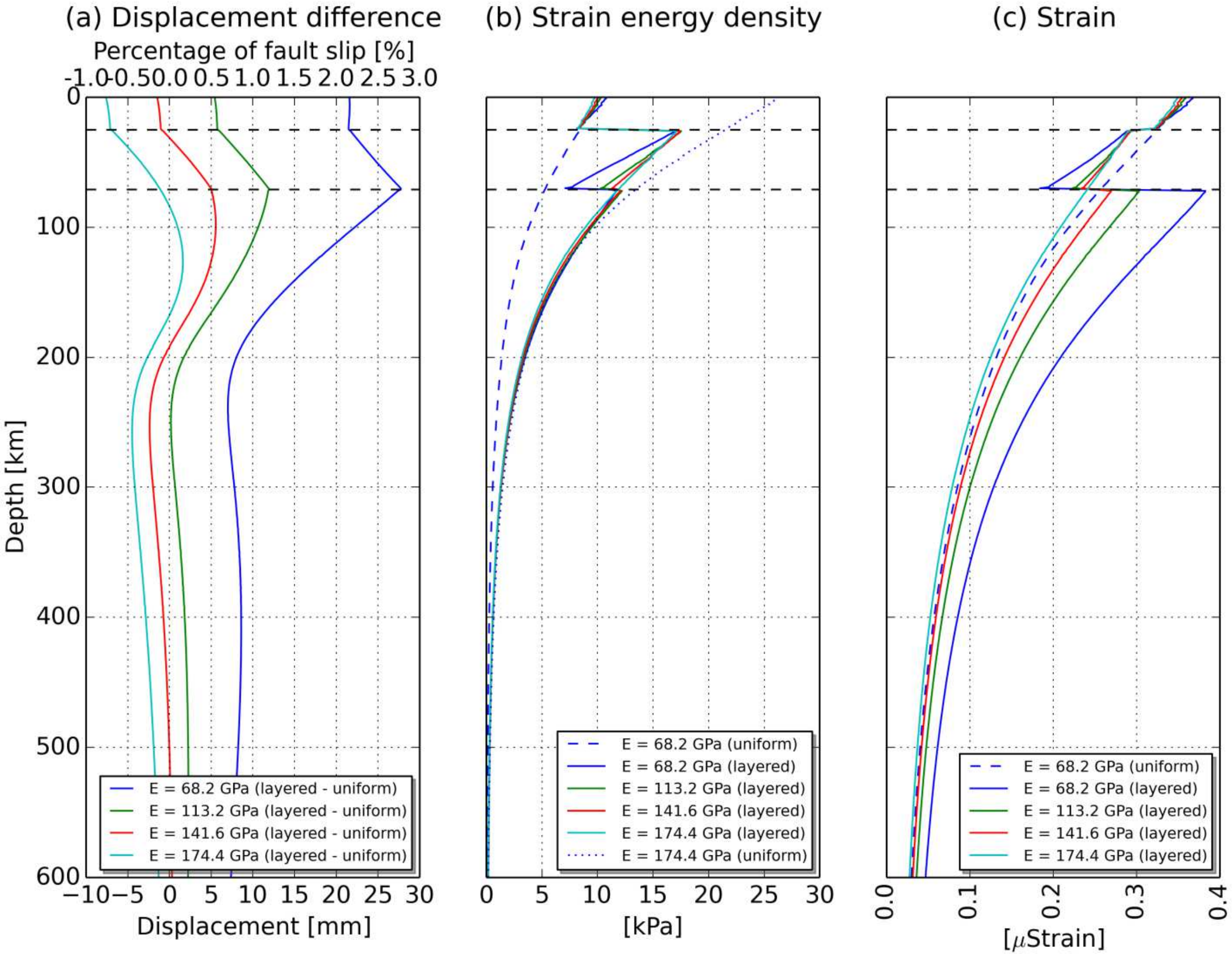

Figure 9. Displacement difference, strain energy and strain as a function of asthenospheric stiffness at ~400 km from the trench. a) Displacement difference between LM and UM with increasing asthenospheric stiffness. Top horizontal axis shows the displacement difference as percentage of slip at the fault. b) Strain energy density. We show the weak (blue dashed line) and stiff (blue dotted line) UM. c) Octahedral total strain for increasing asthenospheric stiffness.

The strain energy density profiles are bounded by the strain energy density of the weak and stiff HM (Figure 9b). Changing the asthenospheric stiffness does not considerably affect the amount of strain energy density in the asthenosphere but rather tends to increase the strain energy in the lower lithosphere. This increase is a result of the asthenosphere becoming stiffer and, therefore, the lower lithosphere requires more strain energy to satisfy the displacement boundary condition. In other words, the lithosphere requires more strain energy to “drag” the asthenosphere. The strain energy in the upper lithosphere is, however, approximately constant for all models because there is no change in *E* of the crust among the models.

The strain in the asthenosphere decreases as it becomes stiffer (Figure 9c), but because the strain energy is approximately constant, this reflects an increase in stress (compatible with the increasing asthenospheric *E*). In the lower lithosphere, however, the strain increases with increasing asthenospheric *E*, as we discussed above.

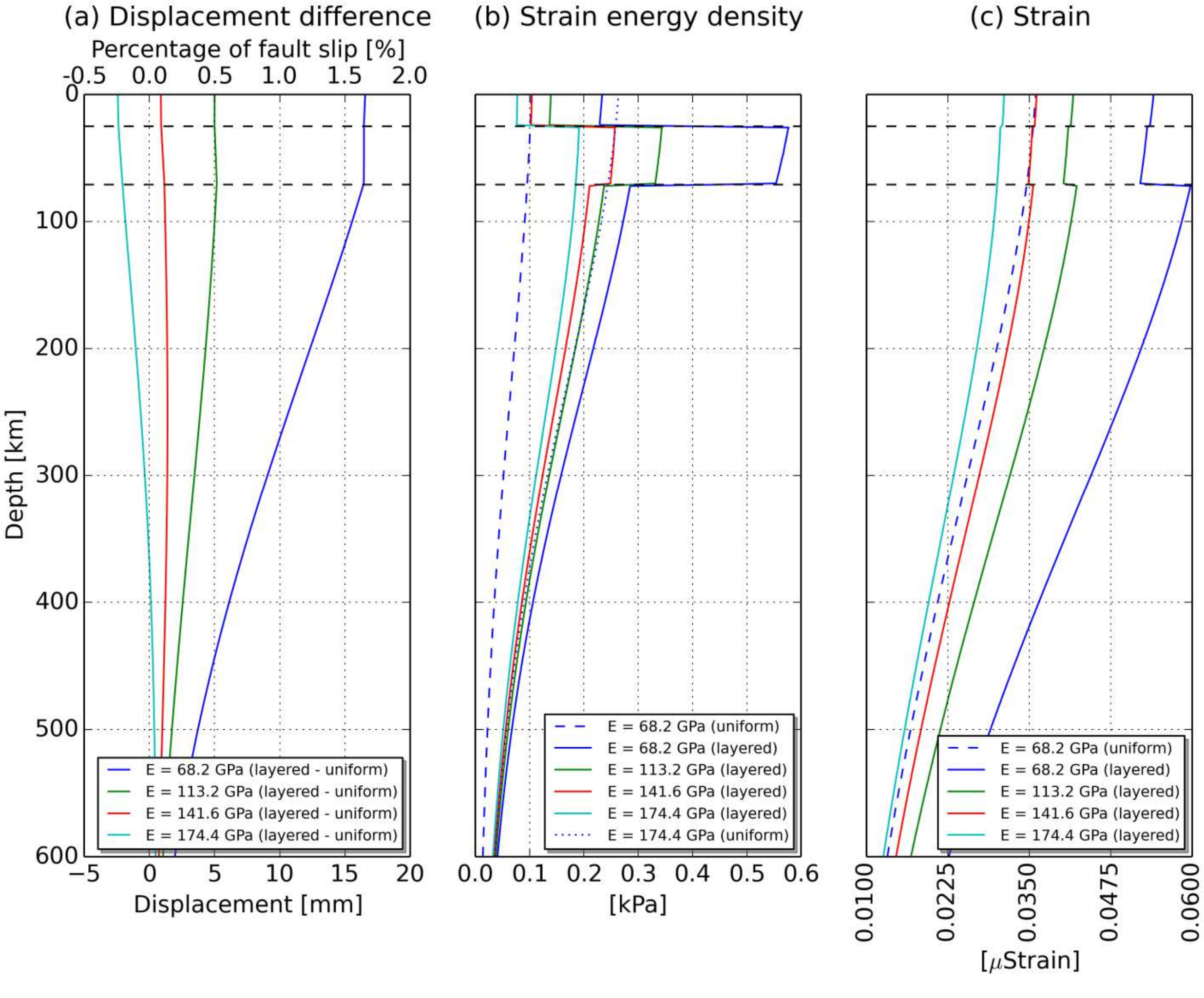

Figure 10. Displacement difference, strain energy and strain as a function of asthenospheric stiffness at ~800 km from the trench. Same as Figure 9.

Finally, we plot the same variables at ~800 km from the fault. The displacement difference (Figure 10a) shows approximately the same behavior as that observed at 400 km. The strain energy density profiles (Figure 10b) show that for decreasing asthenospheric stiffness the strain energy in the lithosphere increases above the limit of the stiff HM. The strain energy contrast between layered and homogeneous models shows that a system with a stress guide can transmit more strain energy towards the far-field than a homogeneous system. The strain energy at 800 km is the greatest for the LM with the weakest asthenosphere. Table 2 shows, however, that the total strain energy of the system increases as a function of increasing asthenospheric *E*. This result verifies that homogenous material models tend to concentrate the strain energy around the fault, while the addition of a stiff lithosphere (with a weak asthenosphere) tends to transmit strain energy to the far-field through the stress guide.

Table 2. Strain energy. Total strain energy as a function of asthenospheric stiffness. The layered models have a weak crust (68.2 GPa) and constant lithosphere stiffness (174.4 GPa), but increasing asthenosphere stiffness, shown in the second column. We also show the integrated total strain energy for all models.

Model type	***E* [GPa]**	**Total Strain Energy [TJ/m]**
Uniform weak	68.2	89.1
Layered	68.2	163.6
Layered	113.2	166.5
Layered	141.6	167.8
Layered	174.4	169.0
Uniform stiff	174.4	226.4

Influence of the stress guide on surface displacement

We investigated the influence of the stress guide on surface displacements. We already learned that due to the rigid body displacement of the lithosphere and the contrast in *E* between the crust and the lithosphere, the crust gets carried along. This effect is, however, dependent on the depth of the slip patch producing deformation. We therefore calculate the impulse response at the surface for two nodes of our FE fault, one completely within the crust (~20 km depth) and another completely within the lithosphere (~30 km depth).

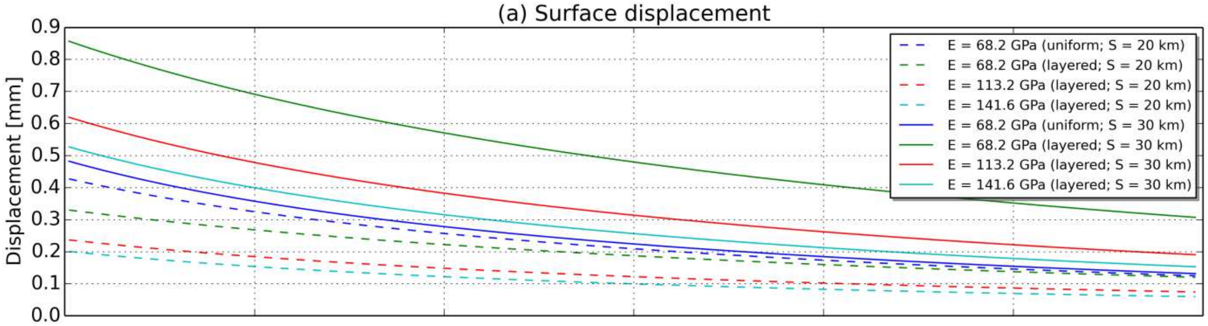
(a) Surface displacement

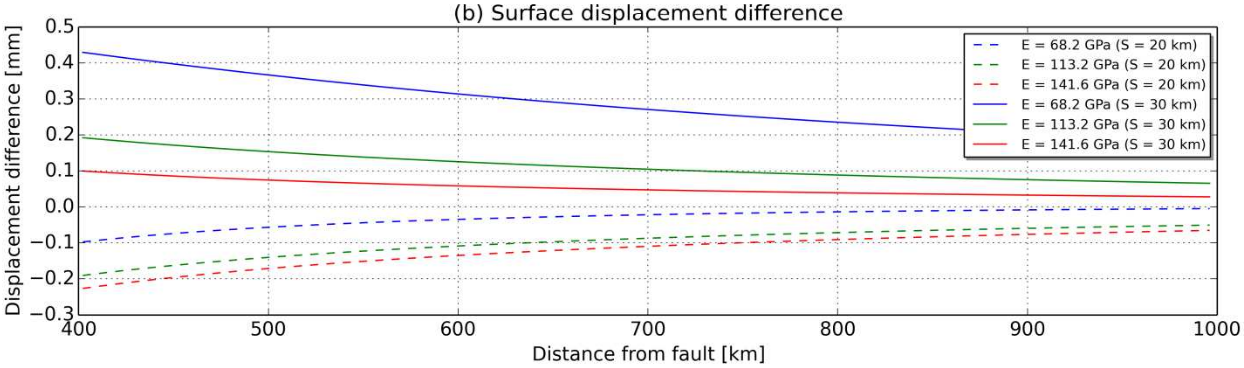
(b) Surface displacement difference

Figure 11. Surface displacement as a function of asthenospheric stiffness and depth of slip. a) Surface displacements showing all possible models, including the HM for increasing asthenospheric stiffness. b) Difference between the surface displacement of the LM and the HM.

Figure 11a shows the surface displacement as a function of distance from the trench for the shallow source (dashed lines) and the deep source (solid lines). For the HM, we note that the deeper source presents a slightly higher response at the surface. This effect is mainly due to the geometry of the fault, since a deep source on a fault dipping 18° is closer to the far-field than a shallow source. For the purposes of this comparison, and because we analyze displacement differences with respect to a reference model (HM), this effect can be ignored.

As expected from our previous analysis, for the LM the largest response is that of a source within the lithosphere coupled with a weak asthenosphere. For a crustal source, we note that the stress guide tends to decrease the LM response with respect to the HM. We analyze these differences in Figure 11b, where we show the difference between all LMs and HM. From this, we conclude that for the LM with a weak asthenosphere, a far-field station is significantly more sensitive to sources in the lithospheric stress guide rather than shallower sources in the crust. Increasing the asthenospheric stiffness reduces this sensitivity but also decreases the sensitivity to shallow sources, as observed for the LM of a weak crust over a half-space. This observation is in agreement with *Savage* [1998] for a half-space, and with *Pollitz* [1996] for a spherical layered earth with a sharp increase in E at the crustal-lithospheric boundary. We must recall that although the differences are of the order of tenths of millimeters, this response corresponds to a single source with one meter of slip. Adding more sources will produce a slip difference as observed in Figure 7c.

Discussion and conclusions

We studied the behavior of co-seismic deformation on a layered spherical earth and analyzed the influence of the stiffness of the asthenosphere in the lithospheric stress guide. We found that increasing the stiffness of the asthenosphere tends to increase the strain in the lithosphere reducing its rigid body displacement, while reducing the stiffness produces the opposite effect. This is equivalent to coupling and decoupling the lithosphere from the rest of the model, allowing the lithosphere to displace as a block or deform to satisfy the slip BC. We did not investigate changes in crustal E as these have been previously studied. We confirmed that for all asthenospheric E values, a weak crust is always carried along with the lithosphere.

We also analyzed the strain energy transmitted to the far-field over the stress guide. Increasing the asthenospheric stiffness increases the total strain energy in the system but reduces the transmission of strain energy to the far-field. Strain energy is therefore more concentrated around the fault when a stiff asthenosphere is present. Results from these models seem indicate that further research is needed to determine the level of sensitivity of far-field stations to viscoelastic flow triggered by the observed increase in lithospheric or asthenospheric strain due to a stiff or weak asthenosphere.

We also show the far-field surface displacements as a function of slip depth and asthenospheric stiffness. Due to the low stiffness of the crust, slip concentrated in this weak layer will tend to produce very small far-field displacements (if any), while transmission of strain energy through the stress guide to the far-field will tend to increase far-field sensitivity to downdip slip. This effect is enhanced by strong decoupling of the lithosphere due to a weak asthenosphere. Although the practical application of using far-field observation points during slip inversion is still to be investigated, we suggest that far-field observations can potentially observe the lithospheric and asthenospheric structure below the crust with little influence from the upper crust or details of the rupture. This property might become useful during observation of post-seismic deformation related to afterslip occurring at the downdip edge of the fault.

References

Aagaard, B. T., M. G. Knepley, and C. A. Williams (2013), A domain decomposition approach to implementing fault slip in finite-element models of quasi-static and dynamic crustal deformation, *J. Geophys. Res. Solid Earth*, *118*(6), 3059–3079, doi:10.1002/jgrb.50217.

Burov, E. B., and A. B. Watts (2006), The long-term strength of continental lithosphere: “jelly sandwich” or “crème brûlée”?, *GSA Today*, *16*(1), 4, doi:10.1130/1052-5173(2006)0162.0.CO;2.

Cattin, R., P. Briole, H. Lyon-Caen, P. Bernard, and P. Pinettes (1999), Effects of superficial layers on coseismic displacements for a dip-slip fault and geophysical implications, *Geophys. J. Int.*, *137*(1), 149–158, doi:10.1046/j.1365-246x.1999.00779.x.

Dong, D., T. A. Herring, and R. W. King (1998), Estimating regional deformation from a combination of space and terrestrial geodetic data, *J. Geod.*, *72*(4), 200–214.

Dong, J., W. Sun, X. Zhou, and R. Wang (2014), Effects of Earth’s layered structure, gravity and curvature on coseismic deformation, *Geophys. J. Int.*, *199*(3), 1442–1451, doi:10.1093/gji/ggu342.

Dziewonski, A. M., and D. L. Anderson (1981), Preliminary reference Earth model, *Phys. Earth Planet. Inter.*, *25*(4), 297–356.

Feigl, K. L. et al. (1993), Space geodetic measurement of crustal deformation in central and southern California, 1984–1992, *J. Geophys. Res. Solid Earth*, *98*(B12), 21677–21712.

Fu, G., W. Sun, Y. Fukuda, S. Gao, and T. Hasegawa (2010), Effects of Earth’s curvature and radial heterogeneity in dislocation studies: Case studies of the 2008 Wenchuan earthquake and the 2004 Sumatra earthquake, *Earthq. Sci.*, *23*(4), 301–308.

Jaeger, J. C., N. G. Cook, and R. Zimmerman (2009), *Fundamentals of rock mechanics*, John Wiley & Sons.

Lechmann, S. M., S. M. Schmalholz, G. Hetényi, D. A. May, and B. J. P. Kaus (2014), Quantifying the impact of mechanical layering and underthrusting on the dynamics of the modern India-Asia collisional system with 3-D numerical models: THE MODERN INDIA-ASIA COLLISION, *J. Geophys. Res. Solid Earth*, *119*(1), 616–644, doi:10.1002/2012JB009748.

Le Pichon, X., C. Kreemer, and N. Chamot-Rooke (2005), Asymmetry in elastic properties and the evolution of large continental strike-slip faults, *J. Geophys. Res.*, *110*(B3), doi:10.1029/2004JB003343.

Massonnet, D., M. Rossi, C. Carmona, F. Adragna, G. Peltzer, K. Feigl, and T. Rabaute (1993), The displacement field of the Landers earthquake mapped by radar interferometry, *Nature*, *364*(6433), 138–142.

Okada, Y. (1985), Surface deformation due to shear and tensile faults in a half-space, *Bull. Seismol. Soc. Am.*, *75*(4), 1135–1154.

Pollitz, F. F. (1996), Coseismic deformation from earthquake faulting on a layered spherical Earth, *Geophys. J. Int.*, *125*(1), 1–14.

Savage, J. C. (1998), Displacement field for an edge dislocation in a layered half-space, *J. Geophys. Res. Solid Earth*, *103*(B2), 2439–2446, doi:10.1029/97JB02562.

Savage, J. C., and R. O. Burford (1973), Geodetic determination of relative plate motion in central California, *J. Geophys. Res.*, *78*(5), 832–845.

Thatcher, W. (1995), Microplate versus continuum descriptions of active tectonic deformation, *J. Geophys. Res. Solid Earth*, *100*(B3), 3885–3894.

Turcotte, D. L., and G. Schubert (2014), *Geodynamics*, Cambridge University Press.

Weertman, J., and J. R. Weertman (1964), *Elementary Dislocation Theory*, New York: Macmillan. Pub.

Conclusions

In this dissertation, we have presented several interdisciplinary applications of GPS algorithms and other geodetic methodologies that can be used for earthquake location and to interpolate co- and post-seismic deformation after great earthquakes. Here we discuss the conclusions of each chapter, how they are related, and lines of future research.

In Chapter One, we found that the Bancroft algorithm can improve the solutions of hypocenters located in regions with high GDOP. We propose that this algorithm should be directly applicable to differential earthquake location. The development of an algorithm for layered media based on Bancroft or other non-iterative algorithms could provide more robust differential locations when dealing with earthquake clusters with high GDOP. Another relevant application of Chapter One would be to replace gap with GDOP in reporting earthquake location results. Both gap and GDOP are functions of only the network-event geometry and independent of data and model errors. GDOP is a much more robust indicator of the effect of the network-event geometry on the quality of the location than gap. Gap is a subjective indicator of the effect of the network-event geometry on the potential quality of the solution, having no quantitative mathematical contribution to estimating the location quality. GDOP is a well defined mathematical indicator that can be used to accept or reject a solution during the quality control of events. It’s worth mentioning that GDOP does not depend on how the earthquake was located (homogeneous half-space, layered model, 3D block inversion, etc).

Chapters Two and Three showed how to apply the least squares collocation (LSC) technique - commonly used in geodesy for interpolating gravity - to both co- and post-seismic deformation fields. We rigorously demonstrated that LSC cannot be applied for co-seismic deformation when there aren’t enough observations (GPS sites) available. We suggested that in the near-field the method could be used in combination with InSAR to fill the gaps between GPS observations. Although the precision of InSAR is lower than that of GPS due to “contamination” by post-seismic deformation, this data can be used for lower precision models. In Chapter Three we showed that the post-seismic deformation field is smooth enough that one can apply LSC to interpolate the logarithmic transients produced after a great earthquake.

Results from Chapter Three also uncovered interesting asymmetries in the post-seismic deformation field that were not discussed in the publication. In the Nazca flat slab region under the Precordillera (San Juan, Argentina), the post-seismic signal in the horizontal component of Vel-Ar showed a zero amplitude logarithmic transient. This could be further evidence of a missing asthenospheric wedge under the Precordillera. More data is being collected in this region after the 2015 Mw 8.3 Illapel earthquake. The effects on co-seismic strain in the asthenosphere due to its stiffness are shown in Chapter Five and will be discussed later.

In Chapter Four we continued performing interdisciplinary research by modifying a method used in seismology, beamforming, to apply it to TEC time series obtained from GPS observations. We consider this work to be a potentially significant contribution to the joint efforts of seismology and geodesy to create a new discipline known as “ionospheric seismology.” As part of this work we observed and recovered low SNR ionospheric signals in Antarctica produced by very distant earthquake sources producing acoustic waves induced by the vertical component of propagating Rayleigh waves. We found that due to the orientation of the geomagnetic field and the low elevation of GPS satellites, the South Geomagnetic Pole is a very favorable location to observe nearly-vertical acoustic waves propagating from the surface of the earth into the ionosphere. Future research could examine these signals at the North Geomagnetic Pole, as well as identify other ionospheric signals in the Antarctic region.

Finally, Chapter Five discussed the lithospheric stress guide and the far-field co-seismic deformation. We used models with increasing asthenospheric strength to show how strain and strain energy is transmitted through the stress guide to the far-field, producing co-seismic deformation. We suggested that far-field GPS sites, which are usually not taken into account when analyzing the deformation field after large earthquakes, could provide useful information regarding the lithospheric and asthenospheric structure. For example, we observed in the Vel-Ar model, which appears in Chapter Three, that the near-field post-seismic deformation after the Maule earthquake presents a north-south asymmetry coincident with the location of the flat slab under the Precordillera. Although we did not discuss this in Chapter Three, this distinctive deformation pattern could be due to the effect of a missing asthenospheric wedge under the Precordillera. Thus, the observations from Chapter Three would be consistent with the predictions resulting from Chapter Five: a stiffer lower lithosphere generates less strain in that layer and, therefore, triggers a smaller post-seismic signal. Further studies on the triggering of viscous flow due to the straining of the lithosphere and asthenosphere could help reveal the driving force of post-seismic deformation in the far-field, which is very significant. This is a topic for future work.

Bibliography

Aagaard, B. T., M. G. Knepley, and C. A. Williams (2013), A domain decomposition approach to implementing fault slip in finite-element models of quasi-static and dynamic crustal deformation, *J. Geophys. Res. Solid Earth*, *118*(6), 3059–3079, doi:10.1002/jgrb.50217.

Abel, J. S., and J. W. Chaffee (1991), Existence and uniqueness of GPS solutions, *Aerosp. Electron. Syst. IEEE Trans. On*, *27*(6), 952–956.

Afraimovich, E. L., E. A. Kosogorov, N. P. Perevalova, and A. V. Plotnikov (2001), The use of GPS arrays in detecting shock-acoustic waves generated during rocket launchings, *J. Atmospheric Sol.-Terr. Phys.*, *63*(18), 1941–1957.

Altamimi, Z., X. Collilieux, J. Legrand, B. Garayt, and C. Boucher (2007), ITRF2005: A new release of the International Terrestrial Reference Frame based on time series of station positions and Earth Orientation Parameters, *J. Geophys. Res. Solid Earth, 112*(B9), B09401, doi:10.1029/2007JB004949.

Artru, J., P. Lognonné, and E. Blanc (2001), Normal modes modelling of post-seismic ionospheric oscillations, *Geophys. Res. Lett.*, *28*(4), 697–700.

Artru, J., T. Farges, and P. Lognonné (2004), Acoustic waves generated from seismic surface waves: propagation properties determined from Doppler sounding observations and normal-mode modelling: Propagation of seismic acoustic waves, *Geophys. J. Int.*, *158*(3), 1067–1077, doi:10.1111/j.1365-246X.2004.02377.x.

Artru, J., V. Ducic, H. Kanamori, P. Lognonné, and M. Murakami (2005), Ionospheric detection of gravity waves induced by tsunamis, *Geophys. J. Int.*, *160*(3), 840–848, doi:10.1111/j.1365-246X.2005.02552.x.

Astafyeva, E., K. Heki, V. Kiryushkin, E. Afraimovich, and S. Shalimov (2009), Two-mode long-distance propagation of coseismic ionosphere disturbances, *J. Geophys. Res.*, *114*(A10), doi:10.1029/2008JA013853.

Astafyeva, E. I., and E. L. Afraimovich (2006), Long-distance traveling ionospheric disturbances caused by the great Sumatra-Andaman earthquake on 26 December 2004, *Earth Planets Space*, *58*(8), 1025.

Aster, R. C., B. Borchers, and C. H. Thurber (2013), *Parameter estimation and inverse problems*, Academic Press.

Bancroft, S. (1985), An algebraic solution of the GPS equations, *Aerosp. Electron. Syst. IEEE Trans. On*, (1), 56–59.

Bevis, M., and A. Brown (2014), Trajectory models and reference frames for crustal motion geodesy, *J. Geod.*, *88*(3), 283–311, doi:10.1007/s00190-013-0685-5.

Bilitza, D., D. Altadill, Y. Zhang, C. Mertens, V. Truhlik, P. Richards, L.-A. McKinnell, and B.

Reinisch (2014), The International Reference Ionosphere 2012 – a model of international collaboration, *J. Space Weather Space Clim.*, *4*, A07, doi:10.1051/swsc/2014004.

Burov, E. B., and A. B. Watts (2006), The long-term strength of continental lithosphere: “jelly sandwich” or “crème brûlée”?, *GSA Today*, *16*(1), 4, doi:10.1130/1052-5173(2006)0162.0.CO;2.

Calais, E., and J. B. Minster (1995), GPS detection of ionospheric perturbations following the January 17, 1994, Northridge Earthquake, *Geophys. Res. Lett.*, *22*(9), 1045–1048, doi:10.1029/95GL00168.

Calais, E., and J. B. Minster (1998), GPS, earthquakes, the ionosphere, and the Space Shuttle, *Phys. Earth Planet. Inter.*, *105*(3), 167–181.

Calais, E., J. S. Haase, and J. B. Minster (2003), Detection of ionospheric perturbations using a dense GPS array in Southern California, *Geophys. Res. Lett.*, *30*(12), doi:10.1029/2003GL017708.

Cattin, R., P. Briole, H. Lyon-Caen, P. Bernard, and P. Pinettes (1999), Effects of superficial layers on coseismic displacements for a dip-slip fault and geophysical implications, *Geophys. J. Int.*, *137*(1), 149–158, doi:10.1046/j.1365-246x.1999.00779.x.

Chaffee, J., and J. Abel (1994), On the exact solutions of pseudorange equations, *Aerosp. Electron. Syst. IEEE Trans. On*, *30*(4), 1021–1030.

Darbeheshti, N., and W. E. Featherstone (2009), Non-stationary covariance function modelling in 2D least-squares collocation, *J. Geod.*, *83*(6), 495–508, doi:10.1007/s00190-008-0267-0.

Dautermann, T., E. Calais, and G. S. Mattioli (2009), Global Positioning System detection and energy estimation of the ionospheric wave caused by the 13 July 2003 explosion of the Soufrière Hills Volcano, Montserrat, *J. Geophys. Res.*, *114*(B2), doi:10.1029/2008JB005722.

Dong, D., T. A. Herring, and R. W. King (1998), Estimating regional deformation from a combination of space and terrestrial geodetic data, *J. Geod.*, *72*(4), 200–214.

Dong, J., W. Sun, X. Zhou, and R. Wang (2014), Effects of Earth’s layered structure, gravity and curvature on coseismic deformation, *Geophys. J. Int.*, *199*(3), 1442–1451, doi:10.1093/gji/ggu342.

Drewes, H. (1978), Experiences with least squares collocation as applied to interpolation of geodetic and geophysical quantities, in *Proceedings of Symposium on Mathematical Geophysics, Caracas*.

Drewes, H. (2009), The actual plate kinematic and crustal deformation model APKIM2005 as basis for a non-rotating ITRF, in *Geodetic Reference Frames*, vol. 134, pp. 95–99, Springer Berlin Heidelberg.

Drewes, H., and O. Heidbach (2012), The 2009 Horizontal Velocity Field for South America and the Caribbean, in *Geodesy for Planet Earth*, vol. 136, edited by S. Kenyon, M. C. Pacino, and U. Marti, pp. 657–664, Springer Berlin Heidelberg, Berlin, Heidelberg.

Drewes, H., and L. Sánchez (2013), Modelado de deformaciones sísmicas en el mantenimiento de marcos geodésicos de referencia, Available from: http://www.sirgas.org/fileadmin/docs/Boletines/Bol18/36_Drewes_Sanchez_2013_Modelado_deformaciones_sismicas.pdf (Accessed 4 January 2014)

Drewes, H., and L. Sánchez (2014), Actualización del modelo de velocidades SIRGAS, Available from: http://www.sirgas.org/fileadmin/docs/Boletines/Bol19/60_Drewes_et_al_2014_ActualizacionVEMOS.pdf (Accessed 2 May 2015)

Drob, D. P. et al. (2008), An empirical model of the Earth’s horizontal wind fields: HWM07, *J. Geophys. Res.*, *113*(A12), doi:10.1029/2008JA013668.

Dziewonski, A. M., and D. L. Anderson (1981), Preliminary reference Earth model, *Phys. Earth Planet. Inter.*, *25*(4), 297–356.

Feigl, K. L. et al. (1993), Space geodetic measurement of crustal deformation in central and southern California, 1984–1992, *J. Geophys. Res. Solid Earth*, *98*(B12), 21677–21712.

Fitzgerald, T. J. (1997), Observations of total electron content perturbations on GPS signals caused by a ground level explosion, *J. Atmospheric Sol.-Terr. Phys.*, *59*(7), 829–834.

Fu, G., W. Sun, Y. Fukuda, S. Gao, and T. Hasegawa (2010), Effects of Earth’s curvature and radial heterogeneity in dislocation studies: Case studies of the 2008 Wenchuan earthquake and the 2004 Sumatra earthquake, *Earthq. Sci.*, *23*(4), 301–308.

Galvan, D. A., A. Komjathy, M. P. Hickey, P. Stephens, J. Snively, Y. Tony Song, M. D. Butala, and A. J. Mannucci (2012), Ionospheric signatures of Tohoku-Oki tsunami of March 11, 2011: Model comparisons near the epicenter: TSUNAMI IONOSPHERIC SIGNATURES NEAR EPICENTER, *Radio Sci.*, *47*(4), n/a–n/a, doi:10.1029/2012RS005023.

Garcés, M. A., R. A. Hansen, and K. G. Lindquist (1998), Traveltimes for infrasonic waves propagating in a stratified atmosphere, *Geophys. J. Int.*, *135*(1), 255–263.

Geiger, L. (1912), Probability method for the determination of earthquake epicenters from the arrival time only (translated from Geiger’s 1910 German article), *Bull. St Louis Univ.*, *8*(1), 56–71.

Georges, T. M. (1968), Collisional interaction of atmospheric waves with the ionospheric F region, in *Acoustic-Gravity Waves in the Atmosphere*, vol. 1, p. 377.

Georges, T. M., and W. H. Hooke (1970), Wave-Induced Fluctuations in Ionospheric Electron Content: A Model Indicating some Observational Biases, *J. Geophys. Res. Space Phys.*, *75*(31).

Gómez, D., R. Smalley, D. Piñón, and S. Cimbaro (2014), Colocación por mínimos cuadrados de la deformación co-sísmica del sismo de Maule, Chile 2010: Estimación de observaciones mínimas, San Juan, Argentina.

Gómez, D., R. Smalley, C. Langston, D. Piñón, S. Cimbaro, M. Bevis, E. Kendrick, J. Barón, J. C. Báez Soto, and H. Parra (2015), Co-seismic deformation of the 2010 Maule, Chile earthquake: Validating a least squares collocation interpolation, *GeoActa*, *40*(1), 401.

Hayes, G. P., D. J. Wald, and R. L. Johnson (2012), Slab1. 0: A three-dimensional model of global subduction zone geometries, *J. Geophys. Res. Solid Earth 1978–2012*, *117*(B1), doi:10.1029/2011JB008524.

Heki, K., and J. Ping (2005), Directivity and apparent velocity of the coseismic ionospheric disturbances observed with a dense GPS array, *Earth Planet. Sci. Lett.*, *236*(3-4), 845–855, doi:10.1016/j.epsl.2005.06.010.

Hooke, W.H. (1967), Ionospheric irregularities produced by internal atmospheric gravity waves, *Geophys. Monogr. Ser.*, *18*.

Hunsucker, R. D., and J. K. Hargreaves (2002), *The high-latitude ionosphere and its effects on radio propagation*, Cambridge University Press.

Hu, Y., K. Wang, J. He, J. Klotz, and G. Khazaradze (2004), Three-dimensional viscoelastic finite element model for postseismic deformation of the great 1960 Chile earthquake, *J. Geophys. Res. Solid Earth*, *109*(B12), B12403, doi:10.1029/2004JB003163.

Jaeger, J. C., N. G. Cook, and R. Zimmerman (2009), *Fundamentals of rock mechanics*, John Wiley & Sons.

Kearsley, W. (1977), *Non-Stationary Estimation in Gravity Prediction Problems.*, DTIC Document.

Khazaradze, G., K. Wang, J. Klotz, Y. Hu, and J. He (2002), Prolonged post-seismic deformation of the 1960 great Chile earthquake and implications for mantle rheology, *Geophys. Res. Lett.*, *29*(22), 7–1.

Klein, F. W. (1978), *Hypocenter locations program HYPOINVERSE*, US Department of the Interior, Geological Survey.

Lechmann, S. M., S. M. Schmalholz, G. Hetényi, D. A. May, and B. J. P. Kaus (2014), Quantifying the impact of mechanical layering and underthrusting on the dynamics of the modern India-Asia collisional system with 3-D numerical models: THE MODERN INDIA-ASIA COLLISION, *J. Geophys. Res. Solid Earth*, *119*(1), 616–644, doi:10.1002/2012JB009748.

Lee, W. H. K., and S. W. Stewart (1981), *Principles and applications of microearthquake* *networks*, Academic press.

Leick, A. (2004), *GPS Satellite Surveying*, John Wiley & Sons.

Le Pichon, X., C. Kreemer, and N. Chamot-Rooke (2005), Asymmetry in elastic properties and the evolution of large continental strike-slip faults, *J. Geophys. Res.*, *110*(B3), doi:10.1029/2004JB003343.

Ligas, M., and M. Kulczycki (2010), Simple spatial prediction-least squares prediction, simple kriging, and conditional expectation of normal vector, *Geod. Cartogr.*, *59*(2), 69–81.

Lin, Y. N. et al. (2013), Coseismic and postseismic slip associated with the 2010 Maule Earthquake, Chile: Characterizing the Arauco Peninsula barrier effect: CHARACTERIZING ARAUCO BARRIER EFFECT, *J. Geophys. Res. Solid Earth*, *118*(6), 3142–3159, doi:10.1002/jgrb.50207.

Lognonné, P., E. Clévédé, and H. Kanamori (1998), Computation of seismograms and atmospheric oscillations by normal-mode summation for a spherical earth model with realistic atmosphere, *Geophys. J. Int.*, *135*(2), 388–406.

Lognonné, P., R. Garcia, F. Crespon, G. Occhipinti, A. Kherani, and J. Artru-Lambin (2006), Seismic waves in the ionosphere, *Europhys. News*, *37*(4), 11–15.

Lorito, S., F. Romano, S. Atzori, X. Tong, A. Avallone, J. McCloskey, M. Cocco, E. Boschi, and A. Piatanesi (2011), Limited overlap between the seismic gap and coseismic slip of the great 2010 Chile earthquake, *Nat. Geosci.*, *4*(3), 173–177, doi:10.1038/ngeo1073.

Maerten, F. (2005), Inverting for Slip on Three-Dimensional Fault Surfaces Using Angular Dislocations, *Bull. Seismol. Soc. Am.*, *95*(5), 1654–1665, doi:10.1785/0120030181.

Mannucci, A. J., B. D. Wilson, and C. D. Edwards (1993), A new method for monitoring the Earth’s ionospheric total electron content using the GPS global network, in *Proceedings of the 6th International Technical Meeting of the Satellite Division of the Institute of Navigation (ION GPS 1993)*, pp. 1323–1332.

Massonnet, D., M. Rossi, C. Carmona, F. Adragna, G. Peltzer, K. Feigl, and T. Rabaute (1993), The displacement field of the Landers earthquake mapped by radar interferometry, *Nature*, *364*(6433), 138–142.

Minkowski, H. (1907), Die Grundgleichungen für die elektromagnetischen Vorgänge in bewegten Körpern, *Math. Ann.*, *68*(4), 472–525.

Moreno, M. et al. (2012), Toward understanding tectonic control on the Mw 8.8 2010 Maule Chile earthquake, *Earth Planet. Sci. Lett.*, *321-322*, 152–165, doi:10.1016/j.epsl.2012.01.006.

Moritz, H. (1972), *Advanced least-squares methods*, Department of Geodetic Science, Ohio State University Columbus.

Moritz, H. (1978), Least-squares collocation, *Rev. Geophys.*, *16*(3), 421–430.

Moritz, H. (1980), Advanced physical geodesy, *Adv. Planet. Geol.*, *1*.

Nievergelt, Y. (2000), A tutorial history of least squares with applications to astronomy and geodesy, *J. Comput. Appl. Math.*, *121*(1), 37–72.

Occhipinti, G., P. Dorey, T. Farges, and P. Lognonné (2010), Nostradamus: The radar that wanted to be a seismometer: IONOSPHERIC SEISMOLOGY, *Geophys. Res. Lett.*, *37*(18), n/a–n/a, doi:10.1029/2010GL044009.

Occhipinti, G., L. Rolland, P. Lognonné, and S. Watada (2013), From Sumatra 2004 to Tohoku-Oki 2011: the systematic GPS detection of the ionospheric signature induced by tsunamigenic earthquakes, *J. Geophys. Res. Space Phys.*, *118*(6), 3626–3636.

Okada, Y. (1985), Surface deformation due to shear and tensile faults in a half-space, *Bull. Seismol. Soc. Am.*, *75*(4), 1135–1154.

Picone, J. M., A. E. Hedin, D. P. Drob, and A. C. Aikin (2002), NRLMSISE-00 empirical model of the atmosphere: Statistical comparisons and scientific issues, *J. Geophys. Res. Space Phys.*, *107*(A12), 1468, doi:10.1029/2002JA009430.

Pollitz, F. F. (1996), Coseismic deformation from earthquake faulting on a layered spherical Earth, *Geophys. J. Int.*, *125*(1), 1–14.

Pollitz, F. F. et al. (2011), Coseismic slip distribution of the February 27, 2010 Mw 8.8 Maule, Chile earthquake: CHILE EARTHQUAKE COSEISMIC SLIP, *Geophys. Res. Lett.*, *38*(9), n/a–n/a, doi:10.1029/2011GL047065.

Powell, C. A., M. M. Withers, H. R. DeShon, and M. M. Dunn (2010), Intrusions and anomalous V_p/V_s ratios associated with the New Madrid seismic zone, *J. Geophys. Res.*, *115*(B8), doi:10.1029/2009JB007107.

Pujol, J., and R. Smalley (1990), A preliminary earthquake location method based on a hyperbolic approximation to travel times, *Bull. Seismol. Soc. Am.*, *80*(6A), 1629–1642.

Rolland, L. M., P. Lognonné, and H. Munekane (2011), Detection and modeling of Rayleigh wave induced patterns in the ionosphere, *J. Geophys. Res.*, *116*(A5), doi:10.1029/2010JA016060.

Rost, S., and C. Thomas (2002), Array seismology: Methods and applications, *Rev. Geophys.*, *40*(3), doi:10.1029/2000RG000100.

Savage, J. C. (1998), Displacement field for an edge dislocation in a layered half-space, *J. Geophys. Res. Solid Earth*, *103*(B2), 2439–2446, doi:10.1029/97JB02562.

Savage, J. C., and R. O. Burford (1973), Geodetic determination of relative plate motion in central California, *J. Geophys. Res.*, *78*(5), 832–845.

Seemüller, W., M. Seitz, L. Sánchez, and H. Drewes (2009), The position and velocity solution SIR09P01 of the IGS Regional Network Associate Analysis Centre for SIRGAS (IGS RNAAC SIR), *Munich Ger. Dtsch. Geod. Forschungsinstitut Rep.*, *85*, 96.

Sevilla, M. (1987), Colocación mínimos cuadrados, *PublUniv Complut. Fac Cienc. Mat Inst Astron. Geod.*

Sirola, N. (2004), A versatile algorithm for local positioning in closed form, in *Proceedings of the 8th European conference GNSS, Rotterdam, The Netherlands*, Citeseer.

Sirola, N. (2010), Closed-form algorithms in mobile positioning: Myths and misconceptions, in *Positioning navigation and communication (WPNC), 2010 7th Workshop on*, pp. 38–44, Ieee.

Snay, R. A., J. T. Freymueller, and C. Pearson (2013), Crustal Motion Models Developed for Version 3.2 of the Horizontal Time-Dependent Positioning Utility, *J. Appl. Geod.*, *7*(3), doi:10.1515/jag-2013-0005.

Thatcher, W. (1995), Microplate versus continuum descriptions of active tectonic deformation, *J. Geophys. Res. Solid Earth*, *100*(B3), 3885–3894.

Thurber, C. H. (1985), Nonlinear earthquake location: theory and examples, *Bull. Seismol. Soc. Am.*, *75*(3), 779–790.

Tong, X. et al. (2010), The 2010 Maule, Chile earthquake: Downdip rupture limit revealed by space geodesy: DOWNDIP RUPTURE MAULE, CHILE EARTHQUAKE, *Geophys. Res. Lett.*, *37*(24), n/a–n/a, doi:10.1029/2010GL045805.

Turcotte, D. L., and G. Schubert (2014), *Geodynamics*, Cambridge University Press.

Vieira, S. R., J. R. P. de Carvalho, M. B. Ceddia, and A. P. González (2010), Detrending non stationary data for geostatistical applications, *Bragantia*, *69*, 01–08.

Wang, K., Y. Hu, M. Bevis, E. Kendrick, R. Smalley, R. B. Vargas, and E. Lauría (2007), Crustal motion in the zone of the 1960 Chile earthquake: Detangling earthquake-cycle deformation and forearc-sliver translation, *Geochem. Geophys. Geosystems*, *8*(10), Q10010, doi:10.1029/2007GC001721.

Weertman, J., and J. R. Weertman (1964), *Elementary Dislocation Theory*, Macmillan, New-York/London.

Wessel, P., and W. H. Smith (1998), New, improved version of Generic Mapping Tools released, *Eos Trans. Am. Geophys. Union*, *79*(47), 579–579.

Zweck, C., J. T. Freymueller, and S. C. Cohen (2002), Three-dimensional elastic dislocation modeling of the postseismic response to the 1964 Alaska earthquake, *J. Geophys. Res. Solid Earth 1978–2012*, *107*(B4), ECV–1.